

POLITECNICO DI TORINO

Corso di Laurea Magistrale
in Ingegneria Civile

Tesi di Laurea Magistrale

Surveys of the Cannara Bridge, monitoring with
fiber optic sensors and early signal analysis



Relatore:
Prof. Rosario Ceravolo

Correlatore:
Prof. Filippo Ubertini

Candidato:
Nicola Catalano

A.A. 2018/2019

ABSTRACT

Structural Health Monitoring (SHM) is a helpful tool to check structural conditions and to schedule maintenance operations. Ordinary maintenance with visual inspections alone is not sufficient to avoid closures or collapses of the structures. The aim of the thesis work is to experiment the fiber optic sensors, in particular FBG sensors, to monitor civil structures. In particular, bridges have always played a central role in the economic and social growth of a country. After the events of the last few years the control of infrastructures has risen to ensure safety and serviceability.

In this thesis is presented the case study of Cannara Bridge. It is an arch bridge built after the Second World War. It is located in Perugia, in a seismic area. After inspections to examine the area where the bridge was built and its conditions, it was decided the position of the different fiber bragg gratings (FBGs) sensors. At the beginning geotechnical tests were analyzed and a topographic survey was carried out because it was difficult to find documentation of the bridge. Therefore, a FEM model was created to better understand the behavior of the structure.

The deployment of the Cannara SHM system and sensors technology are described in detail to give the reader a good understanding of the following data analysis.

CONTENTS

1. INTRODUCTION	11
1.1 STRUCTURAL HEALTH MONITORING	12
1.2 SHM AIMS	12
1.3 SHM MONITORING SYSTEMS AND METHODS	14
1.4 DEVELOPMENT OF STRUCTURAL HEALTH MONITORING	17
2. FIBER OPTIC SENSING	23
2.1 HISTORICAL EVOLUTION OF OPTICAL FIBER	25
2.2 OPTICAL FIBER: FEATURE AND ADVANTAGES	25
2.3 FBG SENSORS	29
2.4 DISTRIBUTED FIBER OPTIC SENSING	34
2.4.1 SYSTEMS BASED ON LINEAR DIFFUSION BACKING	39
2.4.2 SYSTEMS BASED ON NON LINEAR RETRO-DIFFUSION	41
2.4.3 NON LINEAR SYSTEMS BASED ON CO-DIRECTIONAL DIFFUSION	45
2.5 CONSIDERATION ABOUT INTEGRATION OF FIBER OPTIC SENSORS IN STRUCTURES	46
2.6 FBG SYSTEMS ACTIVITIES	47
3. CASE STUDY: CANNARA BRIDGE	53
3.1 ARCH BRIDGES	55
3.1.1 MAILLART'S BRIDGES	59
3.2 GEOMETRICAL DESCRIPTION OF CANNARA BRIDGE	61
3.3 HISTORICAL BACKGROUND	62
3.4 NON - DESTRUCTIVE EXPERIMENTAL INVESTIGATIONS	64
3.5 GEOGNOSTICS INVESTIGATIONS	73
3.5.1 DIRECT SHEAR TEST	77
3.5.2 DYNAMIC PENETROMETRIC TEST	78
3.5.3 MASW TEST	81
3.6 TOPOGRAPHIC SURVEY	84

3.7 INTRODUCTION TO FEM MODEL	90
3.7.1 STRAUS7 R 2.4.6	91
3.7.2 FEM MODEL OF THE CANNARA BRIDGE.....	92
3.7.3 MODAL ANALYSIS	96
3.8 MONITORING ACTIVITY.....	102
3.8.1 MONITORING EQUIPMENT	107
3.8.2 FBG ACCELEROMETER FBGA-01	107
3.8.3 TILT METER FBGTi -01.....	110
3.8.4 STRAIN SENSOR FBGS-01.....	111
3.8.5 FBGUARD 1550 FAST	113
3.8.6 PHOTOGRAPHIC REPORT OF THE TEST	115
4.DATA ANALYSIS.....	119
4.1 NATURE OF THE RECORDED SIGNALS.....	119
4.2 FREQUENCY ANALYSIS	126
4.3 TIME-FREQUENCY ANALYSIS.....	129
4.4 CONCLUSION	137

LIST OF FIGURES

FIGURE 1.1 INTEGRATED FRAMEWORK FOR HEALTH MONITORING AND EVALUATION OF CIVIL STRUCTURES (HUA-PENG, 2018).....	13
FIGURE 1.2 STRUCTURAL HEALTH MONITORING STRATEGIES FOR CIVIL ENGINEERING STRUCTURES (AFTER FRANGOPOL AND MESSERVEY 2009).....	16
FIGURE 1.3 I-35W BRIDGE COLLAPSE	18
FIGURE 1.4 COLLAPSE OF VIADOTTO POLCEVERA IN GENOVA	19
FIGURE 2.1 OPTICAL FIBER	26
FIGURE 2.2 OPERATION OF AN OPTICAL FIBER.....	27
FIGURE 2.3 COMPARISON BETWEEN SINGLE MODE AND MULTI-MODE FIBER.....	28
FIGURE 2.4 BRAGG GRATING IN FBG SENSOR.....	30
FIGURE 2.5 OPERATION OF FBG SENSORS	31
FIGURE 2.6 APPLICATION OF TENSION AND COMPRESSION IN A FIBER WITH A FBG SENSOR	32
FIGURE 2.7 TEMPERATURE VARIATION IN A FIBER WITH A FBG SENSOR	33
FIGURE 2.8 SCATTERING OF INCIDENT LIGHT	36
FIGURE 2.9 BACKSCATTERED LIGHTS FROM DIFFERENT LOCATIONS OF FIBER	37
FIGURE 2.10 THREE DIFFERENT SCATTERING MODES	38
FIGURE 2.11 RAYLEIGH DIFFUSION	40
FIGURE 2.12 RAMAN SCATTERING GENERATED BY TEMPERATURE CHANGE ALONG A FIBER	43
FIGURE 2.13 BRILLOUIN SENSOR	44
FIGURE 2.14 DIFFERENT USES OF OPTICAL FIBER.....	48
FIGURE 2.15 SENSORS IN THE TOP LAYER OF THE ROAD SURFACE	49
FIGURE 2.16 QUASI DISTRIBUTED FIBER OPTIC SENSORS IN A DAM	50
FIGURE 2.17 FIBER OPTIC SENSORS FOR SECURITY	51
FIGURE 3.1 PERSPECTIVE OF THE CANNARA BRIDGE	53
FIGURE 3.2 THE YIELDING CALCULATED BY THE PROFESSOR MATERAZZI	54
FIGURE 3.3 SECOND ORDER THEORY P-D	56
FIGURE 3.4 THREE-HINGED ARCH	57
FIGURE 3.5 MARIA PIA BRIDGE, PORTO (PORTUGAL), 1877. (TROYANO, 2006)	58
FIGURE 3.6 LOS TILOS BRIDGE, LA PALMA 2004. (TROYANO 2006).....	58
FIGURE 3.7 ZOUZ BRIDGE, ZERNEZ, MAILLART 1901.....	59
FIGURE 3.8 SALGINATOBEL BRIDGE, SCHIERS, MAILLART 1930	60
FIGURE 3.9 SCHWANDBACH BRIDGE, SCHWARZENBURG, MAILLART 1933	60
FIGURE 3.10 NAPOLI-POMPEI HIGHWAY (IORI 2015).....	61
FIGURE 3.11 PERSPECTIVE VIEW OF THE CANNARA BRIDGE	61
FIGURE 3.12 BRIDGE OF CANNARA IN 1924	63
FIGURE 3.13 LOAD TEST CONFIGURATIONS.....	65
FIGURE 3.14 LOAD TEST CONFIGURATIONS.....	66
FIGURE 3.15 TARGETS POSITIONS ON RIGHT SIDE	67
FIGURE 3.16 BENCHMARKS POSITIONS ON EXTRADOS	67
FIGURE 3.17 DEFORMOMETRIC BASES ON RIGHT SIDE AND ON LEFT SIDE.....	68

FIGURE 3.18 DEFORMOMETRIC BASES ON EXTRADOS	68
FIGURE 3.19 IMAGES OF THE STATIC TEST	69
FIGURE 3.20 LONGITUDINAL DEFORMATION AFTER THE FIFTH CYCLE	73
FIGURE 3.21 TESTS LOCATION IN THE CANNARA BRIDGE AREA.....	74
FIGURE 3.22 CATALOGING BOXE RELATIVE TO SPECIMEN S1.....	74
FIGURE 3.23 GRANULOMETRIC CURVE RELATIVE TO SPECIMEN S1 (10-10.60 METERS DEPTH).....	76
FIGURE 3.24 GRANULOMETRIC CURVE RELATIVE TO SPECIMEN S2 (9.0-9.60 METERS DEPTH).....	77
FIGURE 3.25 DYNAMIC PENETROMETRIC TEST.....	80
FIGURE 3.26 SPEED OF WAVES PROPAGATION WITH SOIL DEPTH	83
FIGURE 3.27 MASW TEST.....	84
FIGURE 3.28 EQUIPMENT OF TOPOGRAPHIC SURVEY	85
FIGURE 3.29 FLIGHT PLAN FOR A HEIGHT OF 50 METERS.....	86
FIGURE 3.30 DRONE PICTURES	87
FIGURE 3.31 POINT CLOUD OF THE CANNARA BRIDGE AREA	88
FIGURE 3.32 SUPERPOSITION OF POINT CLOUD WITH RGB INFORMATION	89
FIGURE 3.33 BEAM ELEMENT	93
FIGURE 3.34 SHELL ELEMENT	93
FIGURE 3.35 FEM MODEL OF THE CANNARA BRIDGE	94
FIGURE 3.36 CHARACTERISTICS OF BEAM ELEMENT IN MODEL WITH REDUCED STIFFNESS	95
FIGURE 3.37 MAIN VERTICAL AND TORSIONAL VIBRATING MODES OF THE MODEL HINGED ON CANNARA SIDE	100
FIGURE 3.38 MAIN VERTICAL AND TORSIONAL VIBRATING MODES OF THE MODEL FULLY RESTRAINED ON CANNARA SIDE	101
FIGURE 3.39 CONDITION OF THE THIRD ARCH OPPOSITE TO THE CENTER OF CANNARA DURING INSPECTIONS.....	102
FIGURE 3.40 POSITION OF THE SENSORS ON THE LEFT SIDE OF THE BRIDGE	103
FIGURE 3.41 POSITION OF THE SENSORS ON THE RIGHT SIDE OF THE BRIDGE	104
FIGURE 3.42 POSITION OF THE L-B1 ON LEFT AND L-B2 ON RIGHT UNDER THE ARCH.....	104
FIGURE 3.43 INTERROGATION UNIT.....	105
FIGURE 3.44 FBGA-01 ACCELEROMETER	108
FIGURE 3.45 TILT METER FBGTi-01.....	110
FIGURE 3.46 STRAIN SENSOR FBGS-01	112
FIGURE 3.47 FBGUARD 1550 FAST	113
FIGURE 3.48 L-B4 ON THE LEFT AND L-B3 ON THE RIGHT	115
FIGURE 3.49 ACCELEROMETER 1 AND ACCELEROMETER 3 ON THE LEFT SIDE OF THE BRIDGE	115
FIGURE 3.50 ACCELEROMETER 6 AND TILT METER 2 ON THE LEFT AND ACCELEROMETER 4 AND TILT 7 ON THE RIGHT	116
FIGURE 3.51 L-B1 ON THE LEFT AND INSTALLATION OF L-B2 ON THE RIGHT	116
FIGURE 3.52 CANNARA BRIDGE DURING INSTALLATION	116
FIGURE 3.53 CANNARA BRIDGE DURING INSTALLATION	117
FIGURE 3.54 INSTALLATION OF ACC1 WITH BASKET ON THE LEFT AND THE LADDER USED TO INSTALL SENSORS ON THE RIGHT.....	117

FIGURE 3.55 THE TRUCK OF 30 TONS DURING THE TEST AND THE ANALYSIS	117
FIGURE 4.1 INTERFACE FBGUARD	120
FIGURE 4.2 INTENSITY OF SIGNAL IN CHANNEL 4.....	121
FIGURE 4.3 SIGNAL IN TIME DOMAIN OF ACCELEROMETER 3 DURING STANDARD TRAFFIC	122
FIGURE 4.4 SIGNAL IN TIME DOMAIN OF ACCELEROMETER 1 DURING STANDARD TRAFFIC	122
FIGURE 4.5 SIGNAL OF TILT 7 DURING STANDARD TRAFFIC.....	123
FIGURE 4.6 SIGNAL IN TIME DOMAIN OF THE 6 ACCELEROMETERS DURING TRUCK TEST	123
FIGURE 4.7 SIGNAL IN TIME DOMAIN OF THE 4 STRAIN GAUGES DURING TRUCK TEST	124
FIGURE 4.8 SIGNAL OF THE 2 TILT METERS DURING TRUCK TEST.....	124
FIGURE 4.9 SIGNAL OF L-B1 DURING TRUCK TEST ON LEFT AND DURING STANDARD TRAFFIC ON RIGHT	125
FIGURE 4.10 SIGNAL OF L-B2 DURING TRUCK TEST ON LEFT AND DURING STANDARD TRAFFIC ON RIGHT	125
FIGURE 4.11 SIGNAL OF L-B3 DURING TRUCK TEST ON LEFT AND DURING STANDARD TRAFFIC ON RIGHT	125
FIGURE 4.12 SIGNAL OF L-B4 DURING TRUCK TEST ON LEFT AND DURING STANDARD TRAFFIC ON RIGHT	126
FIGURE 4.13 TRANSITION FROM TIME DOMAIN TO FREQUENCY DOMAIN	127
FIGURE 4.14 SPECTOGRAM OF ACCELEROMETER 3 LOCATED ON THE SIDE OPPOSITE TO THE CANNARA CENTER DURING STANDARD TRAFFIC	131
FIGURE 4.15 ACCELEROMETER 3 OPPOSITE TO THE CANNARA CENTER DURING STANDARD TRAFFIC	131
FIGURE 4.16 SPECTOGRAM OF ACCELEROMETER 5 LOCATED ON THE SIDE OF CANNARA CENTER DURING STANDARD TRAFFIC	132
FIGURE 4.17 ACCELEROMETER 5 ON THE SIDE OF CANNARA CENTER DURING STANDARD TRAFFIC .	132
FIGURE 4.18 SPECTOGRAM OF ACCELEROMETER 2 LOCATED IN THE MIDDLE OF THE BRIDGE DURING STANDARD TRAFFIC	132
FIGURE 4.19 ACCELEROMETER 2 LOCATED IN THE MIDDLE OF THE BRIDGE DURING STANDARD TRAFFIC	133
FIGURE 4.20 SPECTOGRAM OF ACCELEROMETER 1 LOCATED IN THE MIDDLE OF THE BRIDGE DURING TRUCK TEST.....	133
FIGURE 4.21 ACCELEROMETER 1 LOCATED IN THE MIDDLE OF THE BRIDGE DURING TRUCK TEST.....	134
FIGURE 4.22 SPECTOGRAM OF ACCELEROMETER 4 LOCATED ON THE SIDE OPPOSITE TO THE CANNARA CENTER DURING TRUCK TEST	134
FIGURE 4.23 ACCELEROMETER 4 LOCATED ON THE SIDE OPPOSITE TO THE CANNARA CENTER DURING TRUCK TEST.....	134
FIGURE 4.24 ACCELEROMETER 1 LOCATED IN THE MIDDLE OF THE BRIDGE DURING TRUCK TEST (FREE DECAY)	135
FIGURE 4.25 SPECTOGRAM OF ACCELEROMETER 1 LOCATED IN THE MIDDLE OF THE BRIDGE DURING TRUCK TEST (FREE DECAY).....	136

LIST OF TABLES

TABLE 2.1 CLASSIFICATION OF FIBER OPTIC SENSORS	24
TABLE 3.1 DEFINITION OF CYCLE LOAD.....	64
TABLE 3.2 CHARACTERISTICS OF TRUCKS	65
TABLE 3.3 VERTICAL DISPLACEMENTS ON INTRADOS	70
TABLE 3.4 VERTICAL DISPLACEMENTS ON EXTRADOS	71
TABLE 3.5 DEFORMOMETRIC VARIATIONS	72
TABLE 3.6 STRATIGRAPHIC ANALYSIS OF S1 AND S2 SPECIMEN	75
TABLE 3.7 COHESION AND FRICTION ANGLE RELATIVE TO S1 AND S2 SPECIMEN	78
TABLE 3.8 CHARACTERISTICS OF PAGANI 73-100 SCPT PROBE	79
TABLE 3.9 ISSMFE TECHNICAL STANDARDS	79
TABLE 3.10 SEISMIC CLASSIFICATION OF ITALY BASED ON PGA	81
TABLE 3.11 MASW TEST RESULTS	83
TABLE 3.12 FLIGHT PLANS.....	87
TABLE 3.13 TOTAL MASS PARTICIPATION FACTORS FOR ALL TWENTY MODES FOR EACH DEGREE OF FREEDOM	97
TABLE 3.14 CHARACTERISTICS OF FEM MODEL HINGED ON CANNARA SIDE	98
TABLE 3.15 CHARACTERISTICS OF FEM MODEL FULLY RESTRAINED ON CANNARA SIDE.....	98
TABLE 3.16 CHARACTERISTICS OF FEM MODEL HINGED ON CANNARA SIDE WITH REDUCED STIFFNESS	98
TABLE 3.17 CHARACTERISTICS OF FEM MODEL FULLY RESTRAINED ON CANNARA SIDE WITH REDUCED STIFFNESS.....	99
TABLE 3.18 CHANNELS OF FBGUARD	105
TABLE 3.19 CHARACTERISTICS OF STRAIN GAUGES	106
TABLE 3.20 DETAILS OF THE TEST WITH THE TRUCK OF 30 TONS.....	106
TABLE 3.21 DETAILS OF THE TEST WITH THE TRUCK OF 30 TONS.....	107
TABLE 3.22 DATA SHEET FBGA-01 ACCELEROMETER	109
TABLE 3.23 WAVELENGTH OF ACCELEROMETERS.....	109
TABLE 3.24 DATA SHEET TILT METER FBGTI-01	111
TABLE 3.25 DATA SHEET STRAIN SENSOR FBGS-01	113
TABLE 3.26 DATA SHEET FBGUARD 1550 FAST	114
TABLE 4.1 MAXIMUM VALUES OF CRACKS OPENING DURING STANDARD TRAFFIC AND TRUCK TEST	1266
TABLE 4.2 ENERGY PEAKS IN THE MARGINAL GRAPHS DURING TRUCK TEST.....	1355
TABLE 4.3 ENERGY PEAKS IN THE MARGINAL GRAPHS DURING TRUCK TEST (FREE DECAY).....	1355

1. INTRODUCTION

Infrastructures will inevitably suffer from damage accumulation and resistance degradation subjected to actions of environmental corrosion, material aging, fatigue and hazards during their life time service. Therefore, in order to assure structural safety, integrity and durability it is important to introduce intelligent health monitoring systems to monitor civil structures during the construction process and also during service life. In particular bridges are the most important facilities for many cities and countries. These infrastructures provide the necessary communication and transport conditions for the residence. If we don't assure maintenance operations and warning, the closure or the collapse of these bridges is possible. The implementation of SHM in civil infrastructure is made also possible by the use of optical fiber sensors and it can substantially improve safety of civil structures and help to manage them more efficiently.

In my thesis work I want to experiment the fiber optic sensors (FBGs sensors) to monitor a civil structure. There are several advantages to use fiber optic sensors. One of all is the possibility to monitor bridges and infrastructures located in areas where power electricity is not available because the fiber optic sensors (FOSs) are completely passive. We can place the interrogation unit up to 50 km away from the monitored structure. Furthermore, the optical fiber used in the telecommunications field, if it is properly doped, it can become a distributed sensor along its entire length. It can be used to monitor pipeline leakage.

In my thesis work it was decided to experiment fiber bragg gratings (FBG) sensors on the Cannara Bridge. I with the support of Giovacchino Rosati, manager of Eagle Projects company, decided to cooperate with NBG Systems company. The goal is the monitoring of the bridge using fiber optic sensors directly produced by NBG Company. The bridge is located in Perugia, in the center of Italy. There was no documentation about it. I started to do a topographic survey. It was necessary to continue in my analysis. Afterwards a FEM model was realized. The analysis of the data recorded by the sensors during the acquisitions was developed using an analysis in time-frequency

domain. The frequencies of the fem model are compared to those obtained by fbg accelerometers.

1.1 STRUCTURAL HEALTH MONITORING

“Structural Health Monitoring (SHM) is a process aimed at providing accurate and in-time information concerning structural condition and performance on a proactive basis. It consists of permanent continuous, periodic or periodically continuous recording of representative parameters, over short or long terms. The information obtained from monitoring is generally used to plan and design maintenance, increase the safety, verify hypotheses, reduce uncertainty and to widen the knowledge concerning the structure being monitored” (More, et al., 2018).

This process consists of many activities including sensing network, data processing and analysis, damage assessment and decision making. It can offer significant economic and life-safety benefits. However, the application of the SHM technology to actual civil engineering structures is still in infancy, and it requires advancements in various fields due to its multi-disciplinary nature. (Hua-Peng, et al., 2018).

Many professors have compared the process of structural health monitoring to the illness experienced by human body. When a person is sick, the unhealthy condition is detected by the nervous system and it sends signals to the brain. Person realizes to be ill and he contacts the doctor to avoid worsening conditions. Synonymously the sensors applied on the structure work like the nervous system and the acquisition system act as the brain. The structural expert is compared to the doctor, he analyzes data given by sensors and he proposes a solution strategy.

1.2 SHM AIMS

SHM aims to give, at every moment during the life of the structure, a diagnosis of the state of the different materials, of the constituent parts, and of the full assembly of these parts constituting the structure as a whole.

Civil infrastructure (bridges, buildings, towers, tunnels, dams) deteriorate over time. This deterioration can be caused by various reasons:

- Aging of the constructions materials;
- Failure due to cyclic traffic loads;
- Normal load conditions during lifetime;
- Effects of environmental factors (e.g. steel corrosion, concrete carbonation);
- Damage due to exceptional events, such as earthquakes, hurricanes and floods.

All these factors are variables with uncertainties. So it becomes very difficult to define the structural health in terms of its age and usage and its level of safety. In order to reliably asses structural health and maintain structural safety, monitoring of the structure is essential (Hua-Peng, et al., 2018).

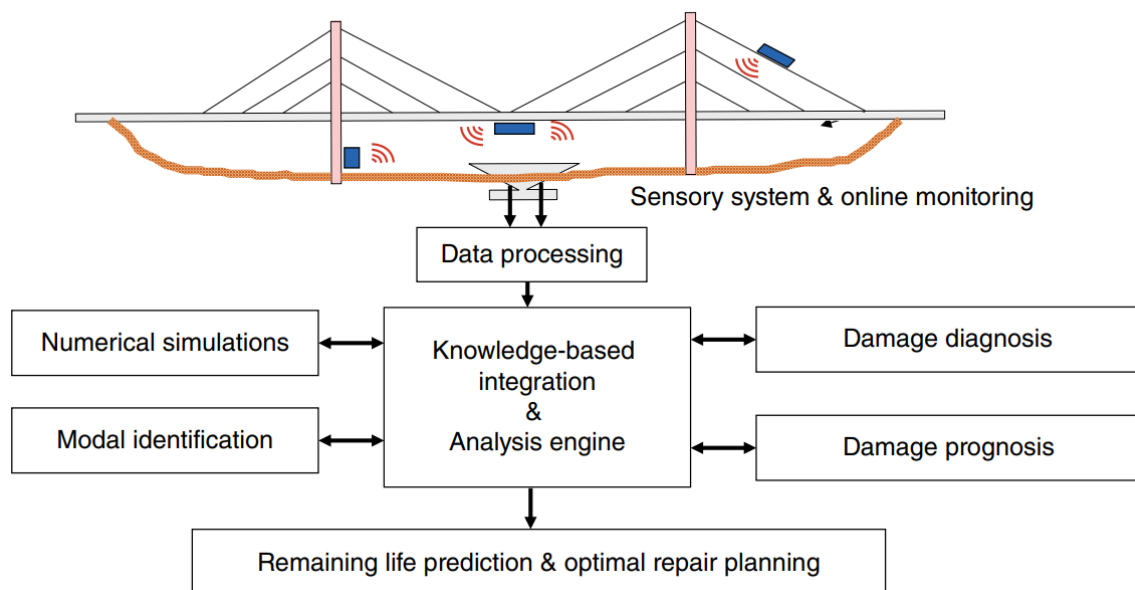


Figure 1.1 Integrated framework for health monitoring and evaluation of civil structures (Hua-Peng, 2018)

For many years the assessment of existing civil infrastructure is largely analyzed by visual inspection. For example, condition of bridges is usually expressed in terms of subjective indices based on visual inspection alone. This is an inaccurate activity to

determine anomalies, to detect deterioration and to assess damage for decision making even when this is conducted by experts (Aktan, et al., 1998).

SHM uses sensing systems and associated hardware and software facilities to monitor the structural performance and operational environments of engineering structures. This process allows to identify the structural behavior such as the damage of the material or of the structural elements, changes in the behavior of constraints and connection systems or reductions in the performance of the structure. Thus, it is possible to optimise maintenance strategies to avoid further deterioration of the structure and to increase the safety level of existing structure and also to monitor those under construction.

1.3 SHM MONITORING SYSTEMS AND METHODS

The SHM method depends on two different factors:

- Sensing technology;
- Signal analysis and interpretation algorithms.

The sensing component of SHM system includes the selection of sensor types to be used, the number of these to be used and their location. Sensors can capture a wide variety of parameters associated with load and environmental conditions. There are countless number of sensors that we can consider to monitor a structure. The sensors can be embedded in the concrete during the construction of the structure or they can put on the structure when the construction is finished.

Standard strain gages and accelerometers have been in wide use for decades to measure structural responses. In the last decade, optical fiber sensors have been applied for strain, temperature, pressure and vibration measurement and GPS sensors to measure bridge deflection which is a critical measure due to the need of a fixed reference point (Duzgun Agdas et al., 2015).

A single SHM system can comprise more than one different kinds of sensors, and whatever the strategies chosen, the data must be merged, processed and evaluated using different algorithms to ensure the safety of the structure (Chapuis, et al., 2017).

The responses that we commonly measure with sensors can be divided in three different categories:

- Mechanical: strain, deformation, displacement, cracks opening, stress, load;
- Physical: temperature, humidity, pore pressure;
- Chemical: chloride penetration, sulphate penetration, Ph, carbonatation penetration, rebar oxidation, steel oxidation.

Another important aspect is how often the data should be collected. The data acquisition component involves selecting the excitation methods, signal conditioning and data acquisition hardware. The transmission of data can take place by wired or wireless transmission networks. The data processing includes different activities: data validation, normalization, cleansing, fusion and compression (Hua-Peng, et al., 2018).

Because data can be measured under different conditions, the normalization becomes necessary in SHM process. One of the most common procedures is to normalize the measured responses by the measured inputs. When is too hard to determine environmental or operating condition the data can be normalized in some temporal fashion to facilitate the comparison of data measured at similar times of an environmental or operational cycle (Sohn, et al., 2003).

The purpose of data fusion is to integrate data from different sensors to make a more confident structure response than is possible with any one sensor alone.

Data cleansing is an activity of selectively choosing data to accept for, or reject from, the feature selection process. There are two different data cleansing procedures applied to data acquired during dynamic tests: filtering and decimation. Sohn believes that these techniques are used extensively in the reviewed literature

although they are not generally identified by the term data cleansing (Sohn, et al., 2003).

The area of SHM which is the most important is feature extraction because the amount of data gathered from sensors will be massive and will require condensation. Feature extraction is considered a process of the identifying damage – sensitive properties, derived from measured system response, which allows one to distinguish between the undamaged and damaged structure. Linear modal properties are the most common features used to identify the damages (resonant frequencies, mode shapes, or properties derived from mode shapes such a flexibility coefficients).

The selection of SHM system and method depends on what we want to analyze. SHM strategies can be divided in two different: local and global monitoring strategies. The two categories provide different types of information and support different types of analysis (Hua-Peng, et al., 2018).

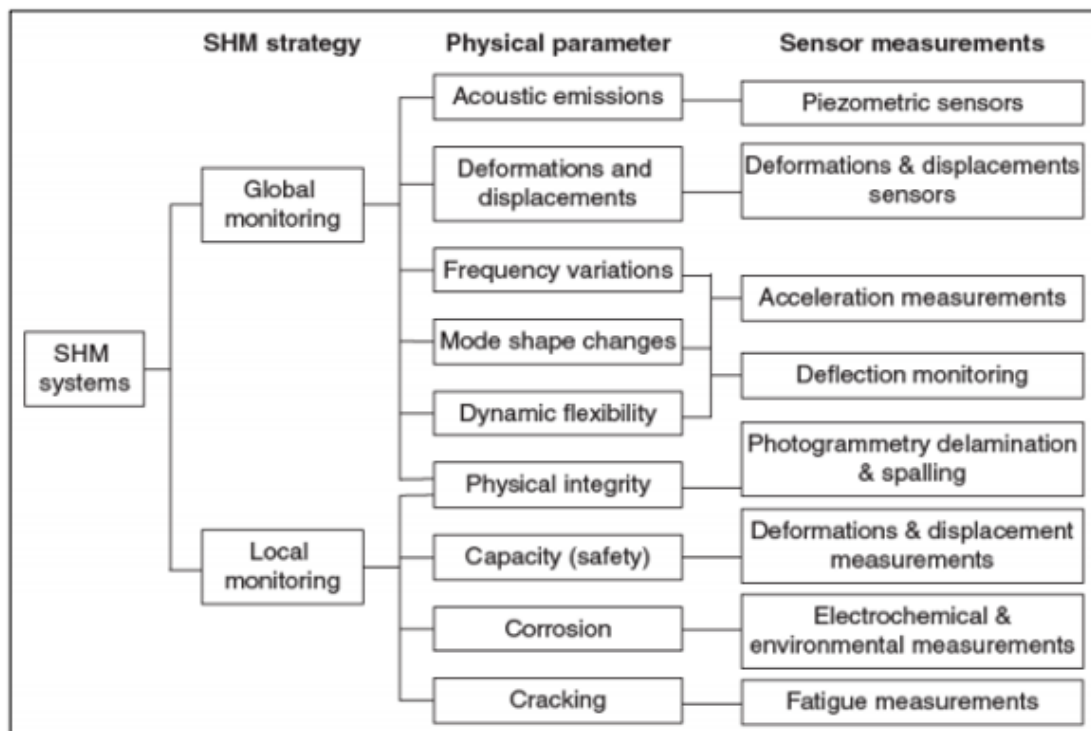


Figure 1.2 Structural health monitoring strategies for civil engineering structures (after Frangopol and Messervey 2009)

A global monitoring approach has to be chosen when we don't have access to a specific part of the structure. For this monitoring we can use accelerometers for measuring the dynamic response of the structure subjected to forced or ambient vibration. We can use acceleration data to extract modal parameters such as mode shape or natural frequencies. This strategy only determine whether or not damage is present somewhere in the whole structure. Once the damage is present, further examination of the structure are carried out to locate the exact position and severity of the damage. So local SHM methods, such as guided waves to measure the state of stress or to identify cracks position are adopted. Therefore, we can say that both global and local SHM methods are necessary to monitor civil structures during their all life (Hua-Peng, et al., 2018).

1.4 DEVELOPMENT OF STRUCTURAL HEALTH MONITORING

Nowadays Structural Health monitoring is becoming an area of great technical and scientific interest. The increasing age of our existing infrastructure makes the cost of maintenance and repairs a growing concern. SHM may alleviate this by replacing scheduled maintenance with as-needed maintenance, thus saving the cost of unnecessary maintenance, on one hand, and preventing unscheduled maintenance, on the other hand.

The introduction of SHM sensors and systems in new structures from the design stage is likely to greatly reduce the life-cycle cost (Gharibnezhad, et al., 2011).

This field is growing very fast, there are countless sensors, methods and data reduction techniques to achieve the same goal of determining how the structure feels, structural integrity, damage presence (or not) and remaining life.

In the last decade many technological advancements have arrived: advances in sensor technology such as smart sensors and wireless sensors and advancement of finite element modelling techniques (Doebbling, et al., 1998).

The use of wireless sensor networks have the potential to increase SHM deployments. In fact, these sensors reduce dramatically the cost of implementation

of SHM compared with other sensor networks. The reduction in cost of sensors enables to increase their density. Thus an increased sensor density can lead to improvements in monitoring reliability (Lynch, et al., 2006).

Wireless sensor networks (WSNs) have attracted a lot of attention also for their high flexibility and high efficiency. Many SHM systems on bridges have been equipped with FOS sensors (Fiber Optic Sensors), providing reliable measurements of strain and temperature including Tsing Ma Bridge, the Yonghe Bridge, the Ebian Bridge and Siggenthal Bridge (X. Meng, 2018).

One of all reason that led to an increasing research in SHM field is the growing pressures of managing ageing infrastructures after dramatic events. An example is the collapse of the I-35W Bridge across Mississippi river in Minneapolis, in 2007.



Figure 1.3 I-35W Bridge collapse

The catastrophic failure occurred during the evening causing the death of 13 people and a total amount of 145 injured. Since 1993, the bridge was inspected every year by Mn/DOT, although no inspection report was completed in 2007, due to the construction work. In the years before the collapse several reports cited problems with the bridge structure (Anderson, et al., 2007). The presence of sensors real-time

monitoring the structure would have been lifesaving. This event highlighted public safety issues related to the ageing infrastructures management.

Another catastrophic collapse was that of Viadotto Polcevera (Genova, Italy) in August 2018 that caused the death of 43 people. This bridge was particularly affected by corrosion and premature aging during its life. Lots of maintenance and strengthening interventions were executed on it. The prevention or early warning of such an event is one reason for the implementation of SHM.



Figure 1.4 Collapse of Viadotto Polcevera in Genova

“It is expected that the further development of SHM systems in civil structures will lead to the establishment of a comprehensive methodology for automated health monitoring of civil structures, so that true condition based inspection and maintenance would become a reality” (Karbhari, 2009).

SHM is a process applied also to aerospace and automotive structures. They are built with higher level of precision than civil structures. In this last case accuracy of implementation and uncertainty of workmanship are often an issue. Total

uniformity of material is never achieved when concrete materials are used. Furthermore, civil structures are also affected by environmental conditions such as temperature and moisture. For example, the natural frequencies of a bridge are often related to the temperature variation around the bridge due to thermal effects. For all these problems the health monitoring and evaluation of civil infrastructure become a challenge (Hua-Peng, et al., 2018).

Balageas in his article written in 2006 said that a bridge inspection during the late 1980s revealed that on the 576.000 US highway bridges, 236.000 were rated deficient by present day standards.

The most obvious benefit to continue research on SHM strategies is increased human safety. Other additional benefits will come from the policy change that sophisticated SHM systems could generate. Most of civil structures undergo routine inspection and maintenance at specific time intervals. For example, in the USA are scheduled every two years. Thus, any unexpected faults occurring in between scheduled inspections may be ignored and cause danger to life. The set timescales for inspections of civil structures is conservative so if a structure continues to be in good health, the costs of inspections could have been saved. Sometimes structural components may be replaced even if they are in good conditions, the economic impact may be even greater. Therefore, the development of SHM strategies would be an economic and environmental benefit (Hua-Peng, et al., 2018).

Significant future growth of an SHM strategy requires multi-disciplinary research involving different fields such as sensor, signal processing, data telemetry, data interpretation, numerical modelling, probabilistic analysis and computational hardware. It is a very complex and diverse topic and it is difficult to see it being solved in the immediate future. Nevertheless, advancements in SHM will be made requiring focused and integrated research efforts.

Bridges are the civil infrastructure which should be controlled most in the future. They provide connections between regions and facilitate regional cooperation as well as economic and social development of countries. A collapse or a closure of a

bridges can lead financial losses and in some cases heavy casualties (Meng, et al., 2018). In many countries such as China and Japan there are studies to implement Structural Health Monitoring on bridges for evaluating their current health status. The Tsing Ma Bridge, which is 1337 m long located in Hong Kong, has equipped with the most complete and sophisticated SHM system. It is called Wind and Structural Health Monitoring System (WASHMS) and it consists of more than 800 different types of sensors installed on the bridge, including Global Position System (GPS) sensors, accelerometers, and strain gauges (Meng, et al., 2018).

2. FIBER OPTIC SENSING

In the first chapter of this thesis work we have seen that lots of structure like bridges, dams, buildings and roadways require evaluation of their performance and health in order to plan maintenance activities and to prevent premature and unexpected failures. These goals can be achieved using effective sensors. The measurements required for structural monitoring are manifold: displacement, velocity, acceleration, jerk, force, stress, strain, temperature, fracture, fatigue and others. Measuring all of these different parameters is possible only using a complementary set of sensors and sensing technologies. Furthermore there are number of issues related to the geometric and time scales over which the measurements must be made. Civil structure are very large however the interest point, such as fracture, yielding or scour occur at localized and precise positions that cannot be identified before. Thus, it is better to introduce sensors able to capture data both locally and globally simultaneously (Huston, et al., 1999).

In general we can classify the sensors based on:

- measured parameter: temperature, pressure, vibration, deformation, corrosion, etc.
- physical principle used: optical, mechanical and electrical sensors
- sector of use: chemical, robotic, agricultural, civil and mechanical sensors etc.

There are two different kind of sensors: active or passive. Active sensors don't need power from outside to supply the output signal deriving from the application of the process variable, they present in output a low value of energy that must be amplified. However passive sensors require an external power supply. An important parameter to define is the sensitivity: it is defined as the transduction efficiency of the sensor and its value is defined as the ratio between the variation of the value measured by the instrument and the variation of the quantity to be measured due to infinitesimal variations.

Up to now, a lot of sensors and instruments are developed for the safety control of civil structures and fiber optic sensors is gradually recognized as the most perspective sensor for safety control of civil structures. At the beginning optical fiber was used in telecommunications field and only in the last decade it is introduced massively for structural monitoring. The principle is completely different: the optical fibers used in telecommunications are not sensitive to displacements, vibration, pressure and temperature variations while in monitoring the optical fibers must precisely detect these data.

Today fiber optic sensors can be considered more flexible and sensitive than traditional sensors. Their main advantages is to be insensitive to electromagnetic noise.

In particularly Fiber Bragg Grating sensors (FBG) are widely used for monitoring the stress states and crack of lots of civil structures. Due to their fundamental features, firstly their small size, which enables minimal interferences with the physical characteristic being measured and the element under investigation, and the very high sensitivity, up to 0.1me (microstrain) for the mechanical deformation and up to 0.1°C for temperature changes, these sensors are also particularly suitable for long term and real time observation from modern civil buildings to historical and cultural heritage structures (Vendittozzi, et al., 2011).

In the structural field we can classify fiber optic sensors based on measured parameters:

Measurement systems	Measured parameters
Bragg Gratings (FBG)	Deformation, displacement, temperature, pression
Fabry Pérot	Deformation, temperature, pression
Microbending	Temperature, pression, deformation
Sofo	Displacement, deformation, inclination
Raman	Distributed temperature
Brillouin	Distributed temperature and deformation

Table 2.1 Classification of fiber optic sensors

In the next paragraphs we will explain in detail the operation of some of these most used sensors.

2.1 HISTORICAL EVOLUTION OF OPTICAL FIBER

The history of optical fibers starts around the 1950s. In 1956 the first optical fiber was physically produced, but it was applied in the telecommunications field only in 1969 thanks to the cooperation between Nippon Sheet Glass Co. and Nippon Electric Co. At the beginning the damping of the fiber was 100 dB/km and it was mainly caused by chemical impurities in the glass. Charles K. Kao of STC and George A. Hockham of British Post Office showed that fiber optics could be a practical means of communication only if the attenuation had been reduced below 20 dB/km.

Thus, in 1970 the first optical fiber for communication was realized by four researchers: Robert D. Maurer, Donald Keck, Peter Schultz and Frank Zimar employed at Conory a glass manufacturer company: they built a fiber with 17 dB of optical attenuation per kilometer, by doping the silicon of the glass with titanium. In the following years lots of progress appeared. In 1976 in many countries like Usa, Japan and Great Britain there was an optical fiber with a damping < 1 dB/km. In this fiber was used not visible light but infrared. Today we use optical fiber with a damping < 0.2 dB/km.

2.2 OPTICAL FIBER: FEATURE AND ADVANATEGES

Fiber optic technology started to develop at the end of 1800 (with different applications compared to present days) but optical properties and its operational principles have much older origin. The introduction of optic fiber has revolutionized the telecommunication field. Since 1970 fiber cables have replaced copper ones to speed up data transmission. Only in the last twenty years the optic fiber has been introduced in civil engineering field to monitor structures. In particular in 1978 Ken O. Hill discovered the effect of optical sensitivity for the fiber doped with Germanium. Exposure to ultraviolet light produces a permanent change of the refractive index. The next step was to use this effect and to write the grating in the fibers so they could

reflect a peak of light very tight. The first Fiber Bragg Grating Sensors were available in 1995 distributed by 3M and Photonetics.

Optic fibers are filaments of glassy or polymeric material, made in such a way to be able to conduct light. They are normally used in form of cables. Each fiber consists of three concentric layers: the core which is the innermost, a cladding and an outer coating. The core and the cladding can be realized in silica or plastic polymers.

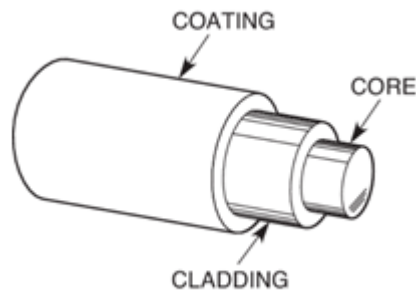


Figure 2.1 Optical fiber

The fiber glass is made starting from ultrapura silica which is provided from the reaction between silicon tetrachloride and oxygen. In the material of the core is added germanium (in the form of germanium tetrachloride) to increase the refractive index without changing the attenuation. While in the silica used to realize cladding, boron is added in order to reduce the refractive index. The main disadvantage of optical fiber made in silica is fragility. On the other hand the polymeric fiber are made by polycarbonates, polycythacurates and polysiloxanes. They have a diameter of the core bigger than silica fiber so it is possible to realize multimode fiber. Polymeric optical fibers are much easier to handle than silica ones; they have a higher mechanical strength and attenuation. For their characteristics this type of fiber is used for small distances, in aerospace or automotive field and also in lighting and medical applications.

A phenomenon of total internal reflection takes place in optical fibers: the discontinuity of the refractive index between the materials of the core and the coating

traps the light radiation as long as it maintains a little grazing angle. Therefore when the fiber makes very sharp curves the total reflection is not possible.

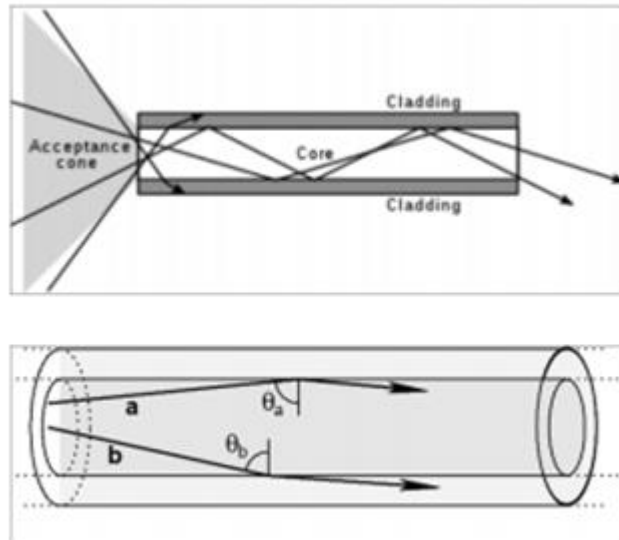


Figure 2.2 Operation of an optical fiber

In the figure above there are two electromagnetic rays which affect the interface between the core and the coating inside the fiber. The a ray incides with an angle bigger than the critical angle of total reflection and it remains trapped in the core, while the other (b ray) incides with an angle lower than the critical and it is refracted in the mantle and therefore it is lost. It is important to remember that in optical we consider the angle between the radiation and the normal to the surface: $q = 90^\circ - a$ where a is the angle between the radiation and the surface.

The core has different dimensions depending if we have a single-mode fiber (SMF) which consists of a smaller core and allows only one mode or multi-mode fiber (MMF) which has a larger core and allows multiple modes of light to travel through the fiber simultaneously. In particular the diameter of the core in single-mode fiber is between 8 and 10 mm while it become bigger in multi-mode fiber. Its dimension is between 50 and 62.5 mm. The cladding has a diameter of 125 mm. The outermost layer is used to give better structural strenght and protection to the fiber. The cladding

and the core have different indices of refraction. Typically the index of the cladding is slightly lower than that of the core.

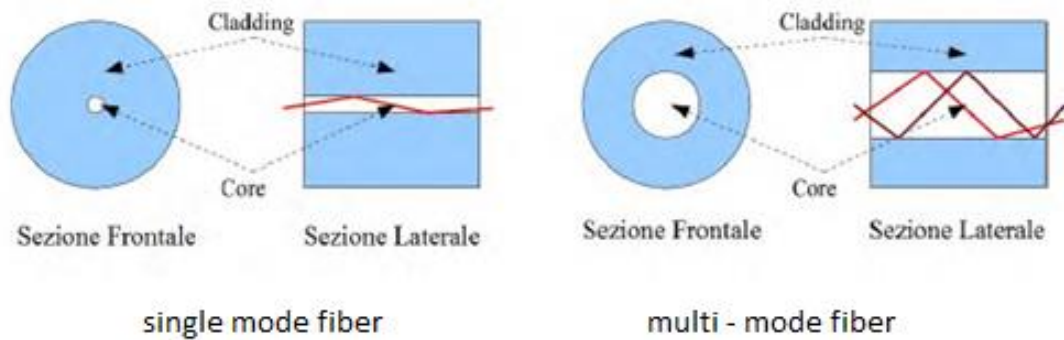


Figure 2.3 Comparison between single mode and multi-mode fiber

The use of optic fiber has several advantages. First of all the *dimension*: the fiber is very small and so we don't have intrusiveness problems in the structure. A FBG sensor measure 150 micron. It can be used to monitor small crack or it can be introduced in composite materials to obtain "smart structure".

The fiber is *immune to electromagnetic interference* and a FBG sensor is a *passive* element that does not need power supply for its operations. It has *high resolution and accuracy*: a FBG sensor has the ability to detect a very small variation of the quantity to be measured (resolution) (1×10^{-7}) and it has also a high accuracy in determining the maximum deviation between the measured value and the real one.

The fiber optic sensors have *high stability*. They are *insensitive to aging* during all their life compared to traditional sensors and to corrosion. They are *resistant* to adverse weather conditions. Once installed they can be used for years without recalibration. It is possible to install the sensors on the structures and interrogate them years later simply bringing the interrogation unit to the site.

A further property of the fiber is *multiplexing*: on a single stretch of optic fiber it is possible to allocate more than one sensor to measure different parameters (a set of FBG can include sensors to measure deformations, temperature and humidity).

The fiber optic has a *low signal attenuation* which makes it possible to place the interrogation unit at very high distance (even tens kilometers) from the sensor network. So this monitoring system can be used to monitor structures that are in areas where there is no electrical energy. Fiber optic transmits the signal from sensors to the interrogation unit without the need of amplification up to 50 kilometers.

Other advantages can be the practicality and the *economy* in the installation and the ability to convey information at high speed.

2.3 FBG SENSORS

FBG sensors can be considered strain gages able to measure deformations of the structures on which they are installed. They are the most used and reliable sensors to measure deformations. Measurements are possible thanks to photo-engraved gratings in the core of the fiber: the Bragg gratings. Their dimension is between 5 and 10 millimeters. These gratings are realized through the photo-incision process which generates a periodic variation of the refractive index. They are obtained when the core of the fiber is exposed periodically to intense ultraviolet light. The exposition determines a permanent increase in the index which can be different according to the type of exposure. The refractive index along the longitudinal axis z of the fiber in the section occupied by the grating is:

$$n(z) = n_0 + \Delta n \cdot \cos\left(\frac{2 \cdot \pi \cdot n}{\Lambda}\right)$$

where:

n = refractive index;

n_0 = average value of refractive index in the core (~ 1.5);

Δn = n_0 modulation (10^{-4});

L = grating pitch (~ 0.5 mm);

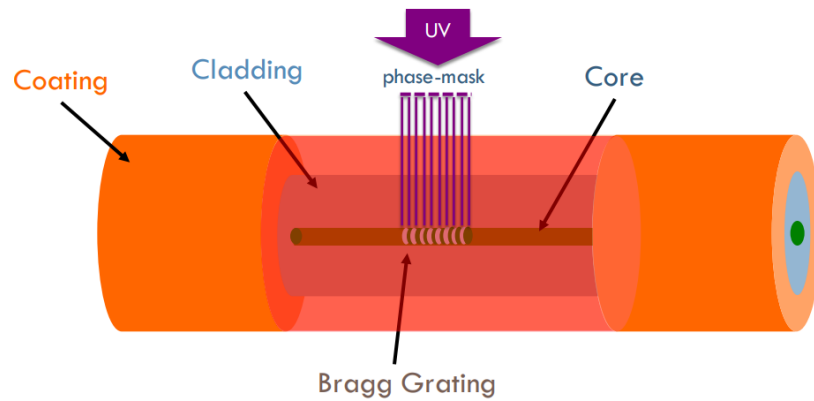


Figure 2.4 Bragg Grating in FBG sensor

If a drop of ultraviolet ray with a spatial period L is projected into a dopant fiber, the same spatial period L of refractive index distribution is copied into the core of the fiber due to its ultraviolet photosensitivity (Chen, et al., 2000). This ultraviolet treated fiber with periodic index distribution is FBG. Corresponding to the pitch L of this fiber grating, there exists a Bragg wavelength λ_B :

$$\lambda_B = 2n_{eff}\Lambda$$

It is possible to calculate spectral function of a low reflection Bragg grating. The spacing of the Bragg grating grid is obtained by the formula:

$$\Lambda = \frac{\lambda_0}{2 \cdot n}$$

$n = 1.46$ typical value for FBGs

if $\lambda_0 = 1550$ nm

$$\rightarrow L = 530 \text{ nm}$$

If it is known the length of the grating for example $G_l = 6$ mm, we calculate the number of fringes N present in the grating itself:

$$N = \frac{G_l}{\Lambda}$$

When multi-wavelength light is launched into the fiber, only the component of wavelength λ_B is reflected by FBG. If FBG is stretched, the Bragg wavelength of FBG will be changed with the change of pitch L . We can embed FBG in the structures so it is considered as a wavelength-coded strain sensor. It is possible to introduce several FBG sensors in the same fiber serially with different pitch L , every sensor can measure the strain corresponding to its location independently. In this way a quasi – distribution of structural strain can be easily measured with FBG sensors system.

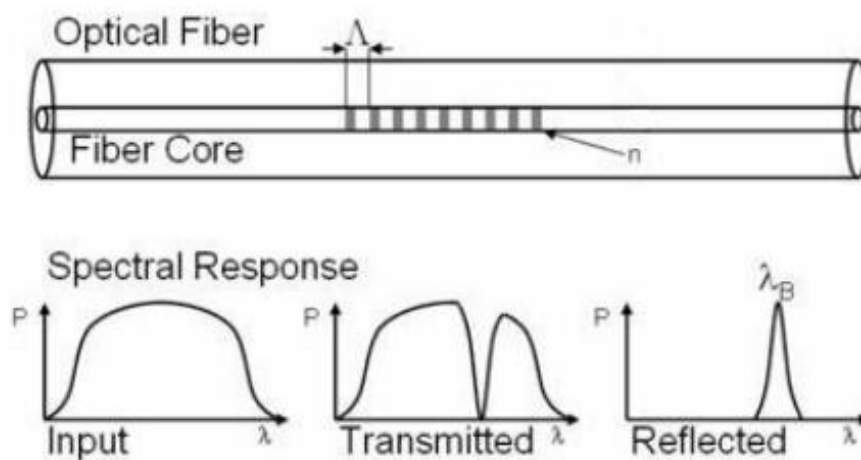


Figure 2.5 Operation of FBG sensors

The fluctuation of temperature can change the pitch of FBG sensors, for this reason the multiplexing capacity of an FBG sensors system is limited by the light source. Many schemes were proposed to compensate the temperature effect and to enlarge the volume of multiplexed FBG sensors. Thus, large volume systems being capable of multiplexing dozens of FBG sensors are widely used in many different countries. For example, in 1995, 45 FBG sensors were embedded in a single – lane of I-10 Bridge at New Mexico State, USA to monitor static and dynamic strain. Another important work was the introduction of 128 FBG sensors for monitoring the long-term performance track of a bridge in Canada.

To summarize we can use the Bragg grating as a sensor when it is fixed to a structure that transmits its deformations to the optic fiber: elongation or compression of the FBG sensor causes a change in grating period resulting in a change in wavelength of the reflected ultraviolet light. FBGs reflect wavelength which have very small bandwidths (so-called peaks in the spectrum). The initial period is a known parameter so we can measure the deformation applied to the grating analyzing the displacement of the reflected wavelength.

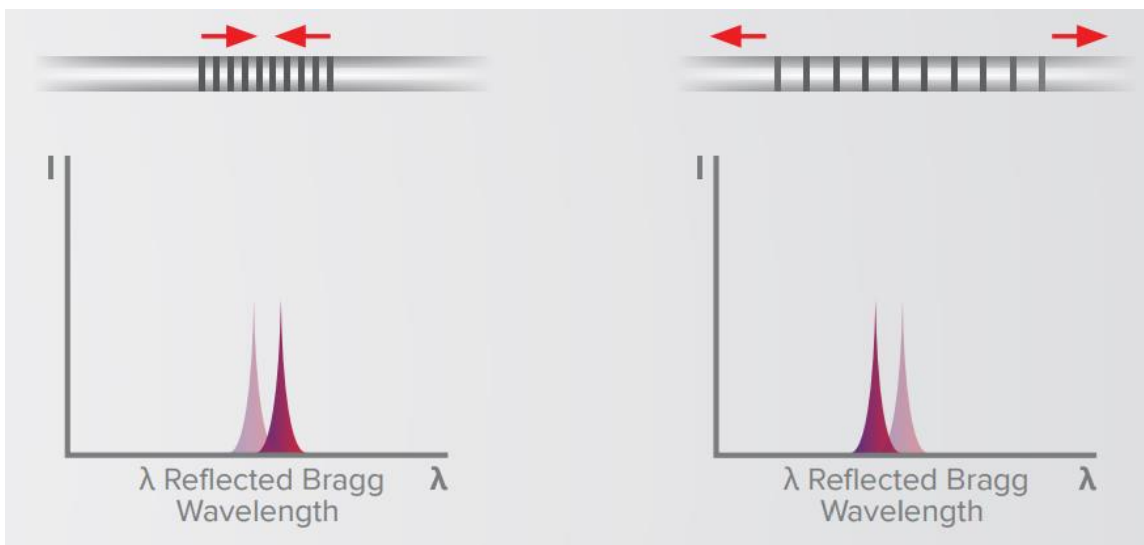


Figure 2.6 Application of tension and compression in a fiber with a FBG sensor

The Fiber Bragg Grating is also sensitive to temperature. In this case the main contributor to Bragg wavelength change is the variation of the silica refractive index, induced by the thermo - optic effect. There is also a contribution from the thermal expansion, which alters the period of the microstructure. This effect is, however, marginal given the low coefficient of thermal expansion of silica.

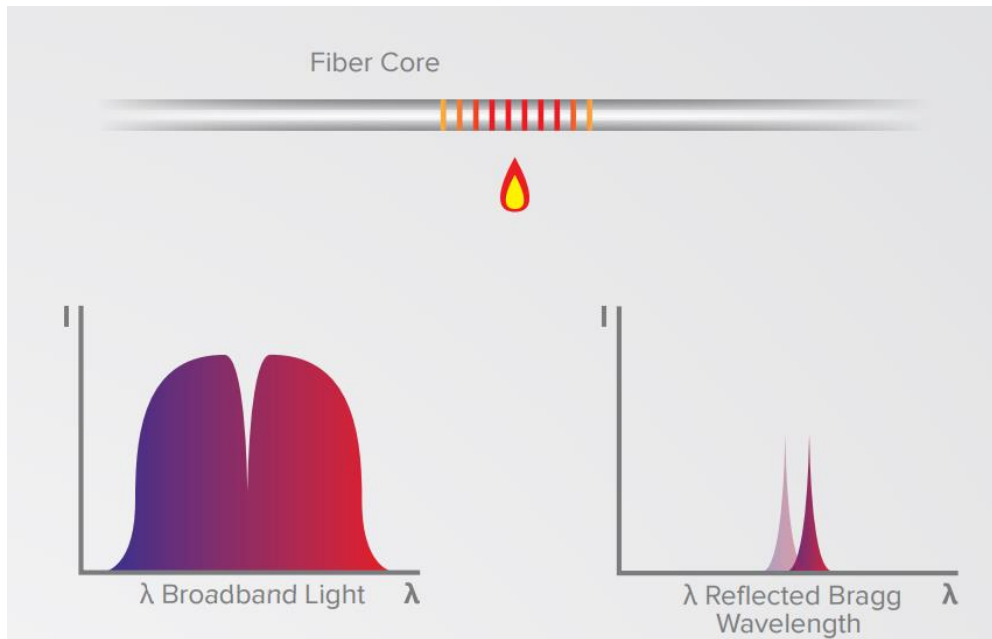


Figure 2.7 Temperature variation in a fiber with a FBG sensor

A variation of the period of the grating inscribed in a fiber optic - induced by thermal or mechanical perturbation - causes a shift of the reflected peak wavelength, due to related optical path length variation. This is expressed by the formula:

$$\Delta \lambda_{Bragg} = 2 n_{eff} \Lambda \left(\left\{ 1 - \left(\frac{n_{eff}}{2} \right) [P_{12} - \nu (P_{11} + P_{12})] \right\} \epsilon + \left[\alpha + \frac{\left(\frac{dn_{eff}}{dT} \right)}{n_{eff}} \right] \Delta T \right)$$

where:

P_{ij} = Pockel coefficients of the elasto-optic tensor;

ν = Poisson coefficient;

ϵ = is the applied deformation;

α = thermal expansion coefficient of the fiber;

ΔT = temperature variation;

By replacing the typical coefficient values for a fiber optic in the FBG formula, the Bragg wavelength shifts due to strain or temperature are of the order of 1pm/me for strain and 10 pm/ °C for temperature. It is evident from the formula that is impossible to separate the two effects from one another.

When FBG sensor is fixed to the structure in a region without temperature variations, it measures strain and stress without any influence of temperature. On the contrary when there are both temperature and strain changes we will put two different FBGs to compensate the data. For example a strain-gauges sensor can have two different FBGs inside: one used to measure only temperature and the other one measures together temperature and strain. The two values can be compensated to obtain the only strain measure.

The connection between unit and sensors is ensured via standard telecommunication fibers. A distance between unit and sensors can be up to several tens of kilometers. Therefore you can cover a large area with one unit and lots of sensors. Being the measurement for each grating a reflected wavelength, which is an absolute parameter, there is the possibility of turning off or changing the measurement unit without the need to calibrate or determine a new zero.

2.4 DISTRIBUTED FIBER OPTIC SENSING

Among many emerging sensing technologies, Distributed Fiber Optic Sensing (DFOS) is one of the promising tools for structure health monitoring. The invention of optical fiber can be considered one of the greatest technological achievements of the twentieth century. The concept of transmitting light waves over very long distance using optical fiber was developed by Nobel laureate Charles Kao in 1960s and Corning glass laboratories produced optic fiber to realize this in the 1970s. Optical fiber has become with laser technology one of the key components for the optical communication revolution (Soga, et al., 2018).

One of the characteristic of optical fiber which has contributed to its development is low-loss, the distributed fiber optic sensors (DFOS) can measure physical quantities such as temperature, strain and vibration of the fiber continuously at discrete points with very small spacings (say 5 cm) along its length for long distance (about 10 km). We can attach an optical fiber cable to all the structure or embedding it inside the structure so it is possible to monitor the changes of ambient parameters of the structure. The sensor is robust to high-voltage environments, electromagnetic interference, corrosion and other harsh environmental conditions (Deng & Cai, 2007; Habel & Krebber, 2011).

Distributed optic fiber sensors are particularly useful when it is necessary to obtain measurements about a large number of points or continuously along all the length of optical fiber. Typical applications are:

- Monitoring of strains in large structures such as bridges, dams, tunnels, buildings, tanks, ships;
- temperature measurements in electric power transformers, generators, gas pipelines, oil pipelines;
- identification of leaks in pipelines, fault diagnostics and detection of electrical or magnetic anomalies in electricity distribution systems;
- real-time evaluation of strains, vibrations and temperature in composite materials with sensors incorporated in them, in field such as the aerospace industry.

The distributed sensors have a lower cost than punctual ones. They manage to find the critical point of the system with a centimeter accuracy over several kilometers and capture temperature variations of half a degree Celsius. The best known are based on Brillouin, Raman and Rayleigh scattering.

Scattering is considered a physical phenomenon where waves, like light, are forced to deviate from a straight trajectory when the material that is passing is non-uniform.

We can consider a light wave which is travelling through the core of an optical fiber, it interacts with the atoms and molecules of the core. The electric field generates a time - dependent polarization dipole, if its wavelength is far from a medium resonance (Boa, et al., 2012). Thus a secondary electromagnetic wave is generated by the induced dipole and this is called light scattering (Soga, et al., 2018).

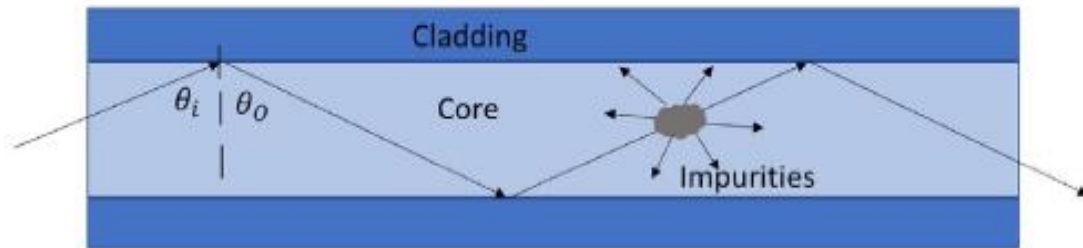


Figure 2.8 Scattering of incident light

When the medium is perfectly homogeneous, the phase relationship of the emitted waves only allows a forward scattered beam. However, every medium has impurities, causing back scattering that changes the light transmitting direction. When a fiber experiences a strain or temperature change, there is density fluctuation, which in turn changes the characteristics of the back scattered beam.

In the 70s there was a great development in the use of optical fiber in telecommunications field. It became necessary an instrument that could locate faults in the fibers, regions of large anomalous losses and bad junctions. Thus it was born the optical reflector in the time domain (OTDR). It is considered a one-dimensional optical radar (LIDAR). An optical pulse from a laser is launched into the fiber and the light, due to the diffusion of Rayleigh, is continuously reflected backwards during propagation. The back-diffused optical power emerges from the launch terminal and it is analyzed as a function of time to provide a differential map of the spatial distribution of the optical attenuation along the fiber. It can be considered the first distributed fiber optic structural monitoring system. It allowed spatial measurements of any external condition which can influence the attenuation of the fiber, such as those caused by a torsion or a break. This instrument had the only problem that

attenuation was not so sensitive to strain, pressure, temperature etc. for this reason the attention was turned towards other parameters such as polarization and phase. The first method developed took into account the polarization. The device was very similar to the OTDR but it analyzed the polarization state of the back-diffused light as a function of time. It was realized the optical polarization reflectometer in time domain (POTDR) which maps the spatial distribution of the polarization properties of the fiber and any parameters that change it. The polarization properties are sensitive to many external agent such as temperature, strain, pressure, etc.

This passive, one-dimensional and dielectric device was installed on different structures with minimal intrusion: bridges, dams, airplanes, oil pipelines, boilers, pressure pipe.

In the 1970s the backscattering effect was studied in detail. Scattering effects were used to characterize loss and defective properties along the fiber resulting in the invention of OTDR (Optical Time Domain Reflectometry). Nowadays OTDR is employed widely in fiber communication technology to measure fiber length and attenuation. OTDR technology opened the way to other light scattering effects: Raman scattering and Brillouin scattering were introduced for various distributed sensing applications (Soga, et al., 2018).

When a light is launched in the fiber, backscattered lights are generated at every point of the fiber. A backscattered light coming back earlier in time is the one close to the original launching point.

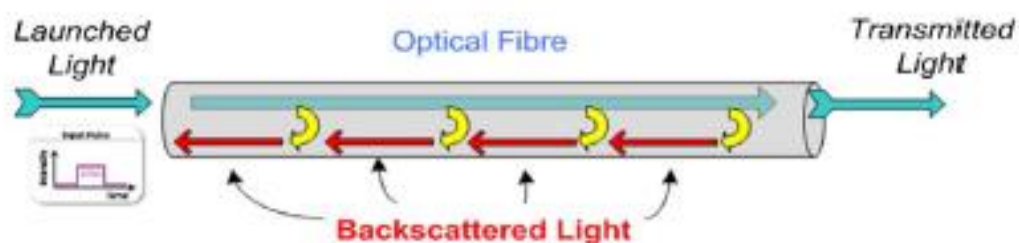


Figure 2.9 Backscattered lights from different locations of fiber

We have two different big categories of physical scattering: elastic scattering and inelastic scattering. Both types of scattering occur simultaneously in the medium, but with different power levels. The elastic scattering is a linear collision process which does not change energy of photons. It is often called Rayleigh scattering. The frequency of a Rayleigh scattered reflected light is the same as that of the input light. The scattered power is considered proportional to the power of the input light. This type of scattering is mainly used for vibration monitoring for civil engineering applications (Soga, et al., 2018). The cost of the sensors which use this technology is not very high even in the equipment used. The accuracy and the sensitivity decreases with the interrogation unit distance, with the proximity of one sensor to the other and also with the presence of curvatures and damage along the fiber.

On the other hand, inelastic scattering is a nonlinear collision process that changes the energy of photons. The Brillouin scattering involves the interaction of incident light with acoustic photons, whereas the Raman scattering involves the interaction with optic photons. In the next paragraphs we will see in more detail the different classes in which distributed optical fiber sensors (DOFS) can be distinguished.

2.4.1 SYSTEMS BASED ON LINEAR DIFFUSION BACKING

In this class the propagation of the optical pulse occurs in linear regime and the light reflected by the impulse is calculated as a function of time and it is analyzed to provide the spatial distribution of the parameter.

Linear systems are less complex and less demanding regarding source requirements and fiber properties than non-linear systems. OTDR was the first to be based on linear diffusion. It consists in launching an impulse from one side of the fiber and then measuring the reflected intensity as a function of time on the same side. We can define t like the delay between the impulse launch and the time when the light is received. Thus, the fiber section when the retro-diffusion takes place is identified at a distance s from the fiber launch terminal:

$$s = \frac{vT}{2}$$

where v is the speed of light in the fiber. In particular conditions this technique of temporal resolution is not useful and it may not provide the required sensitivity because the levels of reflected power are very low (about 10^{-6} of the impulse power per meter of fiber). Therefore, other techniques are available, for example based on frequency modulation: optical reflectometer in frequency domain (OFDR). The spatial resolution of an OFDR can reach 10mm, although the measurement range decreases after few tens of meters.

In the Rayleigh diffusion the wave (which propagates in the core of the fiber) interacts with the diffusion sources, impurities of silicon and other particles with smaller dimensions compared to the wavelength. Interactions give rise to a partial reflection in the order of 10^{-7} m^{-1} . Thus, local modifications of the optical fiber can be identified measuring the variations in intensity in the retro-reflected signal with respect to the initial signal: an abrupt peak of return can be interpreted as a reflection due to connectors or damage on the fiber; also an improper decrease in intensity can be the cause of a loss due to a break along the fiber.

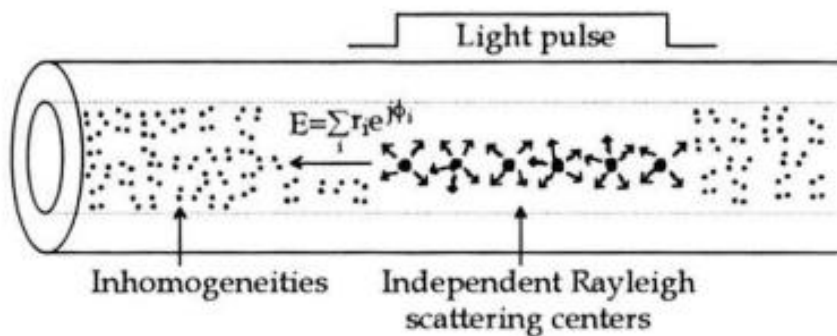


Figure 2.11 Rayleigh diffusion

The variation in light intensity can not be directly correlated with the strains of the structures on which the optical fiber is installed. The value of the Rayleigh back-spreading signal should be associated to optical fibers preliminarily equipped with specific sensors such as 'microbend' sensors or other configurations that incorporate pre-calibrated losses to perform strains measurements.

Another method which uses linear retro-diffusion is the optical polarization reflectometer (POTDR). It resolves the polarization state of the back-diffused light as a function of time. Thus we have a spatial distribution of the properties that influence the polarization.

One of the problems of linear retro-diffusion is that sometimes it is not easy to identify the parameter measured.

2.4.2 SYSTEMS BASED ON NON LINEAR RETRO-DIFFUSION

The main difference between this class and the previous is that the optical pulse has sufficient peak power to enter in non-linear regime. The reflected power will be analyzed differently than before. They require high-power pulse sources and particular fibers due to non-linearity. But they provide a wider range of interactions of parameters with the fiber and a rapid ability to identify the signal to the receiver. The Raman technology can be considered the first example of non-linear retro-diffusion. One of the first advantages is the possibility to use any type of fiber. The intensity of Raman diffusion is about 30 dB weaker than Rayleigh diffusion but the temperature sensitivity is very high. The Raman diffusion allows only measure of temperature not strain. The vibrations and the molecular rotations allow to modulate the light which propagates inside the fiber. In this mechanism the photons from the incident light interact with the optical photons of the material structure (Boyd, et al.). In particular a photon strikes a molecule and it is absorbed, then there is a re-emission of a photon with a different energy compared to the original one. The number of excited molecules depends on the temperature. The radiation with lower

photon energy is known as Stokes light while that with higher photon energy compared with the origin wave and it is known as anti-Stokes light. Soga in his article written in 2018 says: “The Stokes and anti-Stokes of the Raman scattering happens at about ± 13 THz away from the incident light frequency which is in the order of 193.5 THz for 1554nm laser”.

An optical pulse with a high power is launched in an optical fiber at frequency ν_1 . A frequency range ν is chosen and the radiation levels are measured in small range around ν_s and ν_a :

$$\nu_s = \nu_1 - \nu$$

$$\nu_a = \nu_1 + \nu,$$

where ν_a and ν_s are respectively the Stokes and anti-Stokes frequencies. The powers of the two waves are not identical. The dependence of the anti-Stokes radiation on the temperature is normalized dividing it by the level of the Stokes radiation. So all the effects that cause losses (torsion, attenuation of the fiber material ect.) except temperature are eliminated. The ratio of the two powers is related to temperature at the scattered location. It can be expressed with the formula below:

$$R(T) = \left(\frac{\nu_a}{\nu_s} \right)^4 e^{\left(\frac{h\nu}{kT} \right)}$$

where:

h = Planck's constant;

k = Boltzmann's constant;

T = absolute temperature.

When the temperature changes at a section, the Ratio changes at that section. By monitoring the ratio change at every point of the fiber, the temperature change profile can be obtained (Soga, et al., 2018).

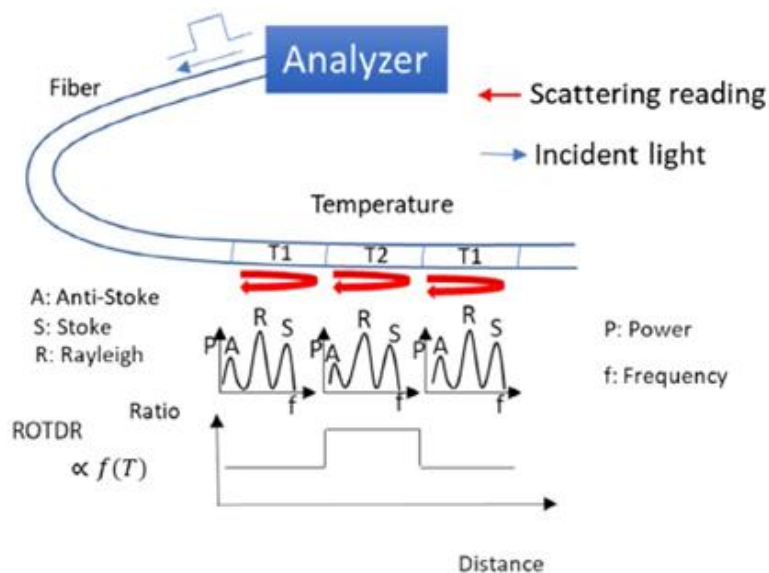


Figure 2.12 Raman scattering generated by temperature change along a fiber

An important feature of this technique is that every fiber already installed can become a distributed temperature sensor (up to 10 km) regardless the purpose for which it was installed.

If we use multimode optical fibers the resolution is of the order of 0.1 ° C for the temperature and the spatial resolution is 1 meter for distances up to 10 km. The Raman diffusion was introduced to monitor oil wells and to identify leaks in earth dams.

Another no-linear retro diffusion technology is Brillouin diffusion. It consists about an interaction between acoustic and optical waves which propagate in the fiber. The acoustic waves, which travel at about 6 km/m, are generated spontaneously by thermal excitation. When it happens we can speak about spontaneous Brillouin diffusion.

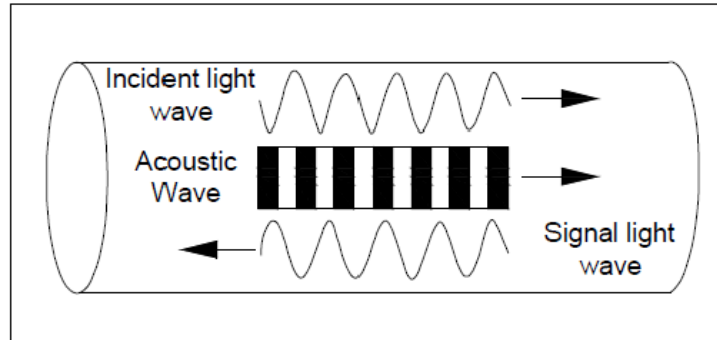


Figure 2.13 Brillouin sensor

The diffusion is the result of a Bragg-type reflection on mobile gratings. These are created by variations in the refractive index causing acoustic waves that propagate in the material along the main axis of the fiber. The reflected Stokes wave comes from an acoustic wave that propagates in the fiber moving away from an impulse generated by the optical pump while the anti-Stokes wave is born from an acoustic wave that moves towards the impulse. The Brillouin diffusion changes the frequency of Stokes and anti-Stokes waves:

$$\nu_B = \pm \frac{2n\nu_a}{\lambda_p}$$

where n is the index of refraction of the fiber material, ν_a is the acoustic speed, λ_p is the wavelength which is pumped into the free space. The intensity of reflected light is detected as a function of the frequency shift and flight time: the frequency shift gives us the deformation and the flight time provides the location where the deformation occurred.

The main difference between Raman and Brillouin diffusion is about excitement. There is a movement of large quantities of molecules in Brillouin diffusion, while there is only rotation or vibration of single molecule in Raman diffusion.

Strain monitoring with Brillouin based scattering was proposed and demonstrated in 1989. Today it can be used to monitor also temperature. If temperature and strain change simultaneously in the same section of the fiber, it

is not possible to distinguish the two single effects. To overcome this problem one half of the fiber should be located to measure temperature variations while the other half should be constrained to the structure and it will measure both temperature and deformation variations. The two halves should be placed next to each other so it is possible to identify the two effects.

The spatial resolution is larger when measurement distance is long. It can be used from 1 km to 70 km. The precision is about 40 me in strain and 2 °C in temperature. A recent application of this technology concerns the detection of chemicals.

The stimulated Brillouin diffusion is introduced when we need a signal with a bigger power and to take measurements over large distances.

2.4.3 NON LINEAR SYSTEMS BASED ON CO-DIRECTIONAL DIFFUSION

The co-directional diffusion consists in the interaction of two counter-propagating radiations (a pulse and a continuous wave or two pulses) inside the fiber. When the non-linear interaction is influenced by an external parameter, the value of this parameter along the fiber can be mapped.

A pulse of light at high power is launched into the fiber; it generates a non-linear effect during propagation. A continuous wave shows non-linearity when the impulse passes through it. The temporal variation of the continuous wave maps the passage of the pulse that passes through it so if the non-linear interaction is influenced by an external parameter, it is mapped along the fiber.

This technology presents the same advantages and disadvantages as systems based on non - linear backscatter. However, it has the advantage to have a higher signal level and therefore they have a bigger signal/noise ratio. On the other hand the disadvantages are: the necessity to have two different optical sources and access to both ends of the fiber.

2.5 CONSIDERATION ABOUT INTEGRATION OF FIBER OPTIC SENSORS IN STRUCTURES

Structures realized with composite materials with an embedded fiber optic detection system allows a constant monitoring about internal deformations, state of stress, vibration, temperature and about the general health condition of the total structure. Using this configuration it is possible to increase the quality of the processing control of the structure during the manufacturing process. Therefore a reduction in the number of maintenance operations is obtained. Furthermore if we constantly monitor the loads and the strain of an element we can have informations about its fatigue state during all its life time.

Fiber optic sensors are extremely small and light, they are resistant to fatigue and corrosion and they are also immune to electromagnetic interference. They can not trigger sparks or explosions: all these characteristic make them ideal for their integration in composite materials. To do this it is important to develop a new know – how in different fields:

- orientation and arrangement of the sensors;
- behaviour of the material and structural properties with the introduction of this detection system;
- dynamics in interaction between sensors and material of the structure;
- search for the most reliable and least intrusive method for the interface.

It has been shown that if optical fiber is used like deformation or temperature sensors they must be placed between two collinears layers of the composite material and they also should be introduced in the same direction of reinforcing fibers. Alternatively, when optical fibers are used as sensors to measure damage, they must be located as close as possible to the surface where it is present the maximum value of stress. It is

also necessary to locate the fiber in an orthogonal way between two layers of collinear reinforcement.

One of the most important problem is to understand if the introduction of fiber optic sensors in composite materials can compromise tensile or compression resistance and reduce the fatigue resistance of the material. If we introduce the fibers in the structure with an inclination with respect to the adjacent layers, they create the “resin – eye”. It is considered the angle between the optical fiber and the reinforcement direction of the material. This angle reaches its maximum amplitude when the fiber is orthogonal to the adjacent layers. However, if we place the fibers in a way that is collinear with the reinforcing fibers, there is no resin-eye and the characteristics of the material do not change appreciably. The “resin-eye” is consider a factor of intensification of the efforts.

In the last ten years a great number of experiments have been conducted and they have been established that the introduction of optical fibers embedded in the structure leads to an improvement in the resistance of the material to damage. An optical fiber with a diameter which is less than 140 mm does not change the strength characteristics of the structure.

Further experiments will be conducted on the diameter and on the coating of the optical fibers to avoid reduction in the performance of sensors embedded in the structure.

2.6 NBG SYSTEMS ACTIVITIES

NBG is a company leader in the fiber optics sector. It is located in Gmund (Austria) and it has almost one hundred engineer. It is specialized in the production and distribution of optical fiber. NBG uses its fiber in many different fields: starting from safety, it monitors bridges and railways without forgetting pylons, gas pipelines, oil pipelines and tunnels. It works mainly in Austria and the Czech Republic but also in other European countries. In the last few years it has also started to cooperate with American companies. The company is the first and only preform factory in Europe.

NBG Fiber GmbH is able to produce European quality preforms for 5,2 million fiber optical kilometer per year.



Figure 2.14 Different uses of optical fiber

NBG try to develop new safety technology for our daily life every day. Online observation 24/7 of speed, weight and position of trains and rails gives information about the actual condition. If metrics differ from normal conditions, safety actions can be executed. Rail transport is one of the most employed means of transportation with an ever increasing number of passenger traffic. Therefore efficient monitoring devices are crucial to reduce maintenance costs and improve the safety of passengers and goods. Many rail systems have the potential to adopt optical fiber sensors due to the optical fiber communication infrastructure already being present. This way is possible to deploy a monitoring system with minimal disruption of the infrastructure.

The fiber optic sensors can also be used in Weight-in-Motion Fiber Optic system. They are installed under the top layer of the road, making them maintenance free and

insusceptible to failure. The sensor is constructed from different segments which can measure and record large amounts of detailed information.

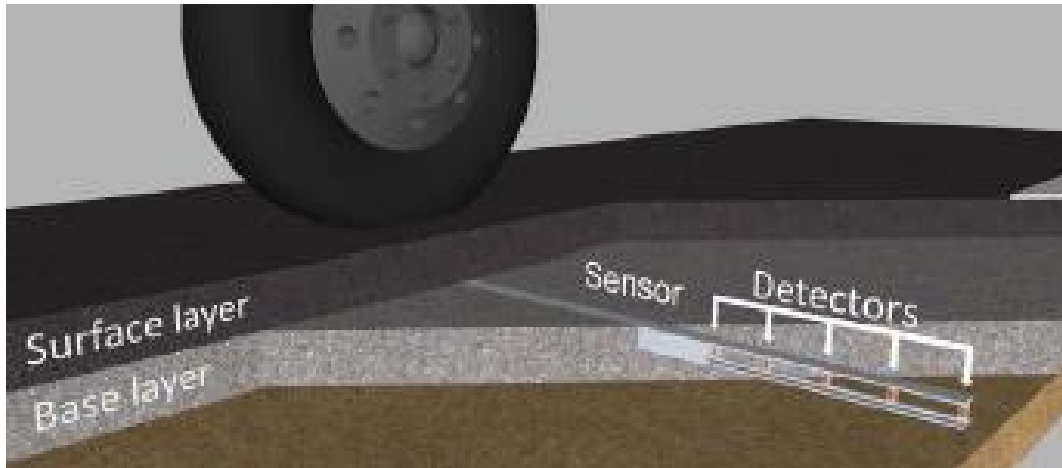


Figure 2.15 Sensors in the top layer of the road surface

On the contrary, in the conventional systems, the sensors and detection loops are installed in the top asphalt layer. This means that the sensors are installed in grooves cut or ground into the asphalt after the asphalt is laid. Due to wear and rutting of the asphalt, the sensors must be replaced or adjusted on average every 1.5 years. Furthermore temperature variations in the summer and winter cause the sensors to separate from the asphalt, requiring the repair of both the sensor and the road surface. This is very expensive.

NBG realizes monitoring systems also for dams. Typical dam safety surveillance consists of visual inspections supported by limited instrumentation. However, the problems in dams can become quite advanced before the problem is detected via these means. Visual observation cannot quantify the extents or depths of distress conditions. FBG proposes a quasi distributed fiber optic sensors to obtain measurements at many points along the fiber-optic cable. The image below shows an example.

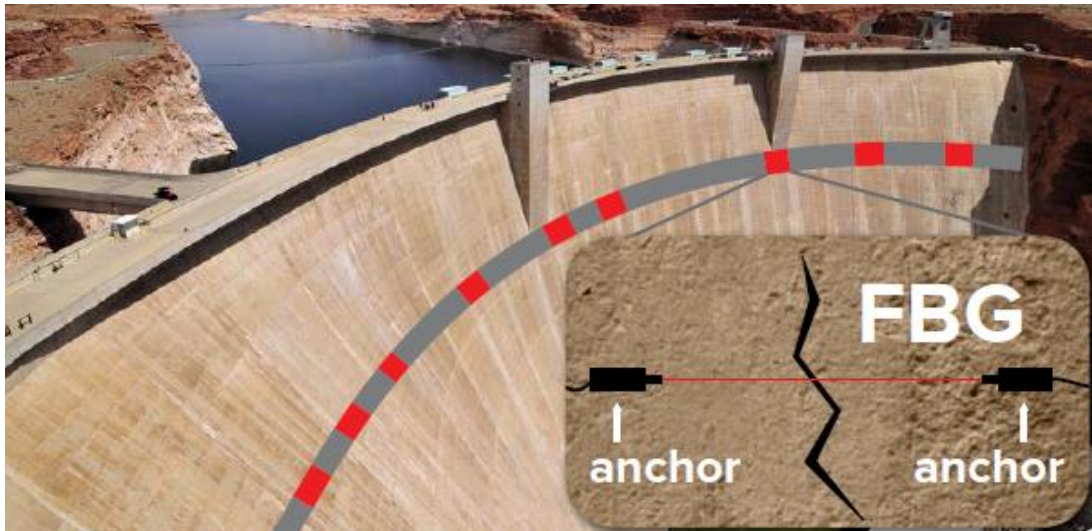


Figure 2.16 Quasi Distributed Fiber Optic Sensors in a dam

Another field of application for NBG engineers is the infrastructure protection. The intrusion detection system PeriGuard is a security system based on the fiber optic sensing technology and is designed for short and medium perimeter applications with up to sixteen detection zones per unit. All zones operate autonomously and use the same interrogation unit; a sensing cable failure or an intruder on any zone will not affect the performance of any other zone. The sensors can be placed also under subsoil, rocky ground, desert with sharp stones, new grass, sand and mixture between all of these. Some are designed to penetrate water, this is especially important when they are installed under grass, so that there is no difference between “normal” grass and grass where a security zone is.

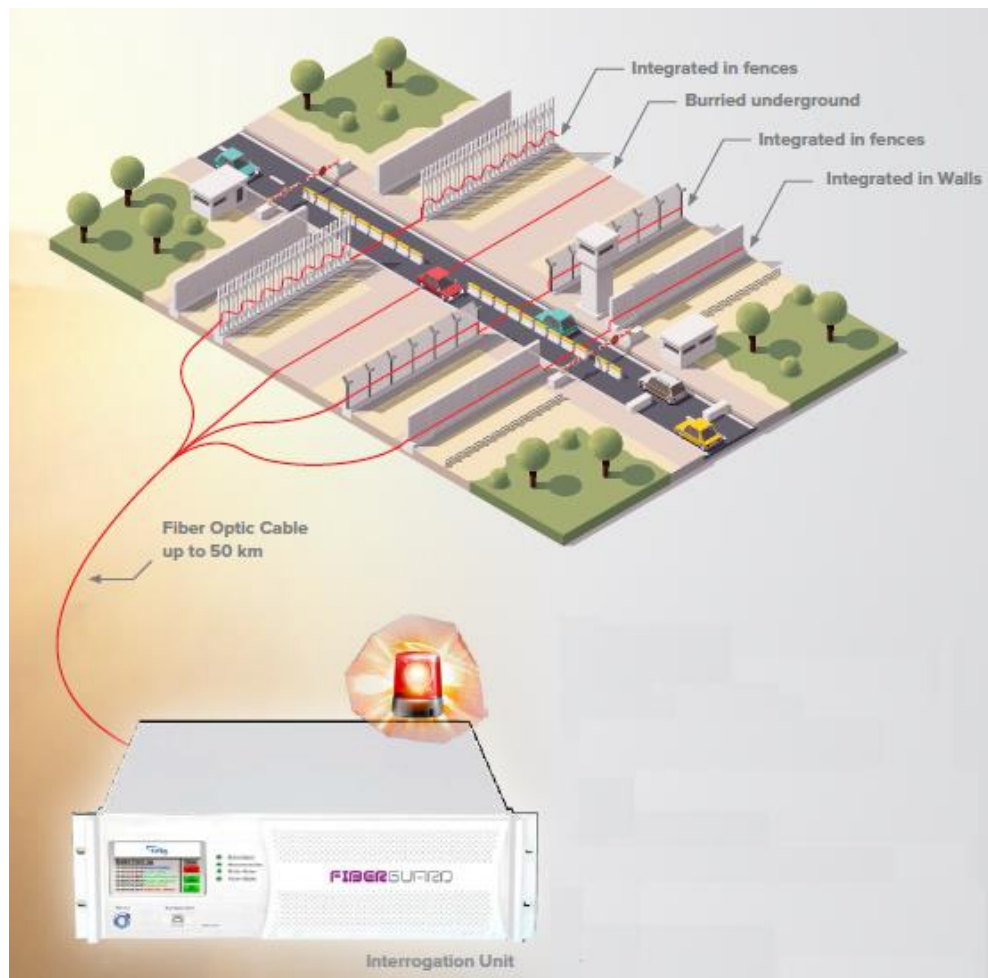


Figure 2.17 Fiber optic sensors for security

NBG fiber optic sensor technology is used to monitor pipeline leakage. Distributed Temperature Sensor (DTS) is used for leakage detection, namely where a leakage causes local temperature anomaly – in the case of liquid gas or isolated steam tubes. DTS can quickly and reliably detect and localize anomalies and if necessary trigger an alarm or an emergency stop of the system. Distributed Temperature and Strain Sensor (DTSS) can allow operators to anticipate failures at a very early stage and to avoid the huge costs associated with pipeline failures. These threats can lead to catastrophic consequences for people, communities and environment.

3. CASE STUDY: CANNARA BRIDGE

We have decided to experiment fiber optic sensing on the Cannara bridge located in Perugia. The behavior of the bridge was already studied in 1997 after the earthquake occurred on 26th september in 1997. This earthquake had a magnitude of 6.0 and a maximum intensity of IX in Mercalli scale intensity. There was the collapse of the Basilica of San Francesco in Assisi which caused the death of four people.



Figure 3.1 Perspective of the Cannara bridge

The professors and engineers A. L. Materazzi and R. Baldi studied the bridge to understand what was its state of the art at that time. In the technical report written by the two professors there is already evidence of cracks which involve the upper slab and the main arch. The professors identified the introduction of a cylindrical hinge. It had been changed the original static scheme of the bridge. They hypothesized that the reason of that situation was due to a yielding of one abutment which would have caused tensile failure of the slab and the introduction of a plastic hinge in the main arch at the most damaged arch (opposite to the center of Cannara). This hinge became the center of a rigid rotation of one part of the structure. It defined the the crack opening and the movement of the two edges of the slab. The value related to the distance between the two edges of the slab was equal to 10 mm in 1997.

To sum up we can say that there was a relative rotation between the two parts of the bridge around a center of rotation. The yielding was related to the foundation closest to the damaged arch and not the one towards the city center of Cannara. This produce a greater tensile stresses in the upper fibers in the section of the plastic hinge while

the rest of the structure remains in the elastic field. Furthermore, the hinge produced a kinematic mechanism which caused a crack on the road surface.

The analysis carried out by the professor Materazzi identified a yielding of the foundation on the opposite side to the Cannara center equal to:

$D_z = 0.94 \text{ cm}$ (vertical direction)

$D_y = 0.80 \text{ cm}$ (horizontal direction)

$D_f = 0.1316^\circ$

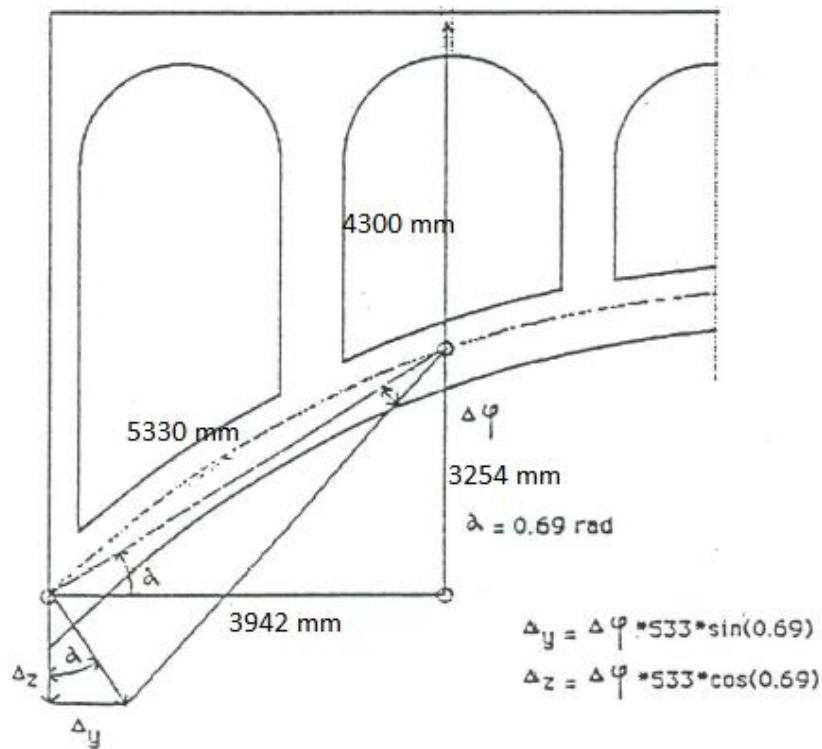


Figure 3.2 The yielding calculated by the professor Materazzi

In the report the professor wrote that the movement of the abutment had already settled so it was not necessary to repair the bridge immediately. The only restriction was related to the traffic: it was not permitted the transit to vehicles weighing more than 38 tons.

3.1 ARCH BRIDGES

Nevertheless, the use of the arch has old origins, Leonardo da Vinci (1452-1519) was one of the first scholars who succeeded to understand how the arch works. It is not possible to define a departure date but certainly the first remains of arched structures date back to the Mesopotamian civilization (IV and III millennium B.C.).

Many arched structures were built in centuries later, but only in roman period the arch find its first period of great diffusion. The Roman bridges were in circular-shaped masonry. Today more than three hundred of that are still used. In the Middle Ages, arched bridges began to change their shape and to become lighter and leaner thanks to the evolution of construction methods. Therefore, they started to reach bigger span. An example is Ponte Vecchio in Florence. It is one of the first depressed bridges in the history. The first concrete arched bridges appeared at the end of the nineteenth century. The concrete was suitable for this type of structure because it is resistant to compression. Concrete bridges are considered the heirs of masonry ones. They have the advantage to have desired shapes thanks to cast in the formwork. The concrete behaves very well with compression stress while it presents a fragile collapse behavior with bending stress. For this reason it was match with steel. The goal was to overcome the limits of the concrete with the exploitation of tensile strength properties and the ductile behavior of steels. The arch transforms stresses produced by vertical loads into compression stress minimizing the bending moment component. It is resistant to vertical loads thanks to the geometric axis variation and the presence of horizontal thrust applied to curved elements. The bending moment values are negligible compared to those measured in the beam in the same configuration and with the same load. The formula below represents the flexural behavior of the arch:

$$M_{\text{arch}} = M_{\text{beam}} - S * Z$$

It is possible to see that the moment applied in each section of the arch is reduced compared to the corresponding one in the case of beam. The difference is equal to the product of the horizontal thrust multiplied by the height of the analyzed section.

It is not possible to study arch bridges with the “Theory of the first order”. It is not correct to consider the De Saint Venant hypothesis of “small or infinitesimal displacements” in structures with high lowering and slenderness. Therefore, it is necessary to study the equilibrium of the structure in the deformed configuration.

If the arch decreases, the value of the horizontal thrust increases. The second order theory takes into account the non-linear behavior present in this type of structure by referring to the P-D effect which considers the influence of normal stress on the flexural deformation of the arch (Margiotta, 2011).

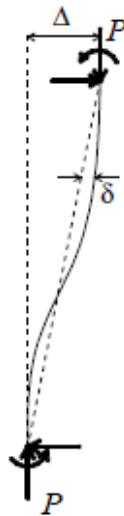


Figure 3.3 Second order theory P-D

In general, if we consider restraint conditions we have three different types of arch bridges:

- Three hinged arch bridges
- Two hinged arch bridges
- Fully restrained arch bridges

The three-hinged arch is an isostatic structure. The pressure curve is forced to pass through the three hinges. The main advantage of this type of structure is its insensitivity to temperature variation and to the differential yieldings of the constraints. This type has not been very successful because it is not very suitable to withstand dynamic loads such as traffic loads. The thrust acting at the hinges at the base depends on the lowering 'f' of the arch. If the arch decreases, the thrust increases.

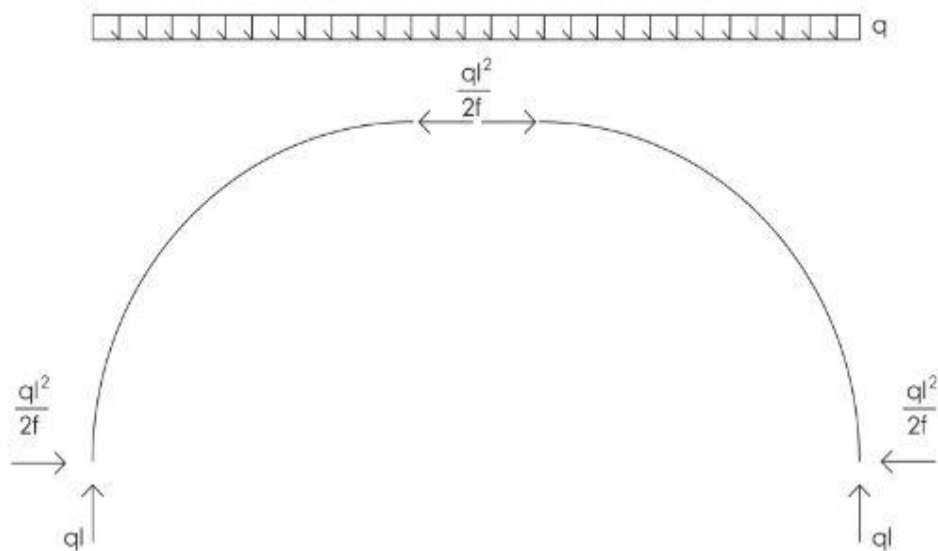


Figure 3.4 Three-hinged arch

The two-hinged arch is mainly used in steel bridges. It is a hyperstatic structure. The pressure curve is forced to pass through the two hinges placed at the base of the bridge. The horizontal component of the reactions must be calculated with an elastic analysis because the structure is once hyperstatic, while the vertical components are the same of a supported beam of equal length as for the arch with three hinges. This type of arch has a good behavior with mobile load. However it is sensitive to the phenomena of viscosity and shrinkage of the concrete and to thermal variations.



Figure 3.5 Maria Pia Bridge, Porto (Portugal), 1877. (Troyano, 2006)

The fully restrained arch bridges is a structure with 3 degrees of freedom. The pressure curve has no obligatory passage. It is suitable to support mobile loads and it has a lower deformability compared to the arch bridges seen previously. However the fully restrained bridge is sensitive to thermal variations, long-term phenomena and yielding constraint.



Figure 3.6 Los Tilos Bridge, La Palma 2004. (Troyano 2006)

3.1.1 MAILLART'S BRIDGES

Robert Maillart encouraged the development of reinforced concrete in construction techniques during all his life. He decided to use the arch as a structural shape for his bridges. He was the first who realized a bridge joining the different parts of the supporting structure into a monolithic unit (Zuoz 1901). Zuoz Bridge is a three-hinged arch bridge. Two years after its construction it showed damages near its abutments. In this region cracks appeared due to horizontal stiffening.



Figure 3.7 Zuoz Bridge, Zernez, Maillart 1901

One of the most important work of Maillart is Salginatobel Bridge (1930). It is a three-hinged reinforced concrete arch bridge. It is 133 metres long and its main element is a hollow concrete box girder over the central part of the arch. It was constructed to connect Schiers to Schuders.

Although the criticisms regarding the complexity of the analysis method adopted in the study of this structure, the result was a great saving both in terms of material and cost.



Figure 3.8 Salginatobel Bridge, Schiers, Maillart 1930

The technique adopted for the construction of the Salginatobel Bridge was used also for other of his works.

Another important bridge built by Maillart is Schwandbach Bridge (1933). It is a reinforced concrete bridge near Bern. It has a main span of 37 meters. The arch is only 200 mm thick. It supports the bridge deck via 160 mm thick reinforced concrete cross walls.



Figure 3.9 Schwandbach Bridge, Schwarzenburg, Maillart 1933

This type of bridge was imported in Italy by two scientists: Ceradini and Galli. The celebration of the "Maillart type" bridge takes place in Italy with the construction of six bridges with a thin vault and a rigid deck on the Naples-Pompei-Salerno highway.

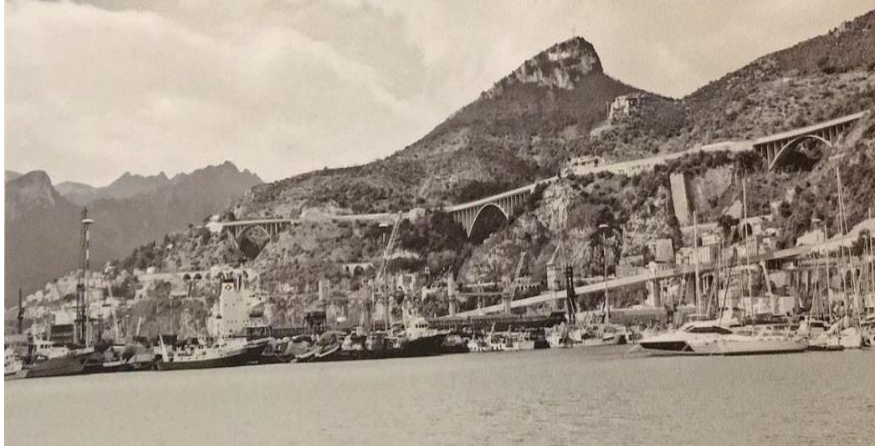


Figure 3.10 Napoli-Pompei highway (Iori 2015)

3.2 GEOMETRICAL DESCRIPTION OF CANNARA BRIDGE

The bridge of Cannara is situated in Perugia located in the centre of Italy. This is a seismic area where often there are earthquakes. It is a reinforced concrete arch bridge cast in situ. It is located near the historical center of Cannara along the provincial road 410. It crosses the river Topino.



Figure 3.11 Perspective view of the Cannara bridge

The supporting structure consists of a reinforced concrete arch of a variable thickness fully restrained to the supports. It is a single span of 39,2 meters long. It is 7,60 meters wide and it has two lanes one for each direction. The arch has an average thickness of 1 meter and its arrow is 8,70 meters. The arch supports a reinforced concrete slab of 40 cm thick with six vertical septa. It is the roadway and these septa have the same width of the arch.

The original project documentation is not available, we have only the one related to the modification of the intersection of Cannara side: there was a local enlargement of the carriageway in 1983.

3.3 HISTORICAL BACKGROUND

The first informations about the bridge of Cannara are relative to the XIII century. In this period a wooden drawbridge probably on stone piers was built. In sixteenth century the bridge on the river Topino started to show its problems: it needed a large number of repairs very expensive. Furthermore, it no longer satisfied the needs for which it had been realized so it was necessary to replace it.

The people who lived in Cannara started to ask authorization to Cardinal Ludovisi to realize the new bridge. The idea was to built a stone bridge. The preventive expense for its realization was 1400 scudi.

The bridge designer's name is unknown but two manufacturers were: Cantuccio Conti and G. Angelo Magnini. The bridge was built but not completely in stone. The part closest to the door of Santa Maria was made of stone and bricks with two stone towers located in the river. The other part of the bridge was realized of wood. In the church of 'Santa Maria Degli Angeli' it is possible to see a mural showing the view of Cannara with this bridge painted in detail. The bridge realized was called 'stone bridge' but in reality the central was completely made of wood. Over time the wood deteriorated and there were a big number of maintenance operations. In 1678 the bridge was repaired once again.

The original bridge was not located where the current one stands today. It was situated more to the left for who looks with their backs towards Cannara. This is easy to detect because foundations are still visible in the river during lean period.

In 1688 it was decided to ask to an expert the task of estimating the cost necessary to realize a new bridge completely in bricks. This choice was the only solution to definitively solve the problems related to the deterioration of wood. The council discussed the necessity to rebuilt the bridge because its beams were again in poor condition on 21 August 1718. Therefore the works started and they were completed in 1742.

The bridge was completely realized in bricks and stone with two arched spans and a big pier in the center. One part of the pier was circular while the other part had an acute angle shape to offer less resistance to the motion of water in the river. Since 1742 the bridge became the center of the life of all the area. It was crossed several times every day.



Figure 3.12 Bridge of Cannara in 1924

It was destroyed by german in retreat at the end of the Second World War and it was rebuilt by Genio Civile at the end of 1945 in the current configuration. Today I have analyzed the bridge in the same configuration of 1945. It has no pier but only two abutments on the two opposite sides of the banks.

3.4 NON - DESTRUCTIVE EXPERIMENTAL INVESTIGATIONS

Cannara was affected by an earthquake of magnitude 6.5 with its epicenter in Norcia on 30th of October 2016. The intensity was the highest in the last thirty years. The number of damaged structures was higher compared to the earthquake occurred in August of the same year. The earthquake occurred in August caused 299 victims, on the contrary no one died in October.

The bridge of Cannara was closed after the earthquake. It was reopened in an alternating one way after few days but more checks were needed. For this reason non-destructive loading tests were carried out to regain normal use of the bridge.

The tests of static loading and monitoring of the behavior of the road bridge was carried out by Unliab Sperimentazione s.r.l. on 25 January 2018 from 9.30 am to 4.35 pm.

The goal of the tests was to evaluate the current behavior of the bridge in term of displacements and cracks opening.

The instruments of the test were three: a deformometer (Controls 58-C0184/20D), an optical level (Leica LS 15) and a theodolite (Leica MS 60).

The test consisted to apply four different trucks with different weights in different configuration on the bridge and to evaluate the displacements in some fixed points of the bridge. In particular, five loading-unloading cycles were carried out considering six different configurations (DS).

The tables and the pictures below show the details of the load cycles and the position of the trucks on the bridge.

CYCLE	LOADING PHASES
1	DS0 – DS1 – DS0
2	DS0 – DS2/A – DS2/B – DS0
3	DS0 – DS3 – DS0
4	DS0 – DS6 – DS0
5	DS0 – DS5 – DS0

Table 3.1 Definition of cycle load

TRUCKS	
LICENSE PLATE	WEIGHT (Kg)
CX 944JX	25000
CC658RH	25240
ED958KS	25040
BT339HP	25040

Table 3.2 Characteristics of trucks

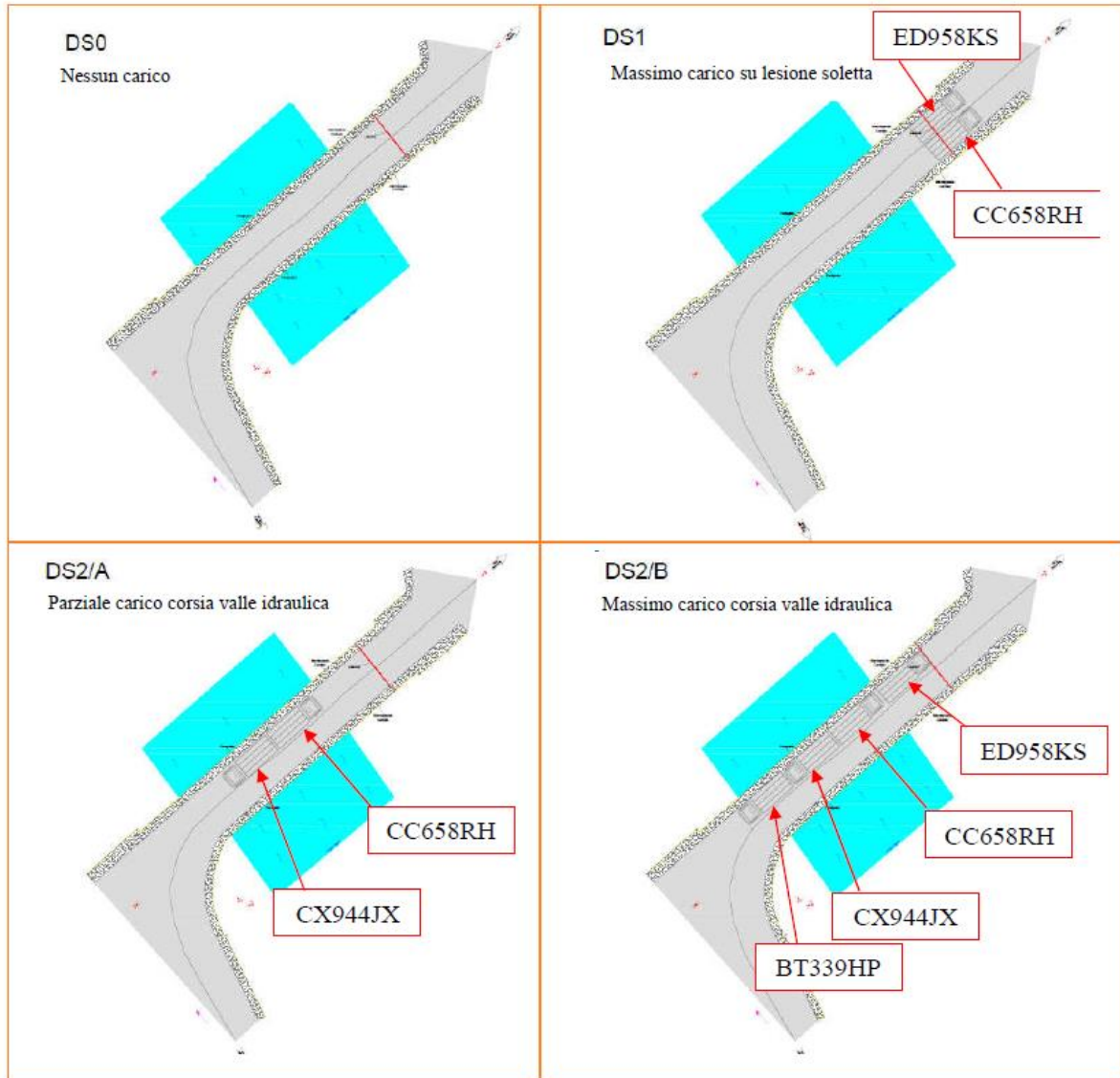


Figure 3.13 Load test configurations



Figure 3.14 Load test configurations

A total station and a digital optical level were used to detect displacements under the load effect. In the picture below there is targets position in front of the bridge (right side). They were levelled by a theodolite LEICA MS60 with precision to the tenth of a millimeter. CS1/SP2 is located about 1.85 meters from the support of the arch of the bridge.

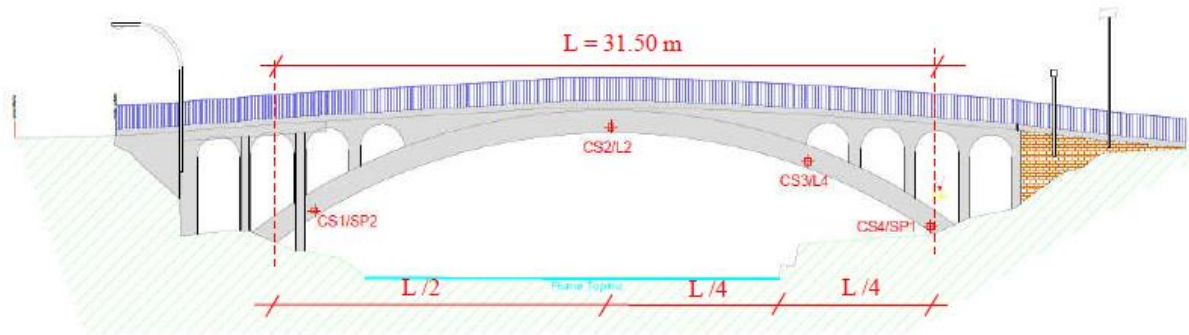


Figure 3.15 Targets positions on right side

Furthermore new benchmarks were placed on the extrados of the bridge to have more precise measurements. They are CAP-1, CAP-2, CAP-3, CAP-4, CAP-1A, CAP-2A, CAP-3A, CAP-4A e CAP-5A. They were leveled using a Leica optical level (mod. LS 15). The accuracy was at hundredth of a millimeter.

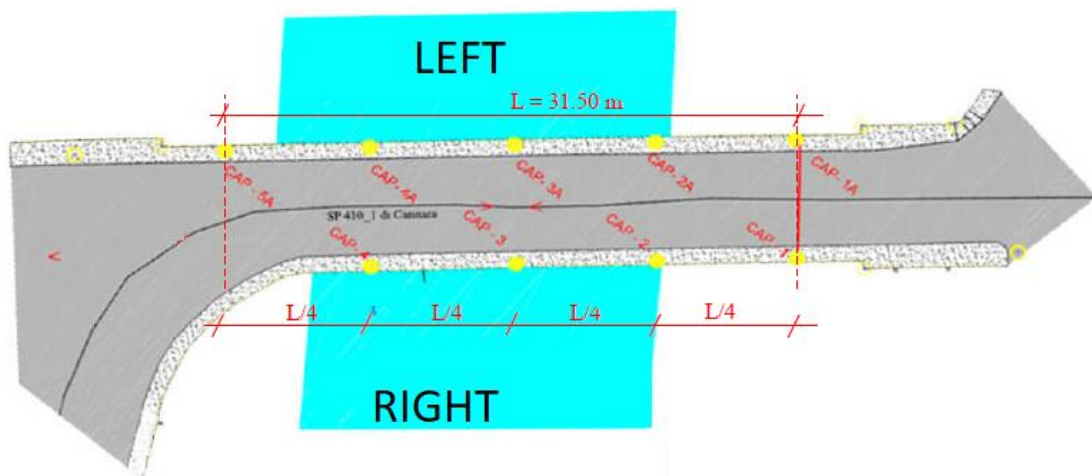


Figure 3.16 Benchmarks positions on extrados

It was also monitored the behavior of the cracks on the bridge during the test. It was used a deformometer (Controls 200 mm). The picture below shows the position of eight deformation bases.

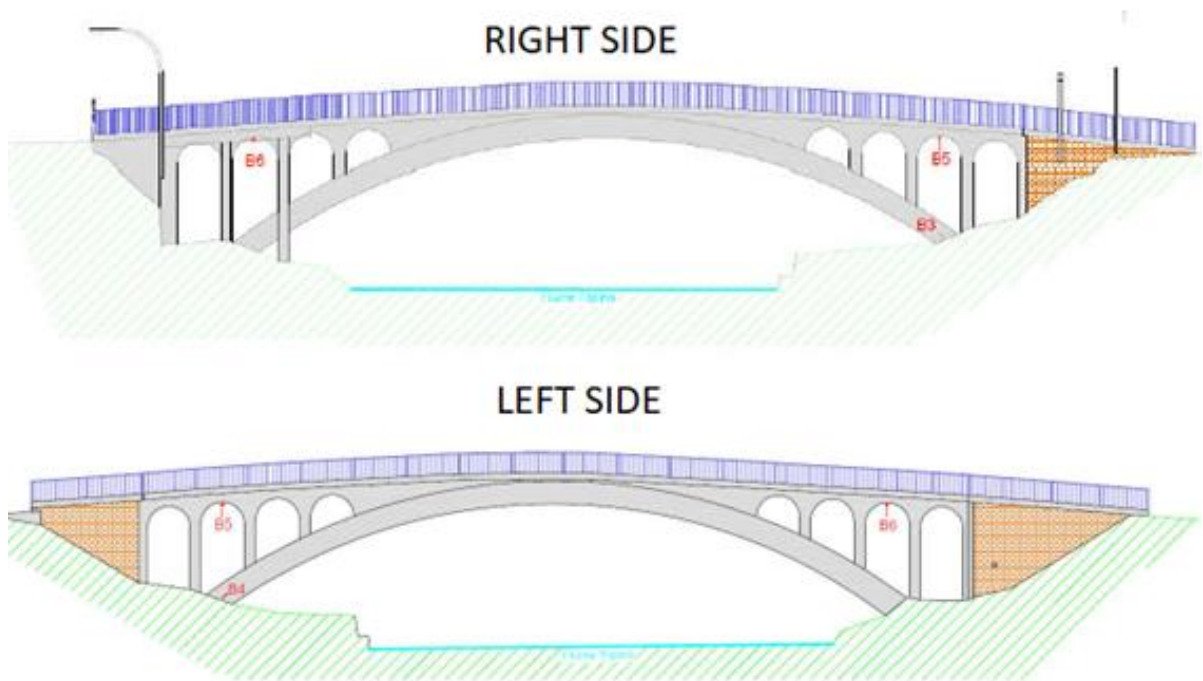


Figure 3.17 Deformometric bases on right side and on left side

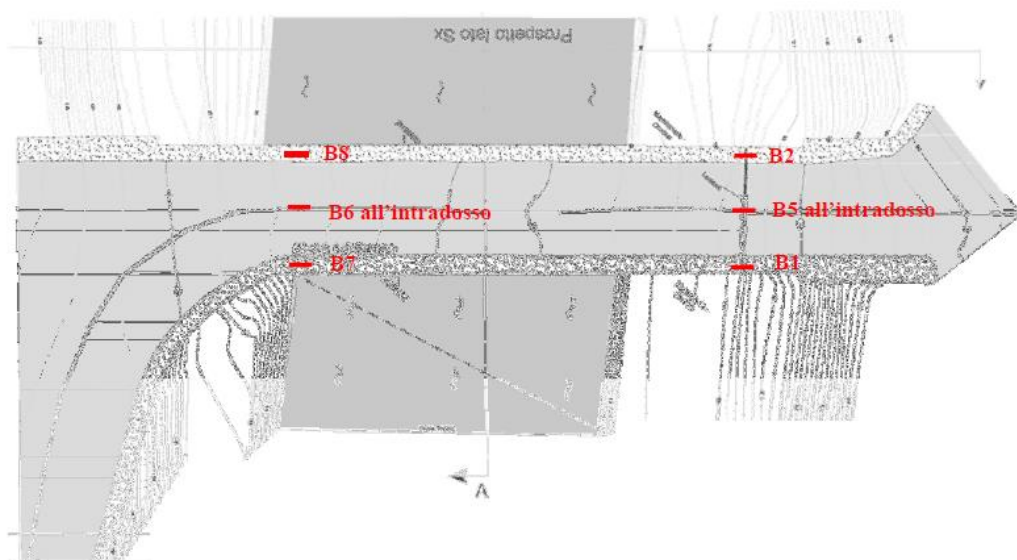


Figure 3.18 Deformometric bases on extrados

Some images relating to the non-destructive activities performed are added below:



Figure 3.19 Images of the static test

It was possible to create three tables to show the results of this test. Every fixed point has moved after each load cycle. Tables show data recorded in different hours during the test. The displacements are indicated in millimeters. If data have a minus sign, it means that the displacement was upwards.

VERTICAL DISPLACEMENT AT INTRADOS							
cycle	load scheme	weight	time	vertical displacement [mm]			
				CS1/SP2	CS2/L2	CS3/L4	CS4/SP1
1	DS0	0	9:30	0.0	0.0	0.0	0.0
1	DS1	50280	10:05	0.2	0.0	0.1	0.3
1	DS1	50280	10:30	0.0	0.0	0.9	0.5
1-2	DS0	0	10:45	0.1	0.0	0.4	0.0
2	DS2/A	50240	10:55	-0.1	0.4	0.2	0.0
2	DS2/A	50240	11:15	0.0	0.2	0.3	0.3
2	DS2/B	100320	11:25	0.0	0.7	0.6	0.0
2	DS2/B	100320	11:40	0.0	0.7	0.7	0.1
2	DS0	0	12:10	0.1	0.4	0.3	0.4
3	DS0	0	12:20	0.1	0.4	0.3	0.4
3	DS3	100320	12:30	0.2	1.3	1.1	0.4
3	DS3	100320	12:45	0.2	1.3	1.1	0.4
3-4	DS0	0	13:25	0.2	0.4	0.5	0.1
4	DS6	100320	13:45	0.2	2.0	1.1	0.3
4	DS6	100320	14:00	0.2	2.0	0.5	0.0
4	DS6	100320	15:00	-0.1	2.0	0.6	0.0
4-5	DS0	0	15:40	-0.2	0.0	0.2	-0.1
5	DS5	100320	16:05	0.5	0.4	-0.4	-0.2
5	DS5	100320	16:20	0.2	0.5	-0.4	-0.3
5	DS0	0	16:35	0.0	-0.1	0.0	-0.1

Table 3.3 Vertical displacements on intrados

It is easy to see that all the displacements of the four targets are elastic. At the end of the loading cycle all the points return to the initial situation. The maximum displacement is the one relative to the CS2/L2 point. It is equal to two millimeters in configuration 4. On the contrary the displacement of CS1/SP2 and CS4/SP1 are always below 0.5 millimeters during all the period of the test.

VERTICAL DISPLACEMENT AT EXTRADOS												
cycle	load scheme	weight	time	vertical displacement [mm]								
				CAP 1	CAP 2	CAP 3	CAP 4	CAP 1A	CAP 2A	CAP 3A	CAP 4A	CAP 4A
1	DS0	0	9:30	0.00	0.00	0.00	0.00	0.00	0.00	0.00	0.00	0.00
1	DS1	50280	10:05	0.27	0.18	0.12	0.14	0.19	0.04	0.01	0.14	0.43
1	DS1	50280	10:30	N.R.*	N.R.*	N.R.*	N.R.*	N.R.*	N.R.*	N.R.*	N.R.*	N.R.*
1-2	DS0	0	10:45	-0.23	-0.21	-0.13	-0.10	-0.15	-0.28	-0.23	-0.11	-0.02
2	DS2/A	50240	10:55	0.02	0.21	0.41	0.17	0.07	0.25	0.72	0.40	0.11
2	DS2/A	50240	11:15	N.R.*	N.R.*	N.R.*	N.R.*	N.R.*	N.R.*	N.R.*	N.R.*	N.R.*
2	DS2/B	100320	11:25	-0.20	-0.04	-0.01	0.03	0.18	0.50	0.57	0.52	0.32
2	DS2/B	100320	11:40	-0.01	0.21	0.19	0.28	0.27	0.62	0.69	0.67	0.23
2	DS0	0	12:10	-0.04	-0.11	-0.40	-0.29	0.08	-0.06	-0.27	-0.12	-0.27
3	DS0	0	12:20	N.R.*	N.R.*	N.R.*	N.R.*	N.R.*	N.R.*	N.R.*	N.R.*	N.R.*
3	DS3	100320	12:30	0.19	0.46	0.29	0.25	0.09	0.24	0.32	0.24	0.01
3	DS3	100320	12:45	0.08	0.36	0.05	0.21	0.13	0.28	0.21	0.26	-0.01
3-4	DS0	0	13:25	-0.22	-0.25	-0.64	-0.23	0.03	-0.07	-0.38	-0.10	-0.13
4	DS6	100320	13:45	-0.38	0.07	0.51	0.12	-0.07	0.31	0.86	0.25	-0.17
4	DS6	100320	14:00	-0.07	0.33	0.63	0.26	-0.04	0.34	0.97	0.29	-0.28
4	DS6	100320	15:00	N.R.*	N.R.*	N.R.*	N.R.*	N.R.*	N.R.*	N.R.*	N.R.*	N.R.*
4-5	DS0	0	15:40	-0.19	-0.21	-0.68	-0.48	-0.01	-0.17	-0.19	-0.21	-0.05
5	DS5	100320	16:05	-0.28	-1.23	-0.25	0.82	-0.14	-1.16	0.11	1.43	-2.10
5	DS5	100320	16:20	N.R.*	N.R.*	N.R.*	N.R.*	N.R.*	N.R.*	N.R.*	N.R.*	N.R.*
5	DS0	0	16:35	-0.16	-0.31	-0.72	-0.38	-0.05	-0.19	-0.31	-0.31	-0.45

*N.R. : non rilevato.

Table 3.4 Vertical displacements on extrados

This table shows how all the displacements of the benchmarks located in extrados of the bridge remained below 1 millimeter during all the test. The maximum displacement occurred during the fifth load cycle. The maximum value was -2.10 millimeter relative to CAP5A. It is upwards. CAP2, CAP2A and CAP4A moved a little bit more than one millimeter during the fifth load cycle too. At the end of the test it is possible to see that all the benchmarks moved upwards around 0.3 millimeters on average.

DEFORMOMETRIC VARIATIONS											
cycle	load scheme	weight	time	deformometric bases [mm]							
				B1	B2	B3	B4	B5	B6	B7	B8
1	DS0	0	9:30	0.000	0.000	0.000	0.000	0.000	0.000	0.000	0.000
1	DS1	50280	10:05	-0.120	-0.017	-0.013	-0.026	-0.075	-0.003	-0.006	0.002
1	DS1	50280	10:30	-0.120	-0.017	-0.013	-0.026	-0.075	-0.004	-0.008	0.002
1-2	DS0	0	10:45	-0.002	-0.002	-0.020	-0.005	-0.012	-0.002	-0.001	0.000
2	DS2/A	50240	10:55	-0.125	-0.105	-0.048	-0.084	-0.084	0.004	-0.081	0.002
2	DS2/A	50240	11:15	-0.125	-0.105	-0.048	-0.084	-0.084	0.004	-0.081	0.002
2	DS2/B	100320	11:25	-0.167	-0.108	-0.096	-0.096	-0.080	-0.047	-0.055	-0.018
2	DS2/B	100320	11:40	-0.169	-0.102	-0.108	-0.098	-0.078	-0.047	-0.083	-0.002
2	DS0	0	12:10	-0.220	-0.157	-0.120	-0.074	-0.122	-0.075	-0.254	-0.111
3	DS0	0	12:20	-0.220	-0.157	-0.120	-0.074	-0.122	-0.075	-0.254	-0.111
3	DS3	100320	12:30	-0.207	-0.183	-0.174	-0.109	0.055	-0.096	-0.262	-0.122
3	DS3	100320	12:45	-0.202	-0.176	-0.170	-0.102	-0.131	-0.089	-0.254	-0.120
3-4	DS0	0	13:25	-0.290	-0.231	-0.144	-0.094	-0.173	-0.113	-0.335	-0.191
4	DS6	100320	13:45	-0.268	-0.221	-0.183	-0.135	-0.159	-0.058	-0.263	-0.039
4	DS6	100320	14:00	-0.281	-0.233	-0.197	-0.140	-0.158	-0.057	-0.280	-0.044
4	DS6	100320	15:00	-0.278	-0.230	-0.183	-0.126	-0.169	-0.051	-0.292	-0.039
4-5	DS0	0	15:40	-0.286	-0.229	-0.132	-0.089	-0.170	-0.100	-0.361	-0.194
5	DS5	100320	16:05	-0.809	-0.781	-0.193	-0.149	-0.633	0.115	0.251	0.083
5	DS5	100320	16:20	-0.819	-0.794	-0.192	-0.148	-0.640	0.120	0.278	0.093
5	DS0	0	16:35	-0.295	-0.246	-0.112	-0.076	-0.194	-0.082	-0.321	-0.168

Table 3.5 Deformometric variations

The last table shows the opening of the cracks. During the test most of the cracks shrink up to 0.9 millimeters. At the end of the load cycle the deflectometer located in position B5 measures a closure of 0.194 millimeters.

It is interesting to understand better the real kind of the displacements of the bridge to see the deformation line after the test. The picture below shows a comparison between the initial line of the arch and that after the load cycle. The displacements can be considered completely elastic.

At the end of the test it was decided to reopen simultaneously the two traffic lanes of the bridge.

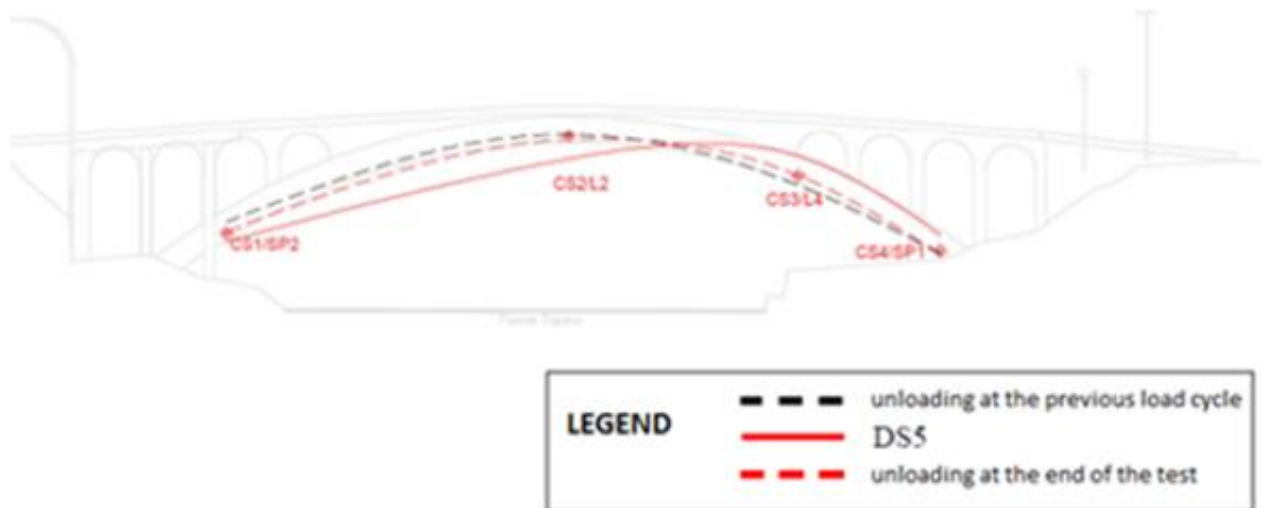


Figure 3.20 Longitudinal deformation after the fifth cycle

3.5 GEOGNOSTICS INVESTIGATIONS

Geognostics uses special activities such as geognostic surveys, on-site tests, static and dynamic penetrometric tests, seismic and geo-electric geophysical surveys, laboratory tests, in order to determine the characteristics of the soil.

The emergency on old structures rose after the earthquake in 2016. Money was allocated to focus the attention on some structures including the bridge of Cannara. The tests should have been the first step for structural operations that haven't happened yet.

The continuous drilling in the area of the bridge of Cannara was carried out on the 16th February 2018. It allowed a stratigraphic reconstruction detailed and punctual of the lithotypes present in the subsoil. The surveys were performed at two different points in the area.

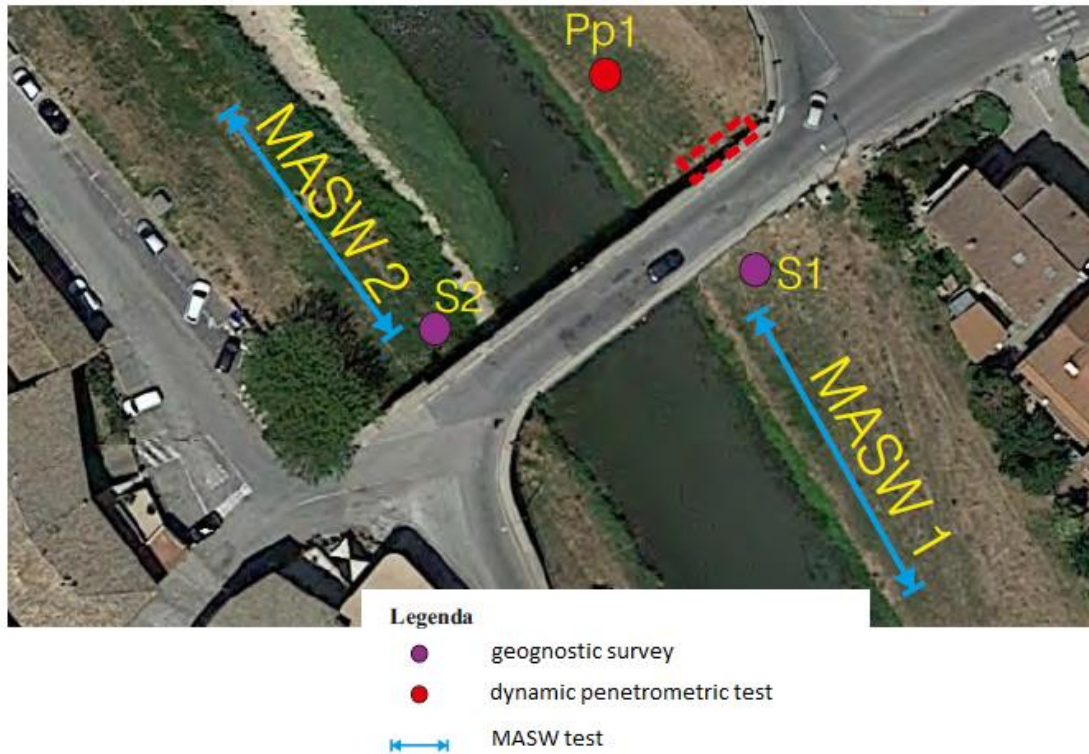


Figure 3.21 Tests location in the Cannara Bridge area

One on the left bank and the other on the right one. They were carried out with the drill CMV 600 MK. The carrots, extracted by special rotation systems, are placed in "cataloging boxes" which serve to preserve the material for a long time. They are useful to read and then to draw up, in a detailed manner, the stratigraphy of the subsoil. The images below describe the test relative to S1.



Figure 3.22 Cataloging boxe relative to specimen S1

In both the two surveys (S1 and S2) the subsoil was investigated up to a depth of 21 meters. The table below shows the lithological description of the subsoil.

S1			S2		
Partial depth	Prog. depth	Lithological description	Partial depth	Prog. depth	Lithological description
1.20	1.20	Vegetable soil	1.00	1.00	Vegetable soil
4.80	6.00	Thickened gravel in sandy matrix with cemented levels	1.00	2.00	Little thickened sand with anthropic material
2.50	8.50	Very melted sand	1.00	3.00	Very melted sand
0.90	9.40	Clay sand melted with gravel	3.00	6.00	Gravel thickened into sandy matrix with anthropic material up to 5.10 meters
0.40	9.80	Silty clay	2.50	8.50	Very melted sand
0.80	10.60	Sandy gravel in a silty clayey matrix	1.10	9.60	Slightly gravelly sand of grey color
0.40	11.00	Gravel in sandy matrix	2.40	12.00	Clay sand
2.00	13.00	Melted clay sand	1.00	13.00	Clay sand with gravel
3.00	16.00	Clay sand very melted with gravel	3.00	16.00	From silty clay to very melted clay sand
3.70	19.70	Clay silt weakly sand	4.50	20.50	Silty clay and sandy clay
1.30	21.00	Clay sand with gravel that increases with depth	0.50	21.00	Clay sand with gravel

Table 3.6 Stratigraphic analysis of S1 and S2 specimen

From the observation of the stratigraphic survey of the sample S1 is possible to see that there is a first layer of vegetable soil (up to 1.20 meters from campaign level). Furthermore, there is a layer with thickened gravel in sandy matrix with cemented levels (up to 6.0 meters from campaign level) above a layer of 2.50 meters characterized by highly compressible sandy soils. Conversely, it can be observed that the soil of sample 2 was “improved” in mechanical resistance using anthropic material under the same thickness of vegetable soil. Therefore the conditions of the sample S2 are considerably better compared to S1 sample. This can be explained because in the past the engineers tried to improve the conditions of the soil where the structures

were built. It was often created a lean concrete layer where the foundations were placed.

A granulometric analysis was carried out on two different samples both for specimen S1 and for specimen S2. Respectively the granulometric analysis of the specimen S1 relates to the soil between 10 meters and 10.6 meters; the other sample relates the soil between 17.40 meters and 18.0 meters. For the specimen S2 the two samples analyzed are related to the soil between 9.00 meters and 9.60 meters and 13.00-13.60 meters.

Ghiaia	67,3 %	Passante setaccio 10 (2 mm)	27,7 %	D10	---	mm
Sabbia	19,1 %	Passante setaccio 40 (0.42 mm)	21,0 %	D30	2,98210	mm
Limo-Argilla	13,6 %	Passante setaccio 200 (0.075 mm)	13,6 %	D50	10,08150	mm
				D60	13,32194	mm
				D90	21,87551	mm
Coefficiente di uniformità		---		Coefficiente di curvatura		---

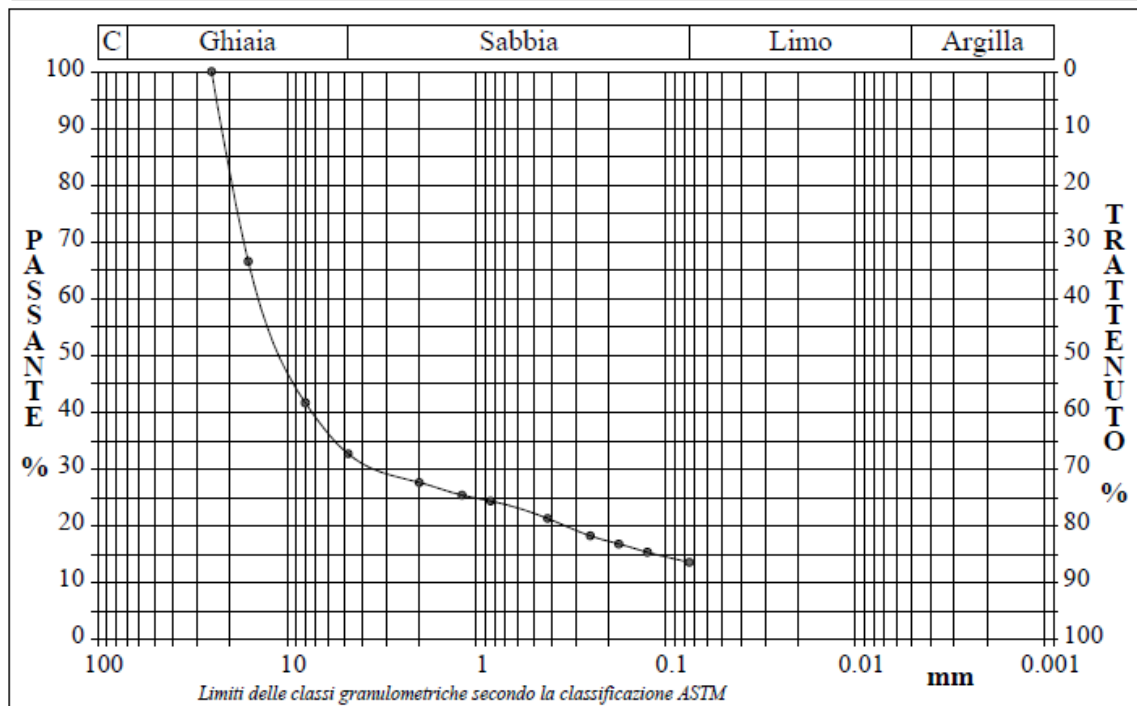


Figure 3.23 Granulometric curve relative to specimen S1 (10-10.60 meters depth)

Ghiaia	17,1 %	Passante setaccio 10 (2 mm)	75,9 %	D10	---	mm
Sabbia	66,5 %	Passante setaccio 40 (0.42 mm)	45,3 %	D30	0,22997	mm
Limo-Argilla	16,4 %	Passante setaccio 200 (0.075 mm)	16,4 %	D50	0,47968	mm
Coefficiente di uniformità		---	Coefficiente di curvatura		---	
				D60	0,71461	mm
				D90	6,42706	mm

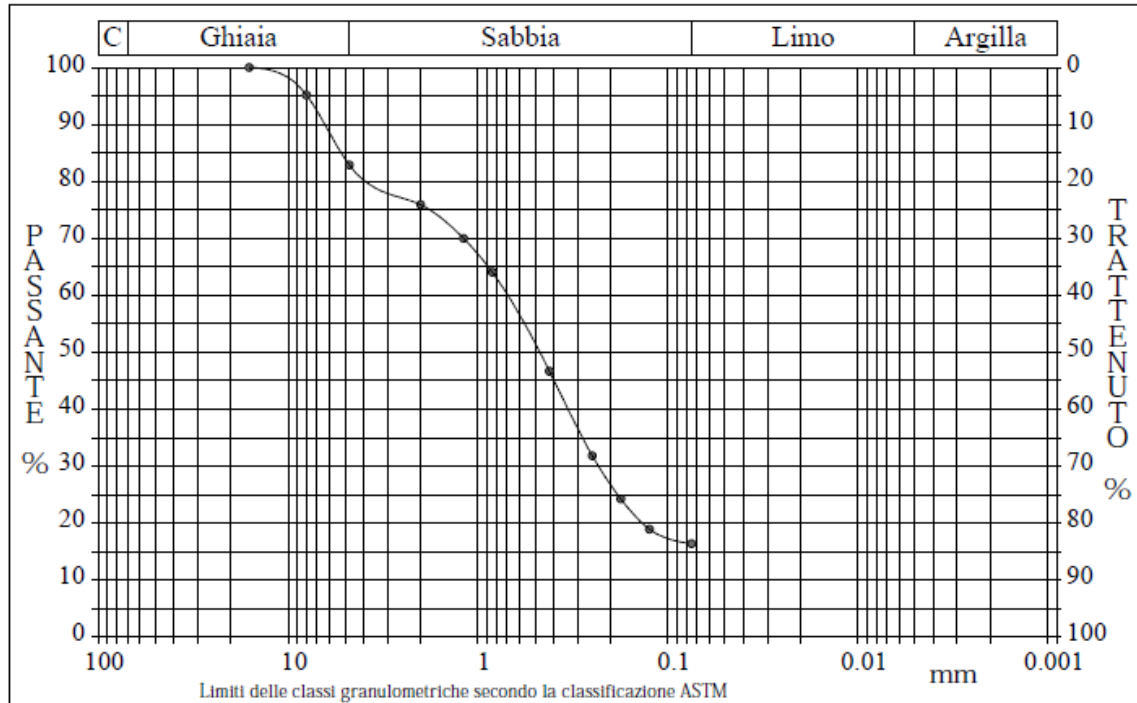


Figure 3.24 Granulometric curve relative to specimen S2 (9.0-9.60 meters depth)

3.5.1 DIRECT SHEAR TEST

A direct shear test is carried out on 26 of February 2018. The goal of the test was to determine the characteristics of resistance to cut of soil. The specimens were 4: two of them belonged to S1 and the others to S2. For each of them were realized 3 sub-specimens and they were subjected to different pressures: 100 KPa, 200 KPa and 300 KPa.

The test can be divided in two different phases: the consolidation phase and the cutting test. In the first phase a vertical constant force is applied for 24 hours. The reduction of the sub-specimens and the quantity of water lost are measured. In the second phase an horizontal displacement is applied to the sub-specimens with a constant and very low speed. The values of the horizontal force which counteract the imposed displacement and the reduction of height are obtained. The test will stop

when the peak resistance is reached. The table below shows the shear strength resistance: c and f (cohesion and friction angle).

S1				S2			
10-10.60 meters		17.4-18.0 meters		9.0-9.6 meters		13.0-13.6 meters	
c	f	c	f	c	F	c	f
0 kPa	41.7°	9.0 kPa	27.7°	0 kPa	38.1°	2 kPa	24.1°

Table 3.7 Cohesion and friction angle relative to S1 and S2 specimen

The investigation of silty and clayey soils was completed with edometric test and calculation of the liquidity and plasticity limit.

3.5.2 DYNAMIC PENETROMETRIC TEST

Another interesting test carried out in the area of the bridge was the dynamic penetrometric test. This test is widespread and used by geologists and geotechnics for their simplicity of execution, speed of execution and costs.

Their elaboration, interpretation and graphic visualization allows to define the soil crossed with a continuous image, which also allows a correlation with geognostic surveys for the stratigraphic characterization.

The penetrometric test also allows to recognize the thickness of the coulters on the substrate, the altitude of any pitched and the general consistence of the soil.

A probe Pagani 73-100 SCPT was used during the activity. The test consisted in measuring the resistance to penetration of a metal conical tip connected to an extendable steel pole up to 18.6 meters. The test information was continuous. The number of strokes necessary for the penetration of the tip in an established length was counted. The table below shows the characteristics of the probe.

Swing weight	72.5 kg
Free fall height	0.75 meters
Weight system	6 kg
Conical tip diameter	50.46 mm
Base tip	20 cm ²
Length of the rods	1 m
Weight of rods per meter	7 kg/m
Joint depth first rod	0.80 meters
Tip advance	0.30 meters
Coeff. correlation	1.15
Coating	No
Tip opening angle	60°

Table 3.8 Characteristics of PAGANI 73-100 SCPT probe

The characteristics of the equipment and the methods of execution have been standardized in the international Reference Procedures developed by the ISSMFE which define four kind of penetrometers based on the mass of the hammer:

TIPO	SIGLA DI RIFERIMENTO	MASSA BATTENTE (Kg)
Leggero	DPL (light)	M ≤ 10
Medio	DPM (medium)	10 < M < 40
Pesante	DPH (heavy)	40 < M < 60
Super pesante	DPSH (super heavy)	M ≥ 60

Table 3.9 ISSMFE technical standards

If we consider the characteristics shown by the probe used in our test we can talk about dynamic super heavy. At the end of the test it is possible to determine the dynamic resistance of the tip R_{pd} by the formula below. This value is a function of the number of hits useful to produce a certain reduction:

$$R_{pd} = \frac{M^2 \cdot H}{[A \cdot e \cdot (M + P)]} = \frac{M^2 \cdot H \cdot N}{[A \cdot \delta \cdot (M + P)]}$$

where M is the hammer weight, P is the total weight of rods and abutment system and $e=d/N$ is the average infixion per stroke. The image below shows the results:

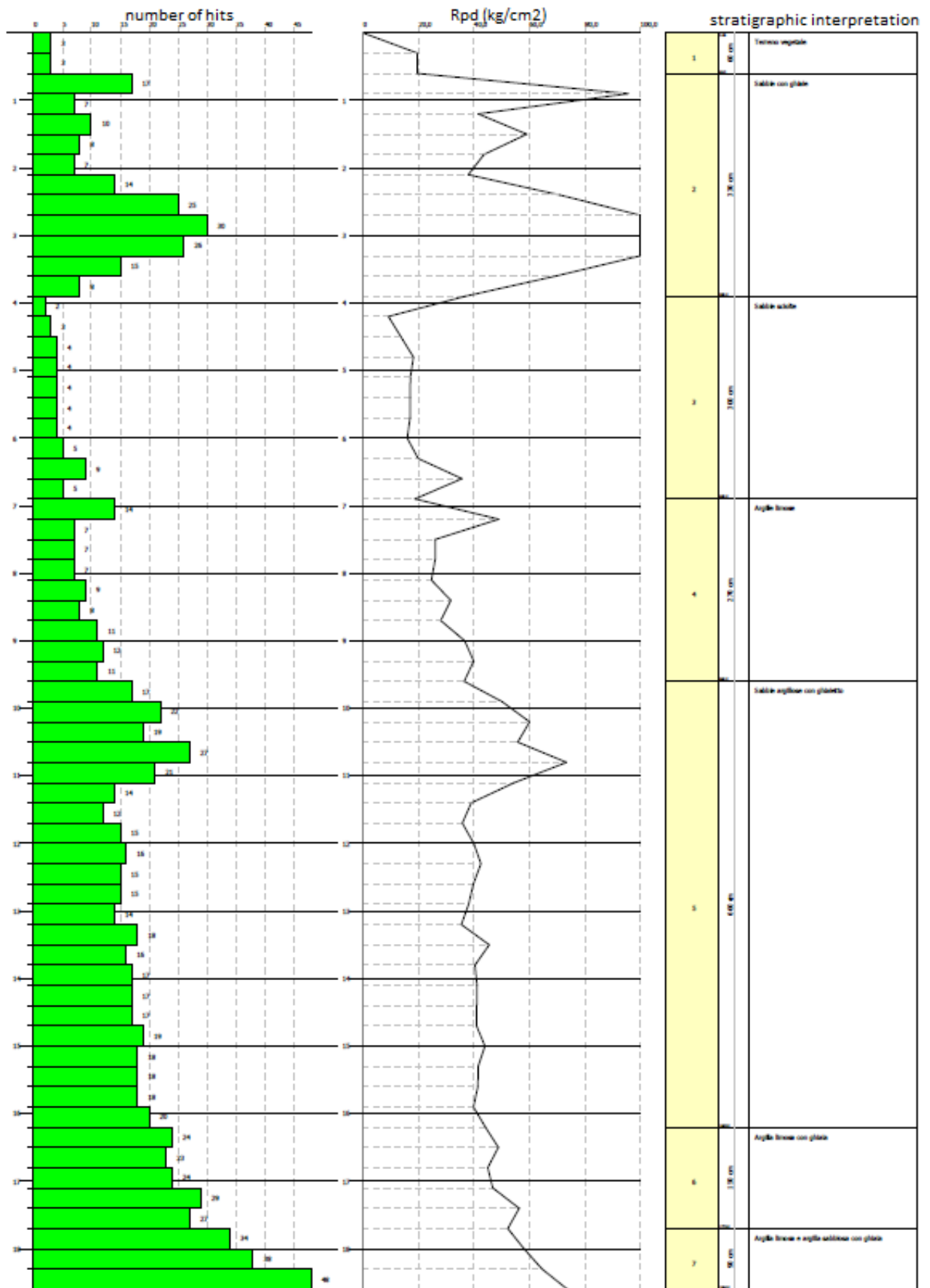


Figure 3.25 Dynamic Penetrometric Test

A further confirmation related to the better conditions of soil of sample S2 compared to soil conditions of sample S1 comes from this dynamic penetrometric test. It is possible to see that there is a reduction in mechanical resistance of soil under 3 meters depth from campaign level. The number of shots needed to penetrate the soil decreases rapidly. Probably another penetrometric test on the other side of the bridge would be useful to confirm this situation.

3.5.3 MASW TEST

According to the 2003 regulation, all Italian municipalities were classified into 4 categories related to their seismic risk, calculated according to the PGA (Peak Ground Acceleration, or the peak of acceleration to the ground), frequency and intensity of earthquakes. The classification is constantly updated. Cannara belongs to zone 2: "Area where strong earthquakes can occur". For this reason it was necessary to carry out test for the seismic characterization of the soil.

<i>Zona sismica</i>	<i>Descrizione</i>	<i>accelerazione con probabilità di superamento del 10% in 50 anni [a_g]</i>	<i>accelerazione orizzontale massima convenzionale (Norme Tecniche) [a_g]</i>	<i>numero comuni con territori ricadenti nella zona (*)</i>
1	Indica la zona più pericolosa, dove possono verificarsi fortissimi terremoti.	$a_g > 0,25 \text{ g}$	0,35 g	703
2	Zona dove possono verificarsi forti terremoti.	$0,15 < a_g \leq 0,25 \text{ g}$	0,25 g	2.225
3	Zona che può essere soggetta a forti terremoti ma rari.	$0,05 < a_g \leq 0,15 \text{ g}$	0,15 g	2.810
4	E' la zona meno pericolosa, dove i terremoti sono rari ed è facoltà delle Regioni prescrivere l'obbligo della progettazione antisismica.	$a_g \leq 0,05 \text{ g}$	0,05 g	2.186

Table 3.10 Seismic classification of Italy based on PGA

In the area were carried out 2 Multi-channel Analysis of Surface Waves (MASW). The MASW investigations were performed by producing 2 geophone extensions of 12 channels for a total distance of 48.0 linear meters with an intergeophonic interval equal to 4.0 meters.

Data acquisition was performed using the 24-channel 16SG24 Seismograph of the P.A.S.I. LTD of Turin and the processing took place through the WinMASW software from Eliosft.

MASWs are carried out by Rayleigh wave analysis which are recorded using common vertical geophones (those used for the common refraction in compression waves) and considering a common vertical impact source obtained by a hammer.

The test provides the stratigraphy and speed of shear waves. Once the thicknesses of the layers and the relative speed of the S waves have been acquired, the average speed relative to the first thirty meters of underground is calculated. Using the formula below we can classify the site according to the normative references:

$$V_{S30} = \frac{30}{\sum_{i=1, N} h_i / V_i}$$

where h_i is the thickness and V_i is the speed of shear waves of each layer. If there is a heterogeneous soil, the surface waves do not have a single speed, but different speed at the different frequencies. This phenomenon depends on seismic properties of the subsoil; it is known as the geometric dispersion and the relationship that link the frequency at the phase speed is called the dispersion curve. The widest wavelengths (the lowest frequencies) are influenced by the deepest part of the subsoil, while the small wavelengths (the highest frequencies) depend on the characteristics of the superficial part.

The table below shows the results of the test.

	MASW 1		MASW2	
	Vs (m/s)	Thickness (m)	Vs (m/s)	Thickness (m)
LAYER 1	246	1.3	230	4.3
LAYER 2	315	1.1	223	4.4
LAYER 3	199	10.9	267	7.0
LAYER 4	347	2.1	329	4.6
LAYER 5	407	13	432	9.8
Vs ₃₀ (m/s)	284		297	

Table 3.11 MASW test results

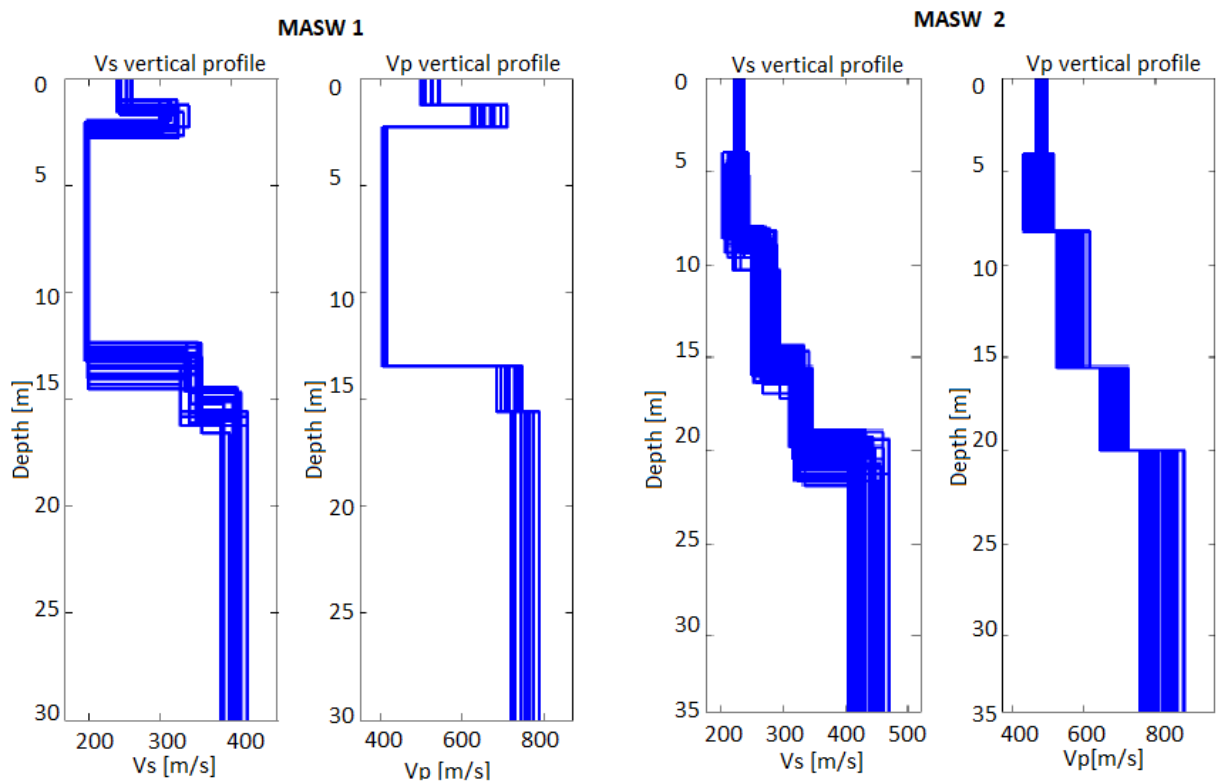


Figure 3.26 Speed of waves propagation with soil depth

The subsoil category related to these two Vs₃₀ speeds is:

C- Deposits of coarse-grained medium-thickened soils or fine-grained soils, characterized by gradual improvement of the mechanical properties with the depth and values of the Vs₃₀ is between 180 m / s and 360 m / s (15 <NSPT30 <50 in coarse-grained soils and 70 <cu30 <250 kPa in fine-grained soils).

It is possible to reach the same conclusions of dynamic penetrometric test and stratigraphic test observing the results of MASW investigations carried out on both

sides of the bridge. The speeds (V_s) rise progressively with increasing depth in MASW 2, while in MASW 1 the speeds suffer an abrupt decrease after the first layer of the soil. This is due to the presence of a strongly melted soil therefore it can be compressible under the effects of an earthquake.



Figure 3.27 MASW test

3.6 TOPOGRAPHIC SURVEY

As mentioned above there is no documentation relating to the design of the bridge. Therefore it was necessary to carry out topographic surveys to proceed in my analysis. The goal was to obtain a 3D model in a short time, which allowed us to extract geometric and morphological information related to the Cannara bridge.

The activities were carried out by a company called Eagle Projects on 29th July 2019. Laser scanner technology has been used. It allows to digitally acquire the correct position and the shape of the objects through a cloud of points. The laser strikes the surface of the object to be detected according to the angle based on its position, so for a complete description of the object several scans are necessary. The position of each point is identified according to a system of coordinates x , y , z centered on the position of the laser scanner. Each point is also detected by 4 other parameters: the

reflectance index of the struck material and the RGB parameters (red, green, blue) related to the color.

The tools used for the topographic survey of the area of Cannara bridge are two laser and a drone:

- Leica BLK 360
- FARO FOCUS 3D
- A drone DJI SPARK



Figure 3.28 Equipment of topographic survey

The first step of the activity was to decide the position of the 23 markers. It is a crucial moment because at least 3 markers must be present in each scan. They were placed in a checkerboard pattern above and below the bridge and on both banks. The markers have also been positioned in the arches even if they were not recorded during the acquisitions.

The laser LEICA BLK 360 is less powerful than the laser FARO FOCUS 3D because it acquires a smaller number of points at the same time. It weighs 1 kg and it needs less than 3 minutes to realize a complete circular scan. It acquires 360.000 points per second rotating on itself. It was placed under the arches and on the two embankments. We obtained 11 scans from Leica BLK 360. It acquires points up to 60

meters while the laser FARO FOCUS 3D arrives also to acquire points up to 160 meters. It was positioned on the street level of the bridge. It is not powerful in the photos, for this reason it was used only LEICA BLK 360 to take pictures. FARO FOCUS 3D was used to realized 15 scans. At the end we had 26 scans obtained by the two lasers. Each scan consists of a big number of points which we can call “points cloud”. We matched the different scans considering the common markers using Leica Cyclone software.

At the beginning we imported all the 26 scans in Cyclone, then we decided the position of the markers and we started to match different scans which had markers in common. This activity was carried out by hand but it can also be performed by software with a lower final precision. At the end of each connection Leica Cyclone gives me information if there is an error bigger than a centimeter and an half.

The scans failed to detect the two highest arches so it was necessary to integrate the 26 scans with the photos provided by the DJI SPARK drone. Three different flight plans were set but also pictures by hand were taken.

The photos taken by the drone were of two different types:

- zenith photos: the drone is positioned parallel to the road. In this position the facades are not detected;
- photos with a 45° inclined drone to detect the facades.



Figure 3.29 Flight plan for a height of 50 meters

An automatic flight plane was carried out to capture the photos. The 3D model realized combining only laser pictures was reconstructed with new informations. At the end of the elaboration of the data the precision obtained using markers is 8 millimeters, on the contrary if we had not used the markers we would have had a clearly lower precision equal to 3 centimeters. The table and the pictures below show the flight plans realized with the drone.

Flight description	Number of photos
Flight 50 meters high	87
Flight 20 meters high on a larger area than the previous one	230
Perimeter flight at 45° inclination and 15 meters high	65
Handmade photos	80

Table 3.12 Flight plans



Figure 3.30 Drone pictures

The pictures below show the “point cloud” after combining the 3D model realized with scans obtained from laser and drone pictures. Scans are black and white pictures. The drone pictures have almost completely confirmed the laser scans. This means that the overlap of the scans was correct.



Figure 3.31 Point cloud of the Cannara Bridge area

The photos taken by the Leica BLK 360 and the drone were used once the point cloud of the Cannara area was completed. These were projected on the cloud to provide the RGB information. A color is associated to each point of the cloud. The pictures below show the overlapping of points and color.



Figure 3.32 Superposition of point cloud with RGB information

At the end we imported the 3D model of the bridge of Cannara in ReCap software to carry out the necessary measurements for the following analysis and the construction of the FEM model.

The availability of laser scanner technology compared to the traditional one for topographic surveys has numerous advantages. First of all, the realization time are reduced. In a traditional topographic survey using a total station, it can be measured only one point at a time. Furthermore, the operator error is canceled because the process is completely automatic. The laser scanner is very compact and not so heavy so it can be used in different situations and palces. The laser scanner 3D allows the acquisition of geometric data but it is also possible to color the “point cloud” with the RGB real data to identify deteriorations and to schedule maintenance activities. The topographic survey can be imported into CAD software and it is used as a starting

point for 3D drawings. Moreover, in a traditional techniques it is necessary to think before about the result to be obtained instead the analyzes can also be made later with laser scanner.

3.7 INTRODUCTION TO FEM MODEL

The finite element method is a technique of approximation of real problems widely used in the engineering field. We are often unable to obtain an analytical solution for many engineering problems. For example, if we consider the displacements as unknown in an elastic problem. We need a system of equilibrium differential equations. Although each equation of equilibrium is simple, it is impossible to obtain an analytical solution to the problem when the shape is not regular. So it is impossible to reach an exact solution. This is why FEM methods were born. The discretization of the continuous problem is the purpose of this technique. The idea is to divide the starting structure which is very complex in many simpler substructures. This is a great simplification but the amount of data to be processed always remains very high. Therefore the application of automatic calculation procedures are required to overcome the difficulty due to the repetition of a series of mathematical operations.

The steps necessary to discretize a continuous body are:

- Identification of nodes;
- division of a continuous body into a series of elements delimited by nodes (mesh);
- introduction of interpolation techniques to find the solution even in the points inside the elements.

The choice of the geometry of the elements adopted in the mesh and its density influences the quality of the solution obtained. In general, if the mesh is thicker the result of the problem will be more accurate. In the study of a structure from the

engineering point of view, it is necessary to set the boundary conditions, imposing static or dynamic, thermal or mechanical stresses.

The boundary conditions are applied in the nodes both in the case in which they are applied in correspondence of them and in the case in which the stresses act inside the element.

The choice of the type of element adopted depends on the starting geometry of the structure. Obviously the solution obtained depends on the material used and its constitutive bond. There are different constitutive bond.

Therefore, the finite element method presents defects due to the arbitrariness of the choices adopted by the operator; a series of inaccuracies add up depending on the approximations and simplification assumptions which are adopted during the model elaboration. all this makes the reliability of the FEM models variable and it helps us to understand how difficult is to build models able to accurately predict the real behavior of the existing structure.

3.7.1 STRAUS7 R 2.4.6

Straus7 is the famous calculation and design software for finite element model. It is used in thousands of installations all over the world and it is also adopted in Italy in major design studios, construction companies, public bodies and universities. The program is completely integrated into Windows, with constantly evolving functions. It allows copy-paste and exchange operations with other applications. Users are facilitated by the presence of a detailed manual on all aspects of its operation and by levels of excellence in training and support. Tools such as copy, extrude, scale, move and mirror are available; it is possible to introduce nodes and elements and to operate automatic subdivision of elements with maintenance of the boundary conditions. The program is also suitable for thickening two and three - dimensional models and to automatically generate two-dimensional meshes with mainly high-quality quadrangular elements. It is useful for checking the accuracy of finite element models and it is also possible to graphically determine nodal discontinuities of the model.

Straus7 can perform all types of analysis: linear and non-linear static, linear and non-linear dynamics required by seismic regulation coming up to the definition of viscous dampers properties used in seismic isolation in the non-linear field.

3.7.2 FEM MODEL OF THE CANNARA BRIDGE

It should be underline that in this preliminary study phase it was not necessary to refine and weigh down the model. It carried out based on the information available and so it presents various approximations related to:

- simplification of the geometry of the elements;
- choice of the constraint conditions of the structure;
- simplifications regarding the mechanical properties of materials.

In this phase the aim to be pursued is to obtain general indications regarding the position of the sensors based on the results obtained from the modal analysis in terms of modal forms.

FEM model is realized using 1502 nodes. In particular the beam element is chosen for the representation of one-dimensional elements and the shell element is chosen for the two-dimensional elements.

BEAM: it is a one-dimensional element with two nodes (i, j); the third node k is able to give the orientation. It is based on Timoshenko's theory of beams and it considers shear deformability. Each node of the element can have six or seven degrees of freedom, the seventh is warping (optional). It supports elastic, plastic, creep and non-linear models.

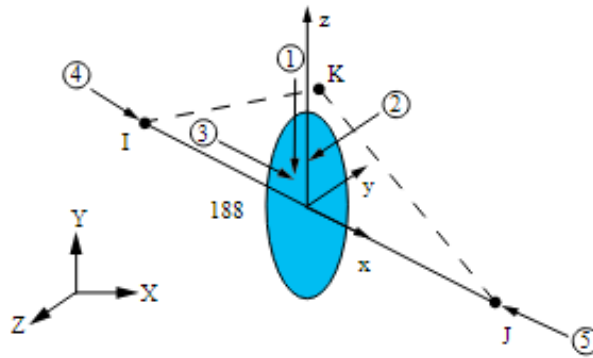


Figure 3.33 Beam element

SHELL: it is an eight-node element with six degrees of freedom for each node. It is suitable for both linear and non-linear analyzes. It is formulated according to Reissner-Mindlin's theory and it can be used for the analysis of structures that vary between being slim to moderately thick

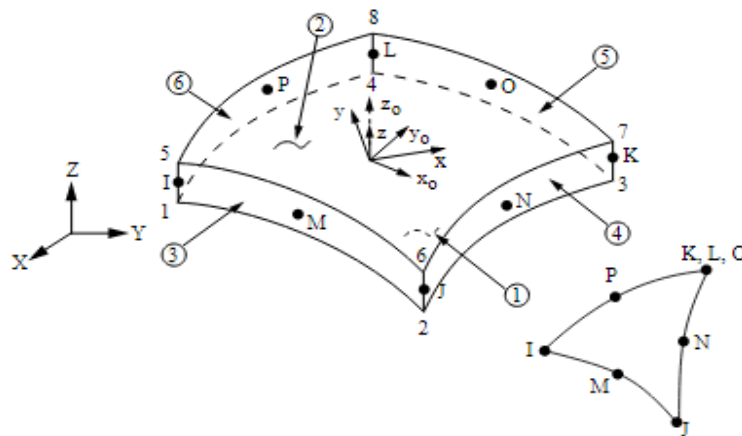


Figure 3.34 Shell element

In the model there are 104 beam elements and 1600 shell elements. The beam element is adopted for the representation of the curb and all the other elements are realized using shell elements.

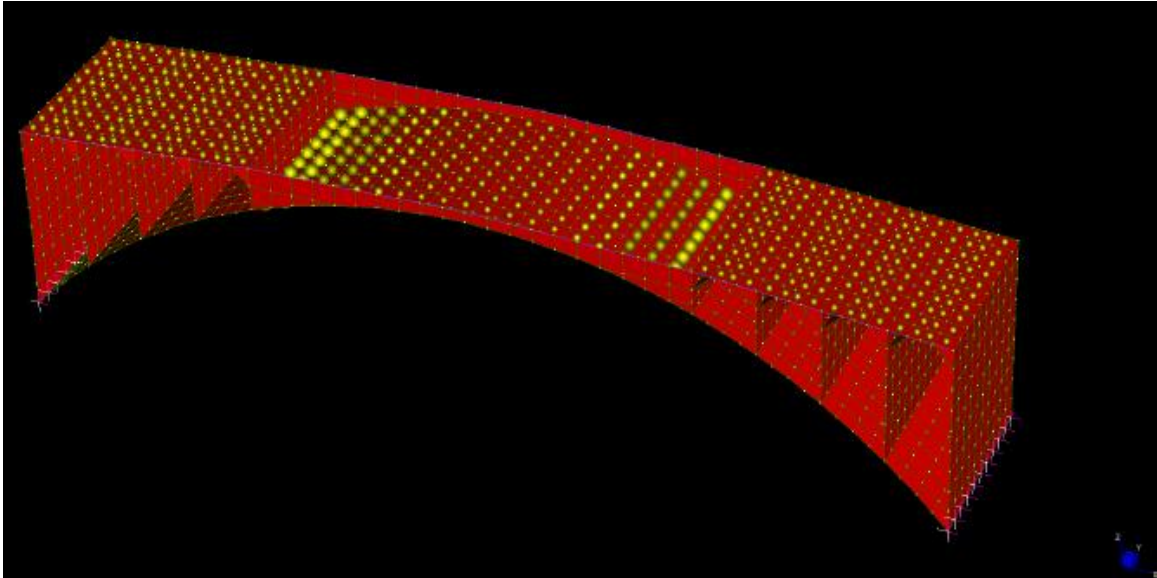


Figure 3.35 FEM model of the Cannara Bridge

FEM model presents the yielding of the abutment, on the opposite side to the center of Cannara, calculated by the professor Materazzi and the professor Balli. The values calculated by the professor Materazzi have been approximated to 1 cm in z direction and 0.8 cm in x direction.

Only the crack of the third arch on the side opposite to the historic center of Cannara is represented into the FEM model. The plastic hinge on the main arch and the other cracks are simulated reducing by 50% the initial stiffness of the concrete in the model.

I report below the simplifications adopted in the model:

1. The main arch has a slightly variable thickness. We consider a constant thickness of 1 meter.
2. The thickness of the different septa is considered constant for all 6 equal to 0.50 meters.
3. The 0.40 meter thick slab is not constant along the whole bridge. It is considered up to the last arch (the one closest to the keystone of the main arch). From then on we hypothesize filling. This is because there is no space at the top for the 1 meter thick arch and the 40 cm thick slab at the same time so

we think there is not the slab. The filling reduces itself going towards the keystone because the distance between the arch and the road surface become smaller.

4. We consider additional non-structural masses that simulate road paving (asphalt) and where it is present also filling.

In this first phase the material adopted have the same mechanical parameters for all the elements both beams and shells.

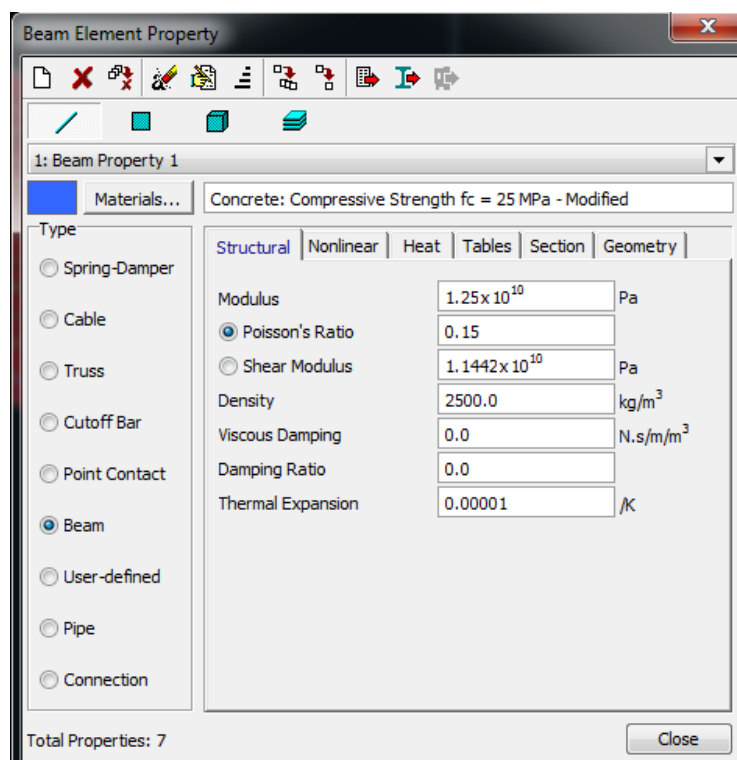


Figure 3.36 Characteristics of beam element in model with reduced stiffness

Another important topic is the creation of the mesh. In this case it was created by exploiting the function of the software that allows to generate it automatically after choosing the element to be adopted. The model has a mesh with quadrangular elements.

It was decided to consider two different constraint conditions due to the uncertainties on the current conditions of the abutments of the bridge. Thus, we have decided to analyze four different models:

- model with hinge and yielding on one side and hinge on the other side (Cannara side);
- model with hinge and yielding on one side and fully restrained on the other side (Cannara side);
- model with hinge and yielding on one side and hinge on the other side (Cannara side), 50% reduction in initial stiffness;
- model with hinge and yielding on one side and fully restrained on the other side (Cannara side), 50% reduction in initial stiffness.

At this point the modal analysis is launched for the four different models and so it is possible to obtain the results in terms of the structure's own vibration periods and relative modal forms for the first 20 ways of the structure vibrations. The study of modal forms will be the basis of the dynamic experimental tests and of the definition of sensor positioning.

3.7.3 MODAL ANALYSIS

The different models differ in terms of restraint conditions and stiffness. It was possible to extract the first twenty modes of vibrating of the bridge thanks to the calculation software. The modal participation factors were determined in relation to the six degrees of freedom of a rigid body in the space:

- traslation in x direction
- traslation in y direction
- traslation in z direction
- rotation in x direction
- rotation in y direction
- rotation in z direction

However not all ways of vibrating are significant. In seismic analysis it is necessary to consider the percentage of the participating mass of the single mode of vibration to understand which are more representative of the behavior of the structure and then to carry out an analysis of the extracted modal forms.

In the paragraph 7.3.3.1 of the technical standards for constructions (NTC2018) is written: "all modes to be considered should have a participating mass greater than 5% and a number of modes whose total participating mass exceeds 85%". The modal participation factors are considered in seismic analysis when the actions come from the support (for example during an earthquake). When actions come from traffic, as in our case, the important modes can also have a low participation factor. Thus we should analyze each modal form and identify which degree of freedom is involved regardless the values of the participation factors.

Obviously these results must be considered taking into account the fact that we realized a rough FEM model.

The table below shows the total mass participation factors for all twenty modes for each degree of freedom.

MODEL	Xtransl.	Ytransl.	Ztransl.	Xrot	Yrot	Zrot
Hinged on the side without yielding	90.17	82.29	78.39	88.68	79.94	80.34
Fully restrained on the side without yielding	89.57	82.64	77.56	88.95	79.30	80.92
Hinged on the side without yielding (reduced stiffness)	90.17	82.29	78.39	88.68	79.94	80.34
Fully restrained on the side without yielding (reduced stiff.)	89.57	82.64	77.56	88.95	79.30	80.92

Table 3.13 Total mass participation factors for all twenty modes for each degree of freedom

It is possible to observe that the first 20 modes extracted excite more than 85% of the total mass of the whole structure only for the translation in the x direction and for the rotation in the x direction. In particular, the first 18 modes are enough to excite 85% of the whole mass of the structure relative to the rotation in x direction in every models. While 15 modes are enough to excite 85% of the total mass of the bridge

relative to translation in x direction in the model fully restrained on the side without yielding. The values don't change if we consider the models with reduced stiffness.

In my analysis it was necessary to identify the vertical modes and torsional modes. We decided to not focus our attention to lateral modes and local modes. In this way the professor Ubertini and me decided to install the accelerometers in vertical direction as much as possible aligned on the same line.

The tables below show the most important vertical and torsional vibrating modes among the 20 extracted through the FEM software for each model. They are characterized according to the natural frequencies, the oscillation periods and the characteristics related to each single mode.

Model hinged on the side without yielding			
Mode	Frequency (Hz)	Period (s)	Description
1	2.1291	0.4697	Vertical mode prevails
2	3.4291	0.2916	Vertical mode prevails
3	5.1244	0.1951	Torsional mode prevails
6	8.2139	0.1217	Vertical mode prevails

Table 3.14 Characteristics of fem model hinged on Cannara side

Model fully restrained on the side without yielding			
Mode	Frequency (Hz)	Period (s)	Description
1	2.3422	0.4269	Vertical mode prevails
2	3.7830	0.2643	Vertical mode prevails
3	5.5676	0.1796	Torsional mode prevails
6	8.9762	0.1114	Vertical mode prevails

Table 3.15 Characteristics of fem model fully restrained on Cannara side

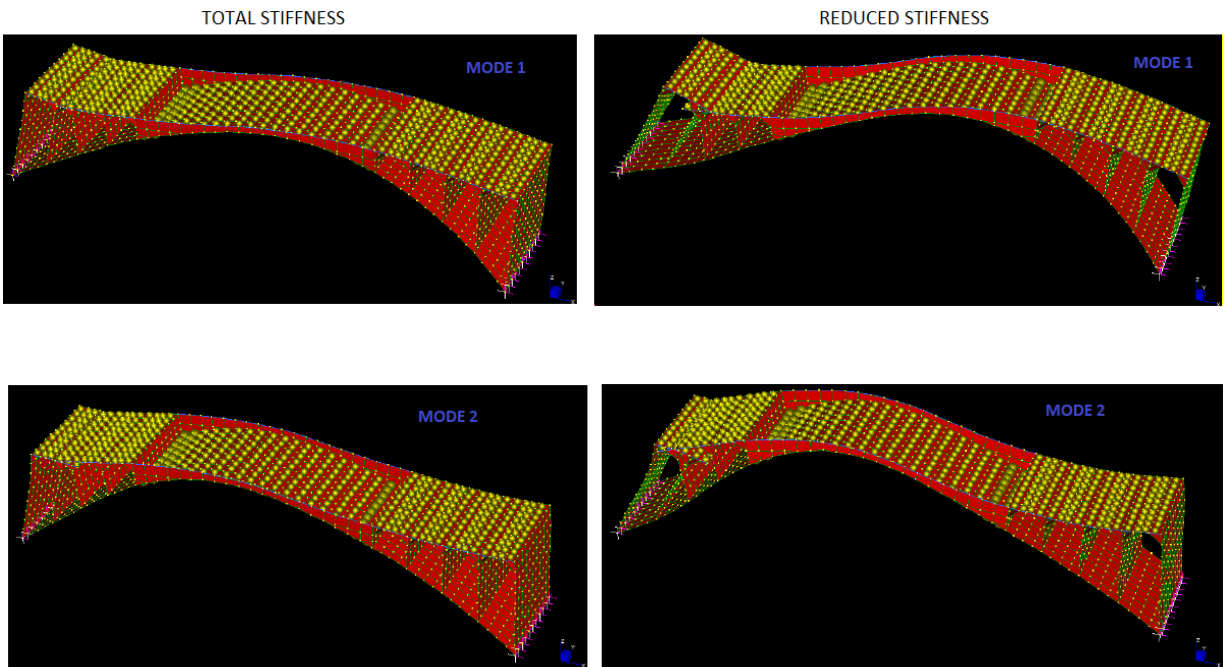
Model hinged on the side without yielding (reduced stiffness)			
Mode	Frequency (Hz)	Period (s)	Description
1	1.4244	0.7020	Vertical mode prevails
2	2.1815	0.4584	Vertical mode prevails
3	3.8993	0.2565	Torsional mode prevails
6	6.2181	0.1608	Vertical mode prevails

Table 3.16 Characteristics of fem model hinged on Cannara side with reduced stiffness

Model fully restrained on the side without yielding (reduced stiffness)			
Mode	Frequency (Hz)	Period (s)	Description
1	1.6685	0.5993	Vertical mode prevails
2	2.4511	0.4080	Vertical mode prevails
3	4.0114	0.2493	Torsional mode prevails
6	6.7323	0.1485	Vertical mode prevails

Table 3.17 Characteristics of fem model fully restrained on Cannara side with reduced stiffness

It is possible to see, analyzing the obtained results, how the frequency values change profoundly considering the stiffness value reduced by 50% in the hinged and fully restrained model. If we compare the same vibrating modes between models with reduced stiffness and models with total stiffness we see that the first have lower frequencies values. Furthermore, it is possible to observe how the frequency value of the most important vertical modes and torsional modes are never higher than 10 Hz. The images below show the main vertical and torsional modal forms relating to hinged model:



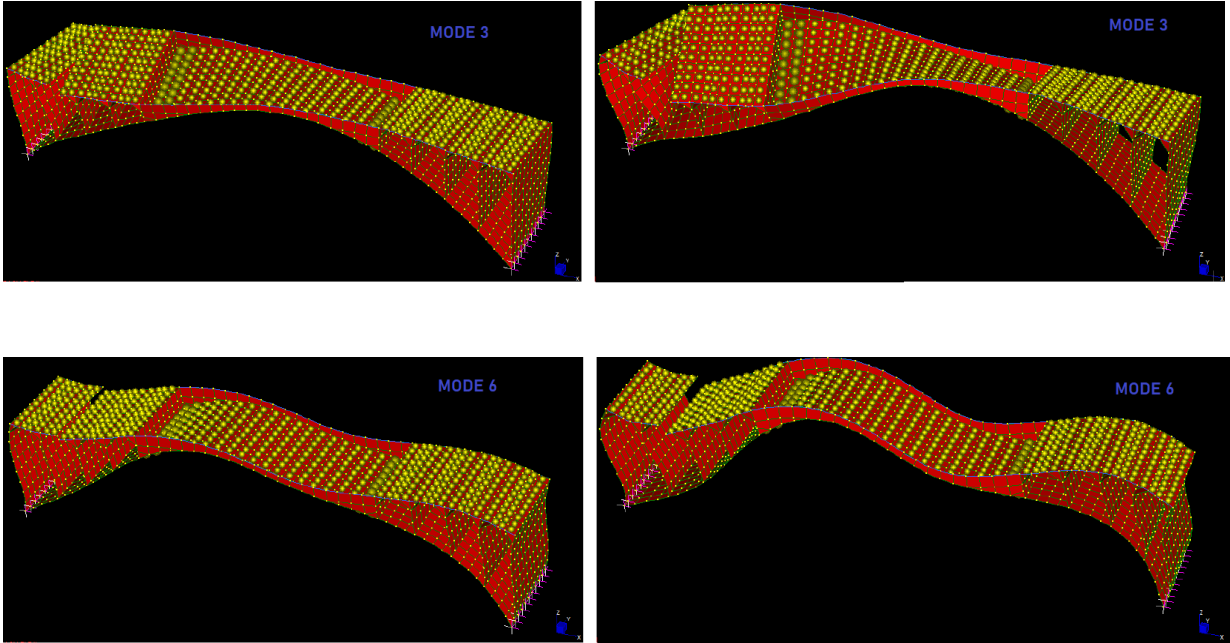
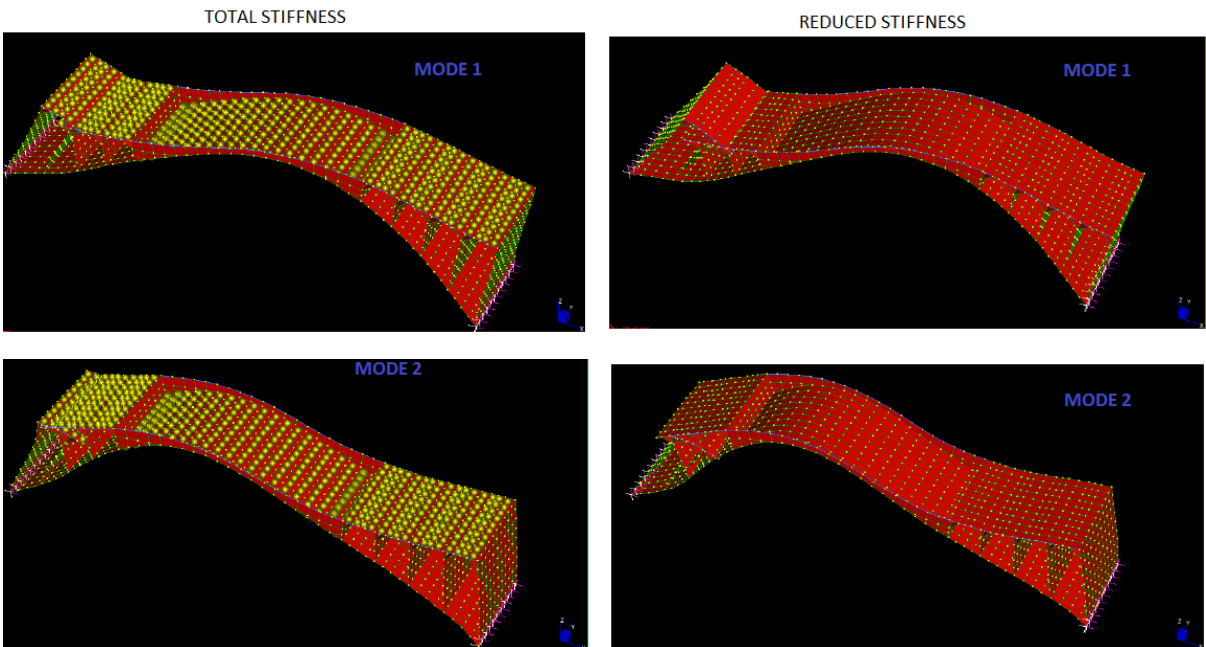


Figure 3.37 Main vertical and torsional vibrating modes of the model hinged on Cannara side

The images below show the main vertical and torsional modal forms relating to fully restrained model:



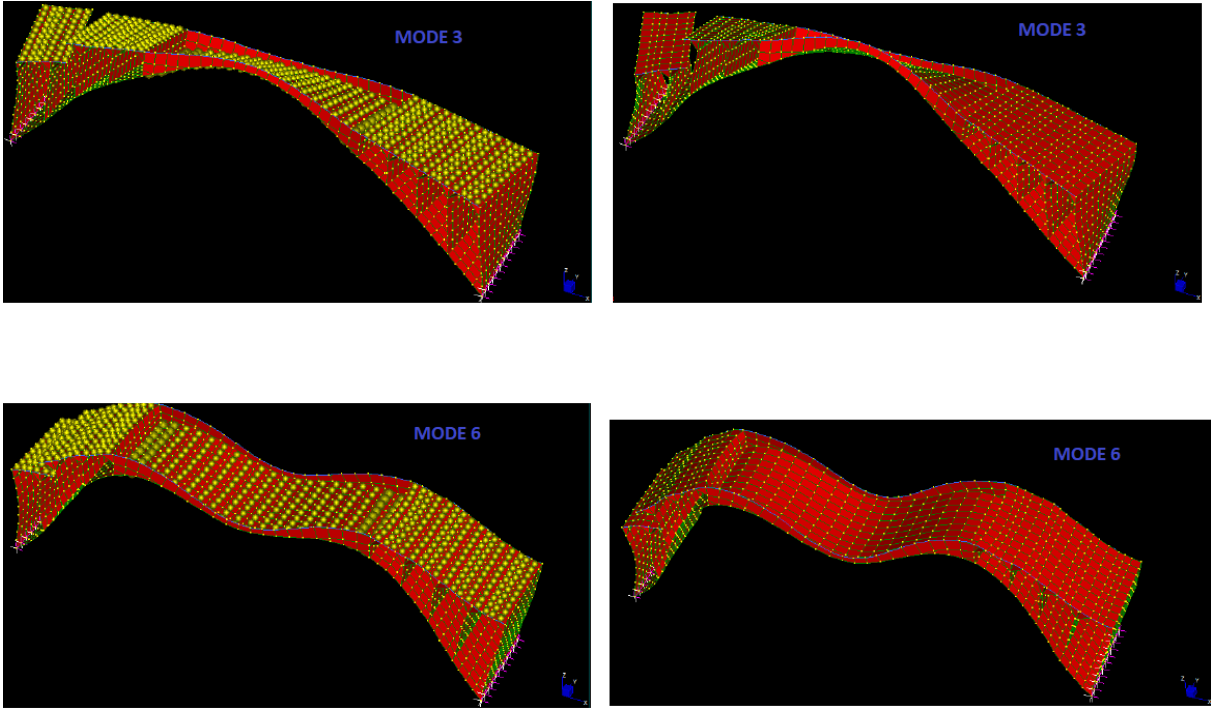


Figure 3.38 Main vertical and torsional vibrating modes of the model fully restrained on Cannara side

3.8 MONITORING ACTIVITY

In the days before the monitoring activities an inspection on site was carried out to identify the actual state of the bridge and to understand how to better organize the experimental tests. The crack pattern appeared immediately defined. The plastic hinge in the main arch in present. It is the same which professor Balli spoke about in his report of the Cannara bridge in 1997. The conditions of the third arch on the opposite side to the Cannara center are critical. It is possible to see how the reinforcements have expelled the concrete cover and they are visible along the total length of the arch. The reinforcements have been treated with a mortar with alkalizing and anticorrosive properties. Looking carefully it is possible to see that the bars have continued to fall down after the intervention. Therefore, the situation cannot be defined as completely stabilized. The images below show the status of the bridge.



Figure 3.39 Condition of the third arch opposite to the center of Cannara during inspections

The experimental tests were carried out on 13 and 14 of November 2019. The preparation of the tests did not record particular delays and setbacks despite during the day of installation small rainfall phenomena of precipitation occurred. The instrumental sections were decided by the professor Filippo Ubertini, professor of bridge design at University of Perugia, in agreement with the NBG Systems company. It was decided to install 6 accelerometers on the two sides of the bridge at deck level in vertical direction, as much as possible aligned with each other. Three of six on one side and the other three on the other side. In particular one is installed in the middle of the arch and the other two on the septum closest to the key of the main arch in symmetrical configuration. The two inclinometers were installed near the kidneys of the arch in symmetrical configurations under the accelerometers only on one side (right side). The 4 strain gauges (L-bracket sensors) were installed to monitor the cracks behavior: two of them under the arch straddling the crack that runs the total width of the bridge; the other two were located at deck level in diagonal position on the two sides of the bridge.

The installation of sensors took place on Tuesday 13th November 2019. It was used a platform with a basket so we decided to partially change the traffic flow closing a lane alternately. On the opposite side to the center of Cannara it was possible to use the ladder to install the sensors in order to restore the normal vehicles circulation.

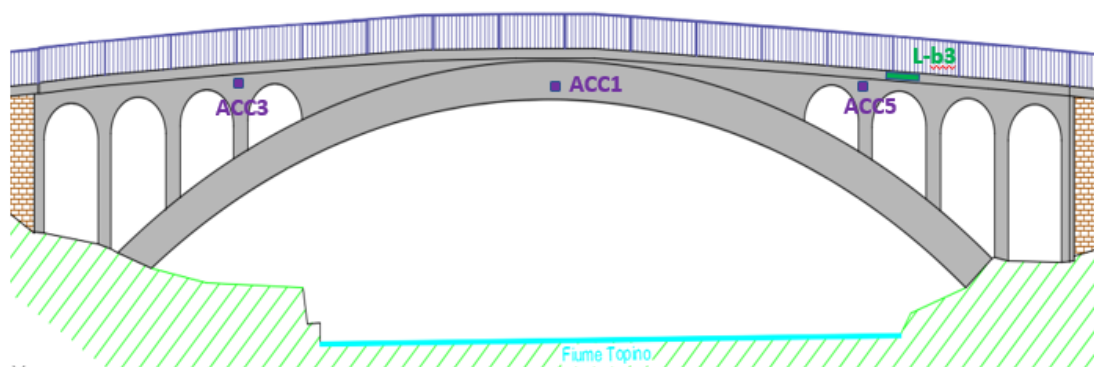


Figure 3.40 Position of the sensors on the left side of the bridge

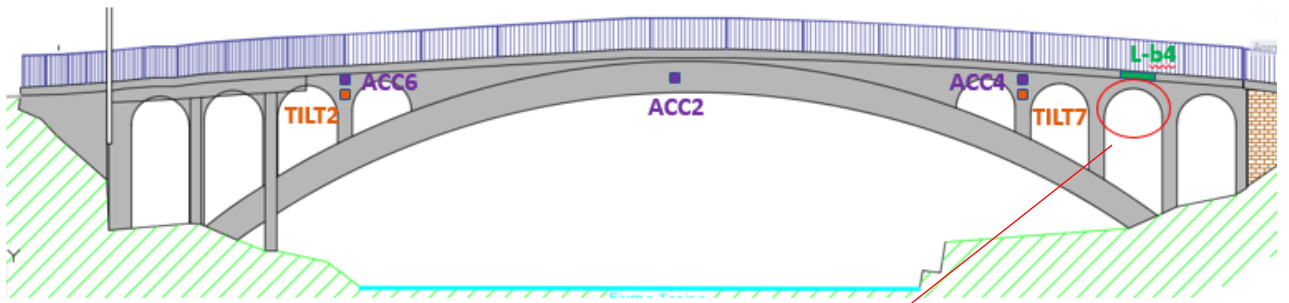


Figure 3.41 Position of the sensors on the right side of the bridge



Figure 3.42 Position of the L-b1 on left and L-b2 on right under the arch

The interrogation unit was located in a cabinet on the right side opposite to the center of Cannara. The FBGuard has 8 channels. We decided to use only seven of them. So we connected some sensors in series. The choice on how to connect them depends on the reflectivity coefficient. The sensors with low reflectivity are usually placed first because during the path of the fiber there are attenuation phenomena that should be minimized. The reflectivity of tilt meter is around 70% while for accelerometers the value is 30%. For this reason we decided to put in series first accelerometers and then the tilt meter. The L-brackets have only one entry, so they were each connected to a

channel. L-b1, L-b3 and L-b4 have 2 FBGs: one has the task of measuring only the temperature, the other one measures the temperature and the strain. It is possible to measure the opening of the cracks through the compensation of these two values.



Figure 3.43 Interrogation Unit

Furthermore the interface of the control unit gives us an indicative information of the temperature. For dynamic measurements it is not necessary to use this type of sensors because temperature is irrelevant, so we can use sensors with only one FBG like the L-b2. The connections were realized using a 3 mm diameter fiber optic cable. The tables below show the details of the channels and the characteristics of L-brackets (strain sensors).

FBGuard channel	SENSOR
1	L-b1
2	L-b2
3	L-b3
4	L-b4
5	Acc4 – Acc2 – Acc6 – Tilt2
6	Acc3 – Acc1 – Acc5
7	Tilt7

Table 3.18 Channels of FBGuard

SENSOR	DIMENSION	WAVELENGTH OF FBG FOR TEMPERATURE	WAVELENGTH OF FBG FOR STRAIN AND TEMPERATURE
L-b1	330 mm	1562 nm	1569 nm
L-b2	500 mm	-	1573 nm*
L-b3	1030 mm	1552 nm	1559 nm
L-b4	1030 mm	1552 nm	1559 nm

*there is no temperature measurement

Table 3.19 Characteristics of strain gauges

The two tilt meters located on the right side have different wavelengths. Each tilt meter has 2 FBGs, both measure the inclination. The FBGs work in push-pull. Inside there is a pendulum that is very sensitive. The temperature variations are compensated directly by the sensor. Tilt meter 7 has two gratings with these values: 1568 nm and 1574 nm. They can change by a maximum of 2 nm.

The recordings were realized in environmental conditions and with the use of a heavy truck (30140 kg) available by the Province. On Wednesday morning, 13 November there were realized the test with the truck. Several test were organized by professor Ubertini in the two different direction with different speed. It was decided to place one or two wooden plates in the middle of the carriageway during the passage of the truck. Furthermore it was decided to close the completely bridge during each passage of the truck and to reopen it at the end of each passage to not create too many mistakes. The sampling frequency during adopted during the test was 250 Hz. The table below shows the detail of the test with the heavy truck.

SPEED	TIME	PASSAGE TIME	DESCRIPTION
≈5 Km/h	12.34	≈23 seconds	No plate
≈5 km/h	12.38	≈21 seconds	No plate
10 km/h	12.42	≈18 seconds	No plate
10 km/h	12.47	≈16 seconds	2 wooden plates
15 km/h	12.50	≈13 seconds	2 wooden plates
15 km/h	12.55	≈14 seconds	2 wooden plates
20 km/h	13.01	≈10 seconds	1 wooden plate
30 km/h	13.08	≈7 seconds	1 wooden plate
≈40 km/h	13.20	≈7 seconds	1 wooden plate

Table 3.20 Details of the test with the truck of 30 tons

In the afternoon of the same day it was organized a test with the heavy truck increasing the sampling frequency. It was possible turning off all the channels of the FBGuard except the number 5 and 6 (the two relating to accelerometers). The sampling frequency was 1000 Hz. The table below shows the detail of the test.

SPEED	TIME	PASSAGE TIME	DESCRIPTION
10 km/h	17.40	≈16 seconds	2 wooden plates
15 km/h	17.47	≈13 seconds	2 wooden plates
≈5 km/h	17.50	≈21 seconds	2 wooden plates

Table 3.21 Details of the test with the truck of 30 tons

The day after, on Thursday 14 November, acquisitions were carried out with environmental excitement without closing any lane. In this case the sampling frequency was 250 Hz (all the channels in use). The acquisitions lasted 50 minutes.

3.8.1 MONITORING EQUIPMENT

It has already been written that on the bridge three different kinds of sensors were installed at critical points produced by the company NBG Systems. In particular we used to monitor:

- 6 FBG Accelerometer FBGA-01
- 2 Tilt Meter FBGTi-01
- 4 Strain Sensor FBGS-01

All of them are connected by an optical fiber which arrives directly to the interrogation unit FBGuard 1550 FAST. In the next pages I will describe in detail the equipment used in monitoring.

3.8.2 FBG ACCELEROMETER FBGA-01

The accelerometer is a device that is used to measure structural vibrations. It has application in different areas going from aerospace and aeronautical to mechanical and civil engineering. The importance of measuring structural vibration is to avoid

negative dynamic effects such as resonance, fatigue and instability that can endanger structural integrity and human health.

The FBG accelerometer FBGA-01 is a fiber optic version of the conventional accelerometer but completely passive, offering inherent insensitivity to environmental-induced noise. It is suitable for a large range of applications where low frequency and small amplitude accelerations are present.



Figure 3.44 FBGA-01 accelerometer

The FBGA-01 is a single axis FBG accelerometer sensor, suitable for low frequency measurement of small vibrations. The sensor is ideal for the measurement of structural responses to dynamic stimuli, for instance buildings during earthquakes, wind turbines under gust loading, ship hulls under wave loading. The high sensitivity and linearity, as well as the flat frequency response and low transverse sensitivity of the accelerometer make it especially suited for civil engineering applications. Its robust design meets the IP68 protection standards and includes aluminum case and input/output fiber optic armor cables meaning that it can be installed outdoors under severe conditions and without extra protection. It provides high accuracy and resolution measurements, and total fiber optic design ensuring intrinsic immunity to electric sparks and EMI/RFI and no ignition risk. The accelerometer combines compact size and high resistance to corrosion and harsh environments with long-term reliability. It is also appropriate for remote sensing being possible to locate it several kilometers away from the measurement unit. It offers intrinsic multiplexing capability

that allows the concatenation of a large number of sensors in a single optical fiber. Therefore this sensor is particularly suitable for difficult-to-reach locations and large scale sensing networks.

The tables below are the data sheet relating to the sensor and the wavelength of each accelerometers.

Sensitivity	75 pm/g @ 40 Hz (typical)
Measurement range ¹	±10 g
Frequency range	0 to 50 Hz
Resonance frequency	430 Hz (typical)
Flatness	< 2 %
Resolution ²	12.5 µg/√Hz
Transverse sensitivity	< 0.1 %
Central wavelength	1510 to 1590
Spectral width (FWHM)	< 0.2 nm
Reflectivity	> 75 %
Insertion loss	< 0.1 dB
Side lobe suppression	> 10 dB
Cable type	Ø 3 mm outdoor (armor)
Cable length	1 m each side (±3 cm)
Connectors	FC/APC
Operation temperature	-20 °C to +80 °C
Relative humidity	< 90 % at 80 °C
Protection class	IP68
Packaging	Aluminium
Dimensions	H 73 mm, D 53 mm
Weight	250 g

¹range may be customized upon request ²dynamics, FFT analysis

Table 3.22 Data sheet FBGA-01 accelerometer

SENSOR	WAVELENGTH
ACC 1	1550 nm
ACC 2	1550 nm
ACC 3	1530 nm
ACC 4	1530 nm
ACC 5	1540 nm
ACC 6	1540 nm

Table 3.23 Wavelength of accelerometers

3.8.3 TILT METER FBGTi -01

The FBGTi-01 Tilt meter is an inclination sensor based on Fiber Bragg Gratings (FBGs). The Tilt Meter is designed to measure small vibrations of angle towards the vertical without the need for temperature compensation. This sensor is completely passive, offering inherent insensitivity to environmental induced noise.

The FBGTi-01 features good linearity, no hysteresis and effective temperature compensation by using two FBGs in an innovative push-pull configuration. The sensor's total fiber optic design ensures intrinsic immunity to electric sparks and EMI/RFI. The tilt meter combines compact size, high resistance to corrosion and harsh environments with long-term reliability. It is protected against rain and moisture as IP68 glands are used in the buffer/sensor connections.



Figure 3.45 Tilt meter FBGTi-01

It's also suitable for remote sensing being possible to locate it several kilometers away from the measurement unit. It offers intrinsic multiplexing capability that allows the concatenation of a large number of sensors in a single optical fiber. It is also particularly suitable for difficult-to-reach locations and scale sensing networks.

The table below shows the data sheet of this sensor.

Sensor	
Sensitivity ¹	500 pm/deg
Measurement range	10 deg (±5 deg)
Resolution ²	0.002 deg
Maximum calibration error	0.05 deg
Optical	
Central wavelengths	1500 to 1600 nm
Spectral width (FWHM)	< 0.2 nm/FBG
Reflectivity	> 65 %
Side lobe suppression	> 10 dB
Inputs/Outputs	
Cable type	Ø 3 mm outdoor (armor)
Cable length	2 m each side (±5 cm)
Connectors	FC/APC SC/APC NC (No Connector)
Environmental	
Operation temperature	-20 to 80 °C
Cross sensitivity	< 0.03 %/°C
Settling time	1.5 sec
Mechanical	
Materials	Stainless steel
Dimensions	220 x 140 x 42.5 mm
Weight	3.3 kg
¹ typical value calculated from the wavelength difference between the two FBG	
² for 1 pm resolution in wavelength measurement	

Table 3.24 Data sheet Tilt meter FBGTi-01

3.8.4 STRAIN SENSOR FBGS-01

The fiber optic Strain Sensor FBGS-01 is a long base strain gauge which measures tension or compression between two fixed points. It is based on Fiber Bragg Grating (FBG) technology. It can be used to measure strain changes on the surface of material of metallic or composite structures due to tension, compression or bending. This allows for the continuous structural health monitoring of structures, crack and fissure formation in (concrete) walls, monitoring of bridges, dams, buildings, tunnels and other complex structures etc.

The standard gauge length can be chosen between 250 mm and 2 meters. The sensor has connectors on both ends and can be used alone or in series as a part of an FBG sensor array. Installation and cabling for such arrays is much less expensive and less cumbersome than comparable electronic gauge networks.



Figure 3.46 Strain sensor FBGS-01

The strain sensor is the fiber optic equivalent of an electrical strain gauge and can be mounted directly on the surface of a structure by means of an adhesive. The sensor is supplied with two aluminum L – brackets and fasteners which facilitate a mounting on a structure. In this way, the fiber sensor makes direct contact with the surface and therefore accurately measures the strain at the surface.

It is like the previous ones immune to electric sparks and EMI/EFI. It features high accuracy and resolution. It is also suitable for remote sensing and it is possible to install it kilometers away from the measurement unit. It is protected against complete, continuous submersion in water guaranteeing IP68 protection.

The table below shows its specifications.

Sensor length ¹	0.250 m up to 2 m
Strain range	-0.5 % shortening and +1 % elongation
Strain sensitivity	1.2 pm/με
Operating temperature	-20 °C up to +60 °C
Central wavelength	1510 to 1590 nm, 810-860
Connector type	FC/APC (standard)
Pigtail length	1.0 m (standard)
Anchor material	Aluminum
Cross sensitivity	10 pm/°C
Protection class	IP68

¹ measurement range and length may be customized upon request

Table 3.25 Data sheet strain sensor FBGS-01

3.8.5 FBGUARD 1550 FAST

The FBGuard 1550 FAST is compact, field proven, industrial grade FBG interrogation unit designed for reliable, long term field operation 24/7 which can be used for a broad field of applications. It is designed for high accuracy static and dynamic measurements of Fiber Bragg Grating (FBG) sensors. The device covers a wide wavelength range and provides simultaneous measurements at a very fast response rates and excellent wavelength resolution. The system can measure up to 8 optical channels with 40 FBG sensors per channel. This provide a cost-effective solution for industrial measurements.



Figure 3.47 FBGuard 1550 Fast

The FBGuard 1550 FAST contains a broadband light source and performs spectral analysis by means of a linear array detector and a spectrometer platform. The system is a fully autonomous unit with an embedded PC and a web server and is independent

from a range of external devices. The configuration of alarms, frequency of measurements, data logging on the integrated SSD et cetera is possible by SSH and the web interface of the FBGuard 1550 FAST. An Ethernet interface allows remote connection to any standard PC through the TCP/IP protocol. Additionally two USB 2.0 ports (serial communication is also supported at lower speeds) are available for data exchange. The system is equipped with four direct relays for immediate alarms. Additionally notifications can be sent via mail and SMS.

The system is supplied with an analysis configuration software, which is used to visualize the spectral information, calculate the peak wavelengths and convert the wavelength data into measurement data (strain, temperature, etc.).

The table below is the data sheet of the Interrogation unit.

Wavelength range *	1510 - 1590 nm
Number of channels	1,2,4 or 8
Wavelength resolution	≤ 1 pm
Wavelength repeatability	±5 pm
Absolute wavelength accuracy (EOL)	±30 pm
Scan frequency	Up to 11 kHz for single channel Up to 1 kHz for two channels Up to 500 Hz for four channels Up to 250 Hz for eight channels
Dynamic range	30 dB
Optical connector **	FC/APC
Durability of optical switch	> 10 ¹¹ cycles
Electrical, Environmental and Mechanical	
Power supply	12 V (adaptor to 230 V included)
Power consumption	< 50 W
Operating temperature	0 °C to 40 °C
Operating humidity	< 80%, non-condensing
Dimensions	482 x 415 x 140 mm ³ (3U, 19" rack) (18.9 x 16.3 x 5.5")
Weight	7.5 kg
Embedded PC	
Processor	Intel Core i3
Memory	4 GB
Hard disk	120 GB SSD Disk (no moving parts)
Communication protocol	TCP/IP MODBUS ***
Interface	Ethernet, USB 3.0 host port, tx VGA 4x alarm relays RS-485 *** RS-232 ***
External trigger	TTL, 2CH
Remote Control	Full control
Manufacturer	Safibra s.r.o. (www.safibra.cz)
Software	FBGuard Configuration Interface
* depending on light source ** be customized *** available on request	

Table 3.26 Data sheet FBGuard 1550 Fast

3.8.6 PHOTOGRAPHIC REPORT OF THE TEST

The images below are useful to understand the position of the sensors and the equipment used for installation.



Figure 3.48 L-b4 on the left and L-b3 on the right



Figure 3.49 Accelerometer 1 and accelerometer 3 on the left side of the bridge



Figure 3.50 Accelerometer 6 and tilt meter 2 on the left and accelerometer 4 and tilt 7 on the right



Figure 3.51 L-b1 on the left and installation of L-b2 on the right



Figure 3.52 Cannara Bridge during installation



Figure 3.53 Cannara Bridge during installation



Figure 3.54 Installation of Acc1 with basket on the left and the ladder used to install sensors on the right



Figure 3.55 The truck of 30 tons during the test and the analysis

4.DATA ANALYSIS

In this last part of the thesis work the results recorded by the sensors are shown. The goal of this part is to describe the data obtained by each sensor and to make a first qualitative analysis of these. It was decided to develop an analysis of the data in time-frequency domain. We focused on the data relating to standard traffic and on the tests carried out with the heavy truck only at speed of 15 km/h. It was possible to define the spectrogram graphs with reference to the different acquisitions. It gives us the frequencies evolution over time. Each of them shows high energy frequency peaks. The probable vertical and torsional modes of the structure at low frequencies can be identified by observing the peaks in Time-Frequency Distributions (TFD) curves characterized by high energy values.

4.1 NATURE OF THE RECORDED SIGNALS

The monitoring activities took place on 13 and 14 November 2019. It was decided to make acquisitions during standard traffic without any particular traffic restrictions and also during the passage of a truck. The tests performed with a truck of 30.140 kg were carried out at different speeds closing the road to any other vehicle. The signals during the standard traffic were recorded with an acquisition of 50 minutes. However, we have decided to consider an interval of few minutes for the analysis. The sampling frequency was 250 Hz in every acquisitions. This section shows the signals in time domain related to the three different sensors installed on the bridge: 6 accelerometers, 2 tilt meter and 4 L-brackets (strain gauges).

It was installed a router near the cabinet which contains FBGuard (Interrogation Unit). When the monitoring system was working it was possible to connect in real time via wi-fi to a link gave us by the NBG company, also with a simple smartphone, to understand if everything was working properly and to see the raw data of each sensor.

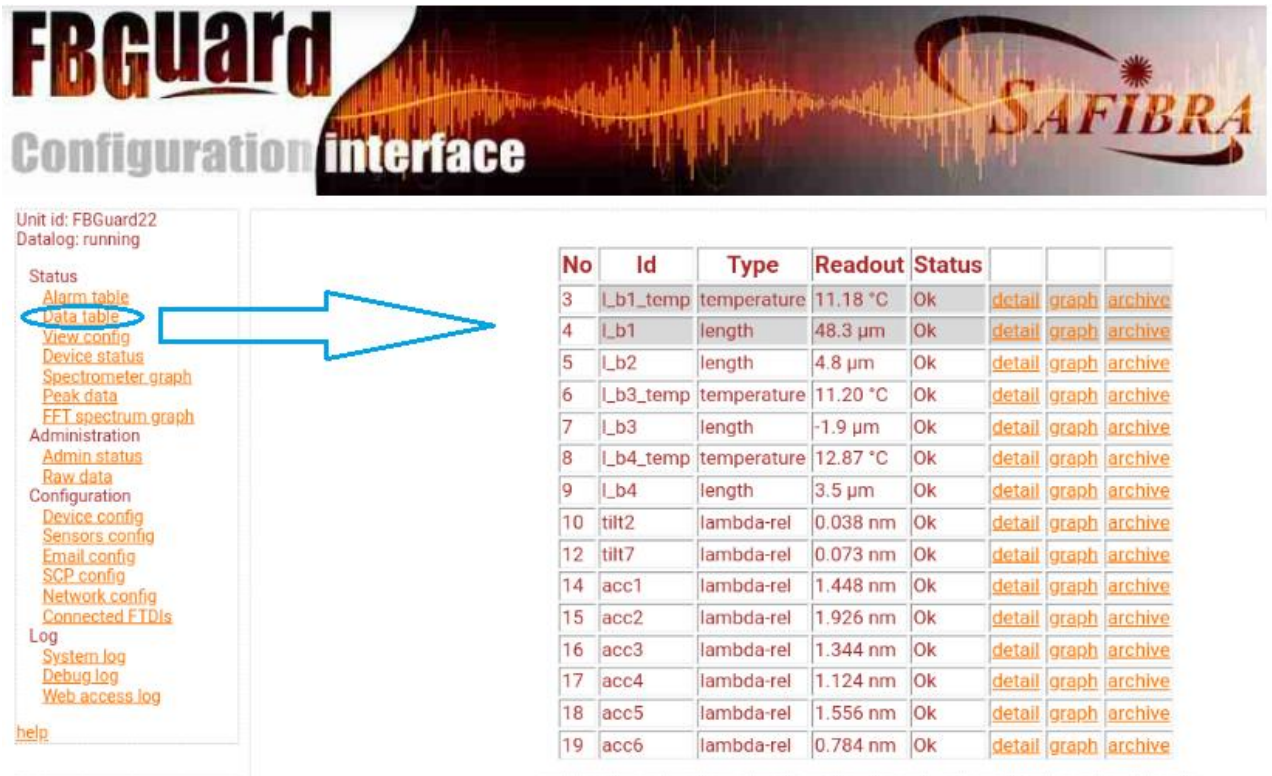


Figure 4.1 Interface FBGuard

The interface shows all the sensors installed on the Cannara Bridge. It is possible to see that for the L-b1, L-b3 and L-b4 (strain gauges), as already mentioned in the previous chapters, there are two different FBGs: one provides temperature and strain measurements while the other one provides only temperature measurements. The values related to this last one fbg are used for the compensation of the data and they can be also used as approximate information about the temperature on the bridge. The L-b2 has only one FBG. It measures the opening of the crack.

It is also possible to verify if the sensors are working correctly using the FBGuard interface. The FBGuard has 8 channels of which 7 have been used by our monitoring system. Each grating has a different wavelength that is in the range 1505-1585 perceived by the interrogation unit. It was necessary to check, for a correct operation of the sensors, that the intensity of each wavelength was greater than a limit value. The picture below shows the intensity of the wavelengths in channel 4 where is located the strain gauges L-b4.

any channel channel_1 channel_2 channel_3 channel_4 channel_5 channel_6 channel_7 channel_8

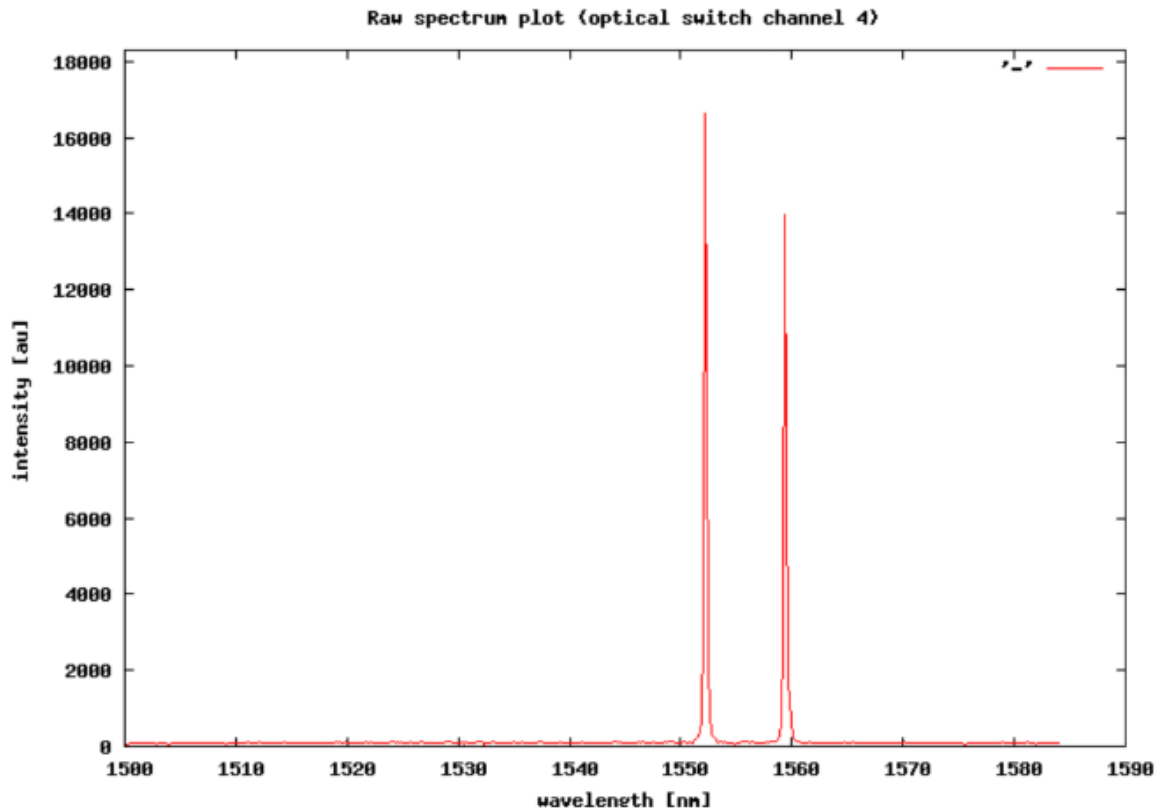


Figure 4.2 Intensity of signal in channel 4

Signal observation allows us to distinguish the peaks produced by vehicles of reduced mass from those corresponding to vehicles of bigger mass. It depends on how the peaks are high during the recordings. The signals were affected by thermal drift so it was necessary to filter the recordings. It was used a highpass Butterworth filter. Its order was 4 and the value of cutoff frequency used was 0.7. The images below show the filtered signals of two of six accelerometers in time domain related to standard traffic. In these images the recordings last 470 seconds.

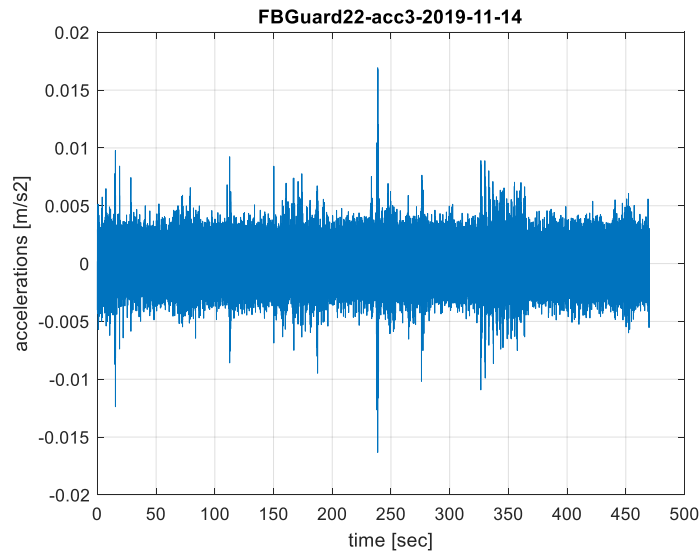


Figure 4.3 Signal in time domain of accelerometer 3 during standard traffic

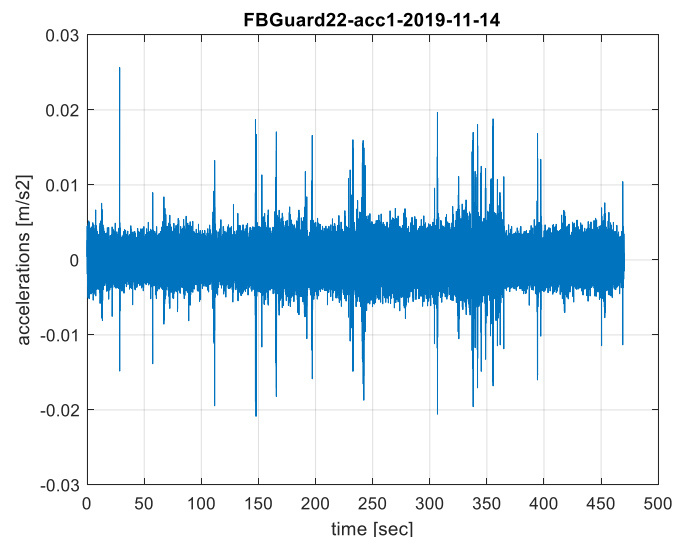


Figure 4.4 Signal in time domain of accelerometer 1 during standard traffic

It is possible to see that there are no obvious peaks in the two signals. The accelerations during standard traffic almost never exceed the value of 0.02 m/s^2 . The Butterworth filter deleted the thermal drift but the noise is yet present in the acquisitions. The causes of noise can be due to various factors. The ratio signal-noise seems to be not so high. The signals recorded by tilt meters during standard traffic don't show obvious peaks just like the accelerometers acquisitions.

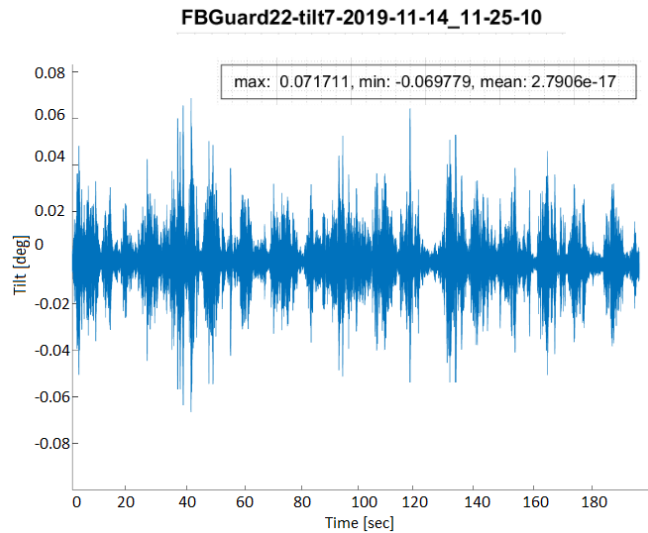


Figure 4.5 Signal of tilt 7 during standard traffic

The signal value recorded during standard traffic seems to be lower than the noise value. The noise masks almost completely the acquisitions during standard traffic. The nature of the signals recorded during heavy vehicle transit is completely different. The peaks are clearly identified in the acquisitions of the accelerometers and inclinometers. It is even possible to distinguish the passage of the three axles of the truck. In this part it was decided to show the graphs and the analysis related to the passage of a truck for speed equal to 15 km/h using 2 wooden plates with a thickness of 3 cm each. The images below show the acquisitions of the 12 sensors in time domain.

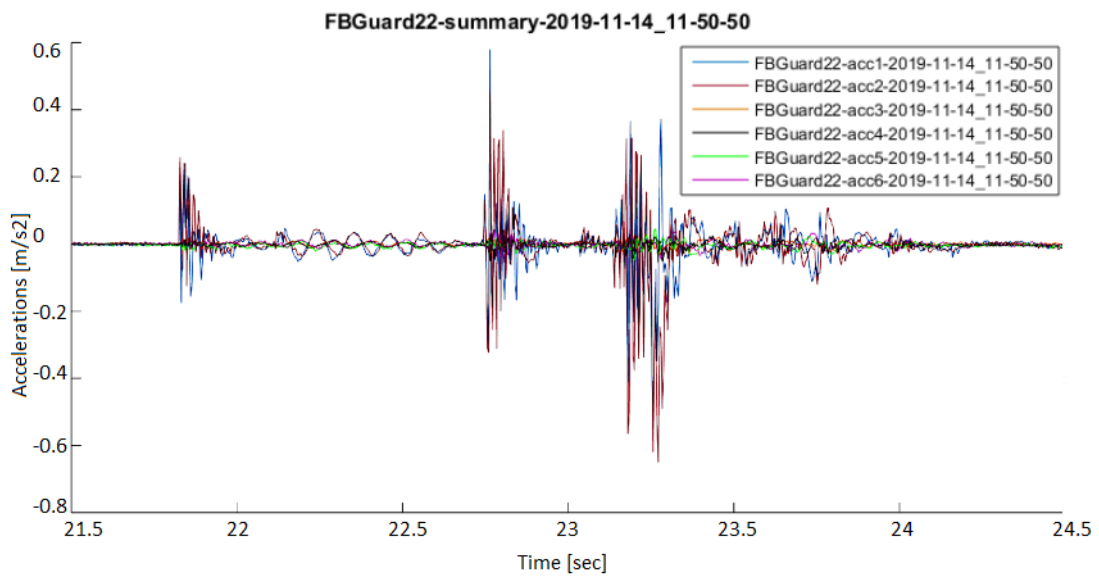


Figure 4.6 Signal in time domain of the 6 accelerometers during truck test

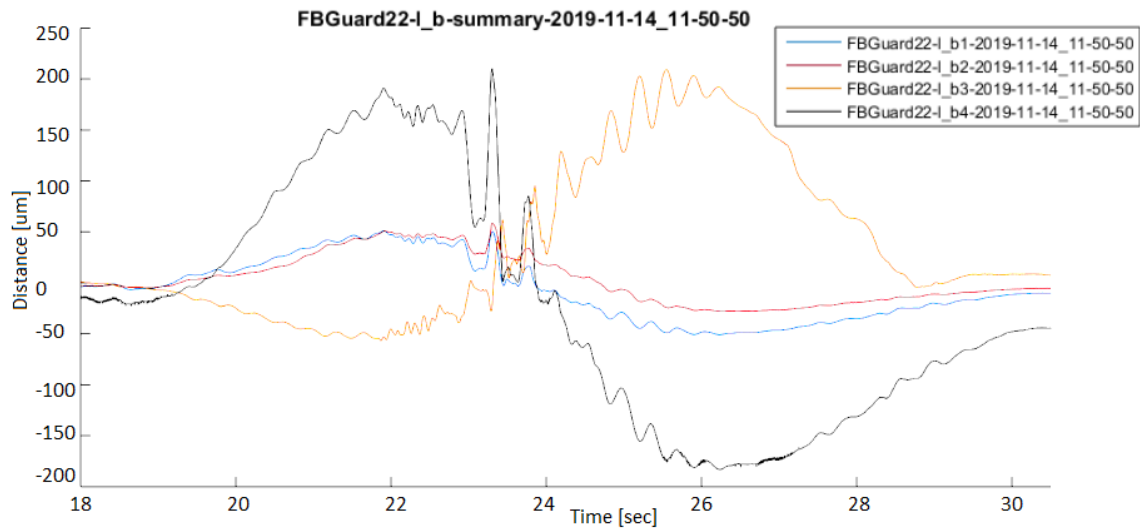


Figure 4.7 Signal in time domain of the 4 strain gauges during truck test

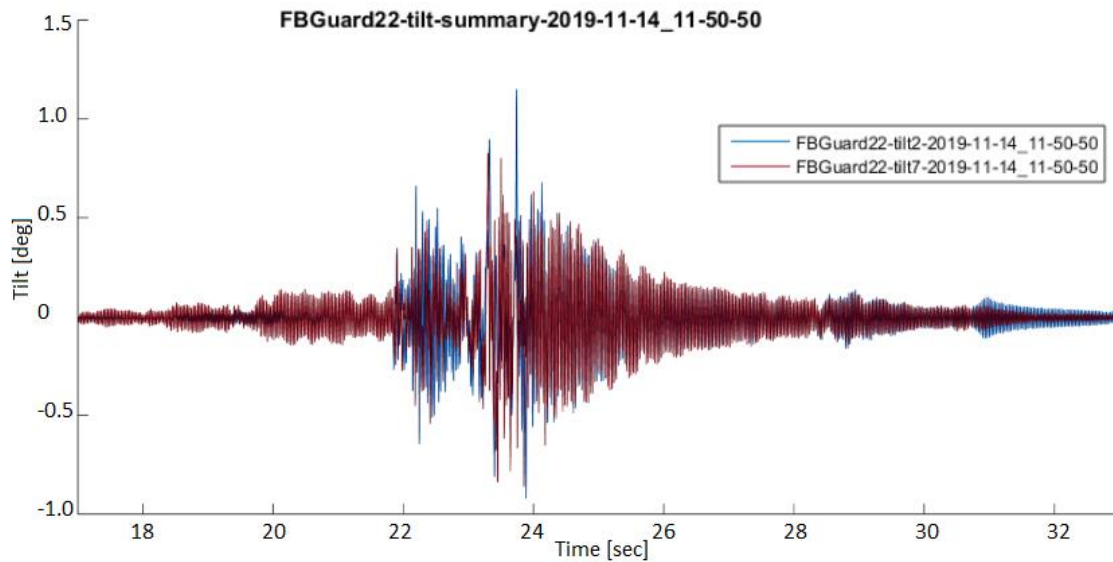


Figure 4.8 Signal of the 2 tilt meters during truck test

It is interesting to make a comparison between the values of the cracks opening recorded during the standard traffic and during the test carried out with an heavy truck. The images below show the results for each L-brackets sensor.

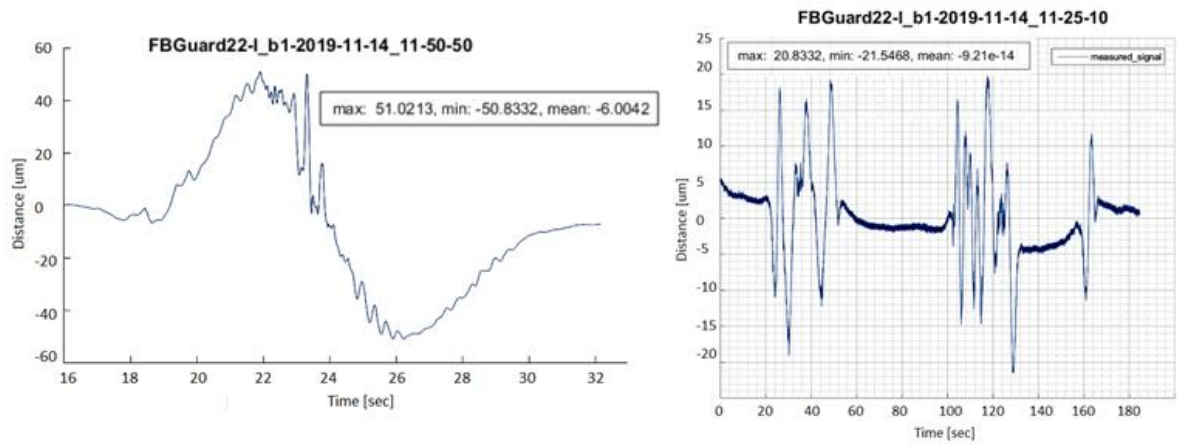


Figure 4.9 Signal of L-b1 during truck test on left and during standard traffic on right

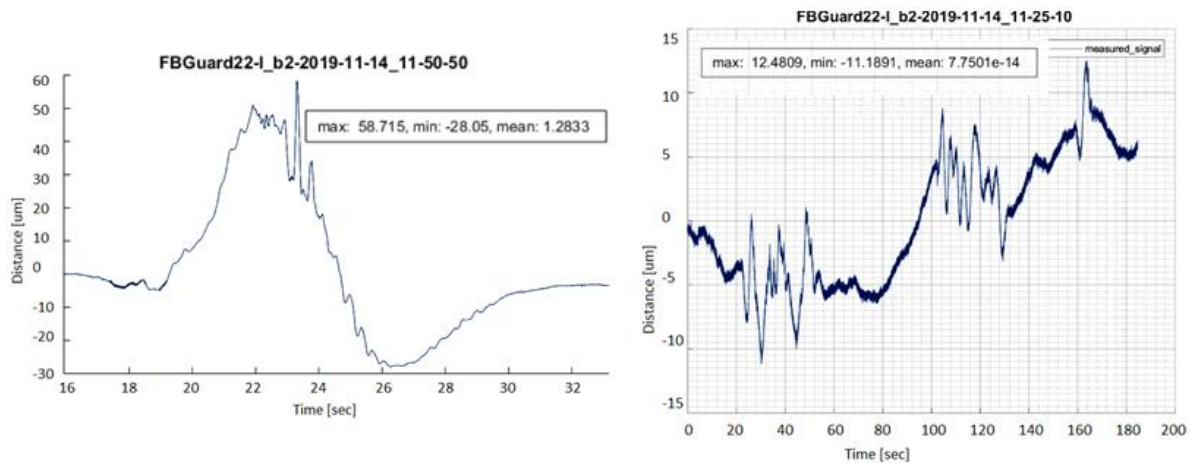


Figure 4.10 Signal of L-b2 during truck test on left and during standard traffic on right

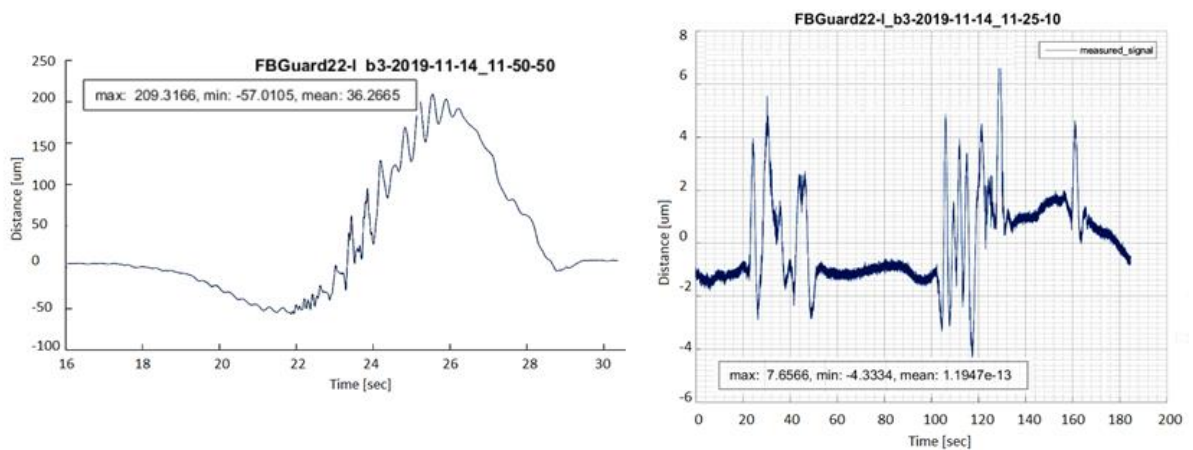


Figure 4.11 Signal of L-b3 during truck test on left and during standard traffic on right

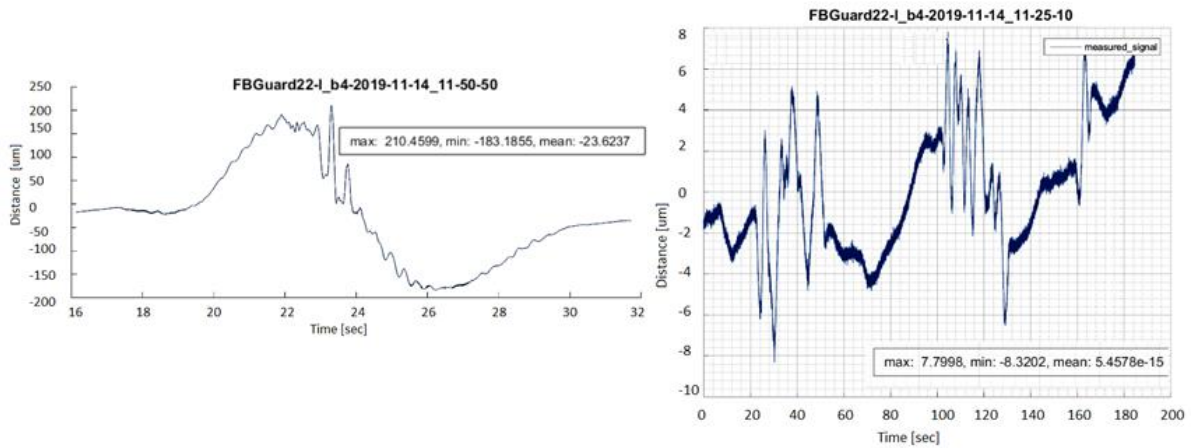


Figure 4.12 Signal of L-b4 during truck test on left and during standard traffic on right

The table below shows the maximum values of the cracks opening during the two acquisitions.

SENSOR	TRUCK [mm]	STANDARD TRAFFIC [mm]
L-b1	0.051	-0.021
L-b2	0.058	0.012
L-b3	0.209	0.007
L-b4	0.210	0.007

Table 4.1 Maximum values of cracks opening during standard traffic and truck test

It is possible to observe how the greater opening values are located in the slab (L-b3 and L-b4). The values of L-b1 and L-b2 obtained during standard traffic are not so different from those related to the passage of the heavy truck. The minus sign stands for the closure of the cracks while plus sign stands for opening cracks. The cracks are completely elastic: they close after few seconds from the passage of the truck. Therefore, the initial situation is restored. The order of size of the cracks opening is identical to that found in the test carried out in 2018.

4.2 FREQUENCY ANALYSIS

The study of a signal can be developed by analyzing the signal as a function of time; in this case we are in the time domain. It is also possible to consider the signal in the

frequency domain. In the time domain the study of the signal is carried out through its wave form, while in the frequency domain the study of the signal is carried out through its spectrum.

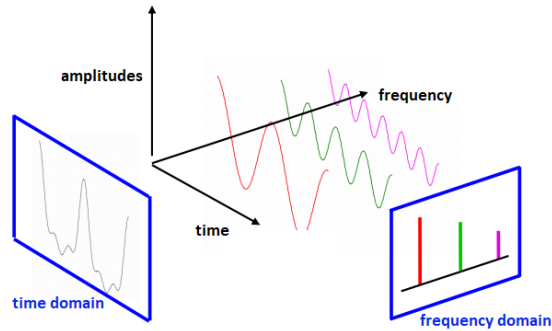


Figure 4.13 Transition from time domain to frequency domain

Fourier studied the transition from time domain to frequency domain. He has shown that for non-periodic function the signal spectrum is possible with an operation called Fourier Transform (FT).

$$X(f) = F \{x(t)\}$$

$$X(f) = \int_{-\infty}^{+\infty} x(t) e^{-j2\pi ft} dt$$

It is also possible to obtain the reconstruction of the original signal starting from its Fourier spectrum. This is obtained not from the sum of sinusoidal functions but from an integral called Inverse Fourier Transform (IFT).

$$x(t) = \int_{-\infty}^{+\infty} X(f) e^{j2\pi ft} df$$

A periodic signal is a sum of sinusoids having multiple frequency of f_0 . In this case, the spectrum is formed by a series of equidistant "lines". The situation changes in the case of aperiodic signals. The signal becomes a sum of sinusoids that can take any frequency. The spectrum is now represented by a continuous line.

A spectrum of a signal is characterized by two diagrams: one related to the amplitudes and the other one related to the phase which are both functions of the frequency. The graph of only amplitude is usually represented with respect to the frequency ignoring the phase angle. Otherwise the graph should be drawn as a curve in 3 dimensions: one for the real spatial variable and two to represent the complex values of the Fourier Transform.

If a signal is sampled at an insufficient frequency, when the signal is reconstructed starting from these samples, high frequency components of the original signal will appear as low frequency components in the reconstructed signal. This is the typical aliasing phenomenon. Therefore, it is necessary to take special attention to the sampling frequency.

The shape of a signal is defined by its frequency spectrum. If the signal has angular points and sharp oscillations, there are many high frequency components.

A signal can be filtered by removing high frequencies that contain noise. We cut the frequency spectrum of the signal above a given cut-off frequency. The sampling frequency needed to reconstruct the signal without loss must be at least twice the cut-off frequency. If the cut-off frequency is low, a lower sampling frequency will be required to accurately reconstruct the signal but less it will be similar to the original one.

The definition of Fourier Transform (FT) is only theoretical and it can not be applied to real cases. In practice we perform the Discrete Fourier Transform (DFT) which is an operation equivalent to the Fourier Transform conceived to operate in the discrete field. The Discrete Fourier Transform (DFT) has a computational load equal to N^2 , so the complexity increases with the square of the number of samples. For this reason, the Fast Fourier Transform (FFT) algorithm was introduced in the 1960s. This is more efficient and faster than the DFT. It has a computational load of $N \log N$. In this formulation the only constraint was that the signal must have a length N equal to the power of 2, but this problem has been solved in Matlab using corrective algorithms. The FFT calculates the spectrum of a signal starting from the samples. It operates on the N real samples and it transforms them into $N/2 + 1$ complex frequency samples

with constant spacing. Each of them consists of a real part and an imaginary part: the algorithm produces a linear trend on the frequency axis. It is important to remember that the upper limit to the available frequencies is given by the sampling frequency. If we indicate with f_c the sampling frequency the maximum frequency that can be represented is $f_c/2$. Therefore it is possible to use Matlab software in real cases. The "fast" version of the Fourier Transform (FFT) is implemented in it.

Spectral analysis is useful to detect phenomena that would not be observed if only a time domain analysis is developed. The evaluation of the peaks of the spectrum is carried out to determine the main characteristics of the signal. Today the FT is yet widely used but it has also limits. It is not useful when we have a frequency variation during the recording of a phenomenon. The frequency analysis loses completely time information. This usually doesn't allow an exhaustive description of the signal. For example the Doppler effect and the human voice have a frequency variation. In these cases a time-frequency analysis is used to analyze the data.

4.3 TIME-FREQUENCY ANALYSIS

The time-frequency analysis has been widely used since 1980. It can be considered a thorough Fourier's analysis. It is performed when we want not only the frequencies and their amplitudes but also it's important to know which frequencies have existed and in what times. The aim is to find functions able to represent the energy density simultaneously in time and frequency domain in a single graphical and analytical representation. Density is a quantity used very often in time-frequency analysis. We calculate the energy density every time we consider the signal squared or the Fourier Transform squared. The spectrogram identifies time, frequency and amplitude of a signal simultaneously. Time-Frequency distribution (TFD) performs the Fourier Transform to a part of the signal applying a window in time domain. We will consider the Fourier Transform for each translated window of an interval τ :

$$X(t, \tau) = \int_{-\infty}^{+\infty} x(t)h(t - \tau)e^{-j2\pi\nu t} dt$$

$H(t)$ function is the one that completes the $x(t)$ signal windowing process, it allows us to obtain the window signal $h(t-\tau)*x(t)$. It can be considered an “averaged spectrum” in the time interval. Therefore, it is not possible to guarantee for an instant of time an exact value of spectral content. Although this, it is considered a simple and widely used method.

Once the Short Time Fourier Transform (STFT) has been defined, the spectrogram is a completely trivial extension: it represents the time-frequency density of energy obtained from the STFT. Therefore, it can be calculated considering the squared absolute value of the STFT just shown above:

$$P_{SP}(t, \nu) = |X(t, \tau)|^2 = \left| \int_{-\infty}^{+\infty} x(\tau)h(\tau - t)e^{-j2\pi\nu\tau} d\tau \right|^2$$

The choice of the window is important for the signal analysis. If the windowing is too short the signal could be well defined but there is a problem: the uncertainty principle of the Fourier Transform. It is not possible to reduce band and duration of the signal, because one goes at the expense of the other. For this reason, it is possible to observe a big uncertainty when there is a change of frequency. On the other hand, the uncertainty principle is satisfied if we choose a windowing too long. Therefore we have signals determined under the point of view of dispersion in the time-frequency plane. In this case it's important to be careful not to capture even the wrong sinusoids (those too far back or too far in time). The only solution is to try the correct windowing until a correct compromise is reached between indeterminacy and overlapping of harmonics. In our analysis a 3000-point Hamming windowing was adopted. It was decided to integrate the acceleration values, after filtering them with an highpass Butterworth filter, to obtain displacement values. The double integration was carried out because the displacements are in relation with the slower modes of the structure and therefore with the lower frequencies. They are the most interesting vibrating modes. Furthermore the integrations filter more the signal unless of a multiplicative constant. The time-frequency analysis was developed both for acquisitions during standard traffic and during the passage of the truck of 30 tons. It is interesting to show

the spectrogram and marginal graphs. The first gives me informations about the energy content in time and frequency. In particular how frequencies evolve over time. The marginal graph gives only frequency information and it shows the frequency peaks at high energy. It can be considered the equivalent of Power Spectral Density (PSD) in the frequency analysis.

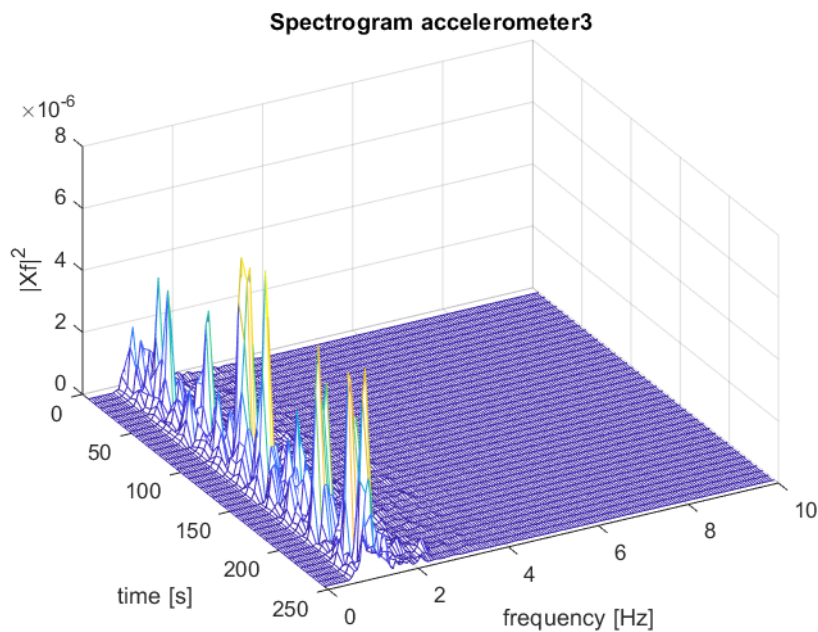


Figure 4.14 Spectrogram of accelerometer 3 located on the side opposite to the Cannara center during standard traffic

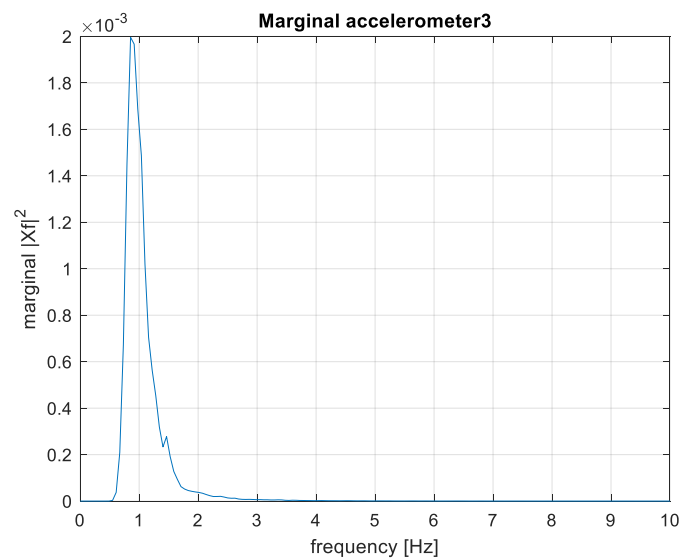


Figure 4.15 Accelerometer 3 opposite to the Cannara center during standard traffic

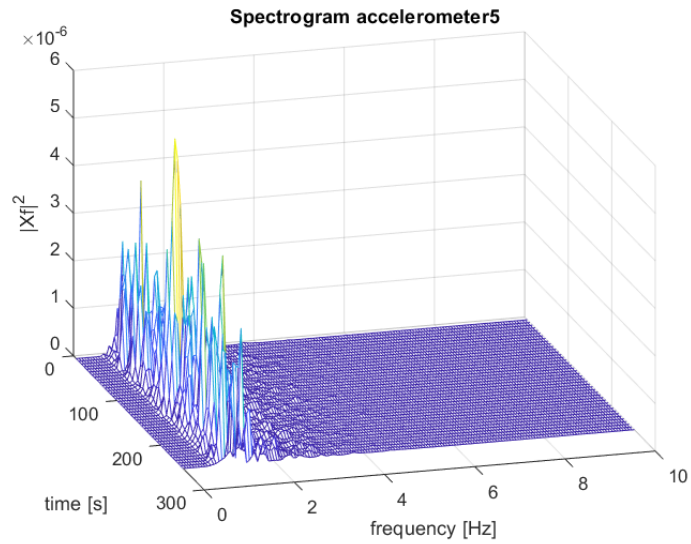


Figure 4.16 Spectrogram of accelerometer 5 located on the side of Cannara center during standard traffic

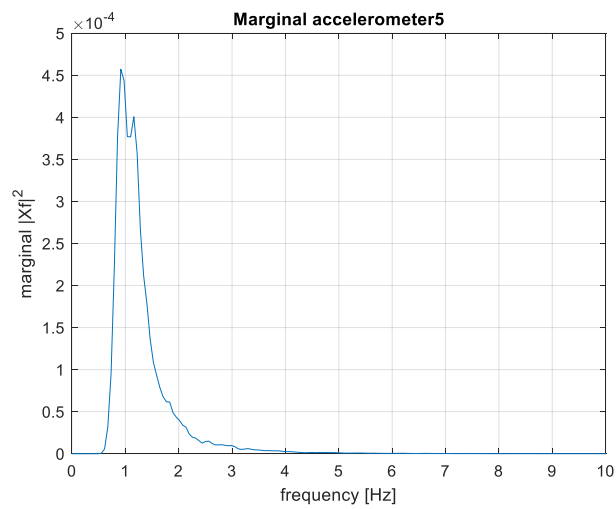


Figure 4.17 Accelerometer 5 on the side of Cannara center during standard traffic

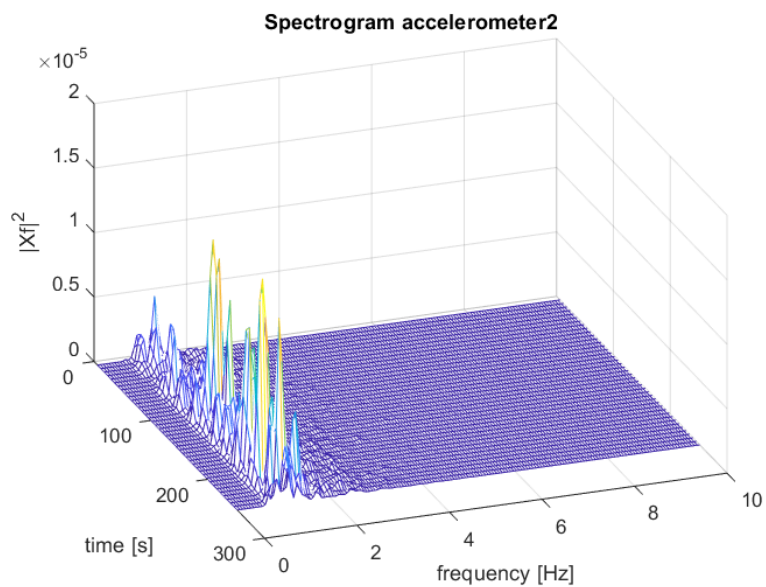


Figure 4.18 Spectrogram of accelerometer 2 located in the middle of the bridge during standard traffic

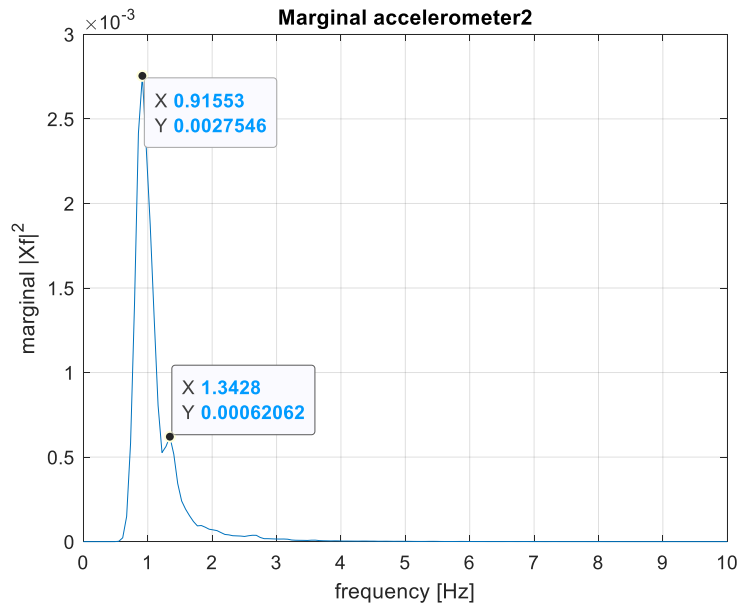


Figure 4.19 Accelerometer 2 located in the middle of the bridge during standard traffic

The graphs above show the frequency trend over approximately 4 minutes of signal recorded during standard traffic. The graphs are related to three sensors placed respectively in the middle and on the two sides of the bridge. It is possible to observe from marginal graphs how the first peak is well defined in all signals. The peak value is 0.91553 Hz. Instead the other peaks are not very energetic so it was decided to analyze the acquisitions during the passage of the truck. The graphs below show the signal of accelerometers 1 and 4.

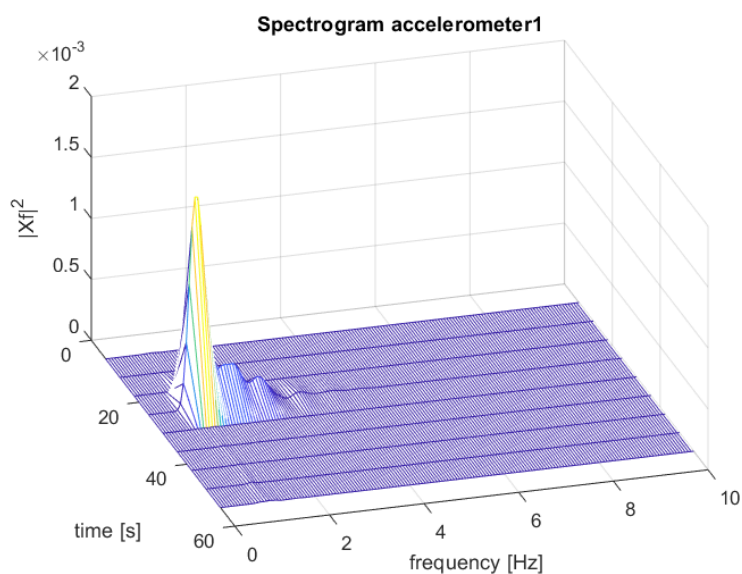


Figure 4.20 Spectrogram of accelerometer 1 located in the middle of the bridge during truck test

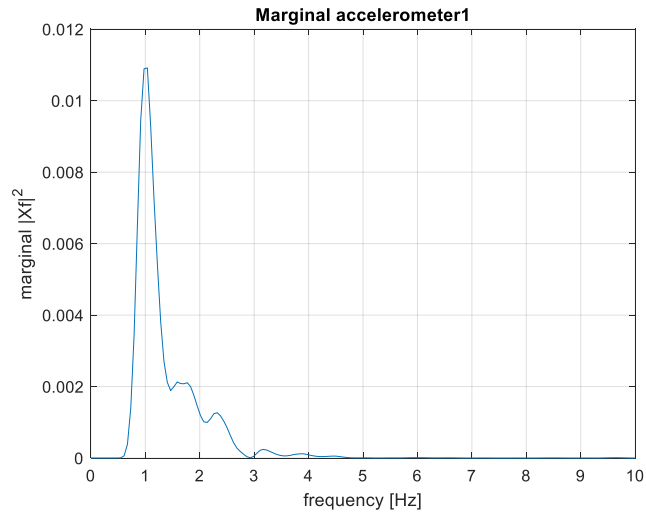


Figure 4.21 Accelerometer 1 located in the middle of the bridge during truck test

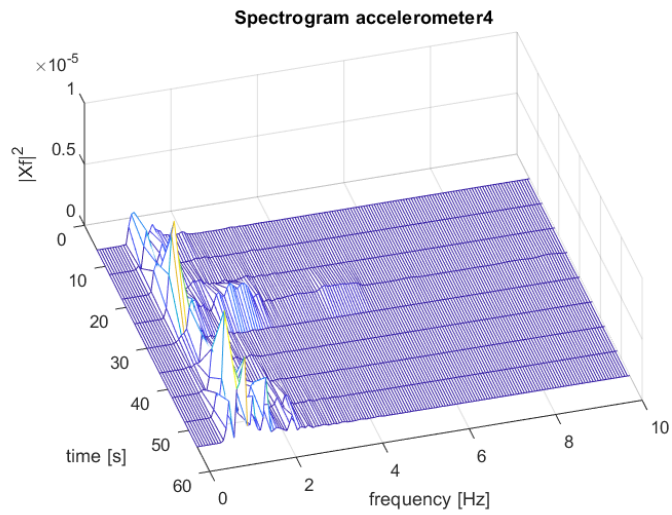


Figure 4.22 Spectrogram of accelerometer 4 located on the side opposite to the Cannara center during truck test

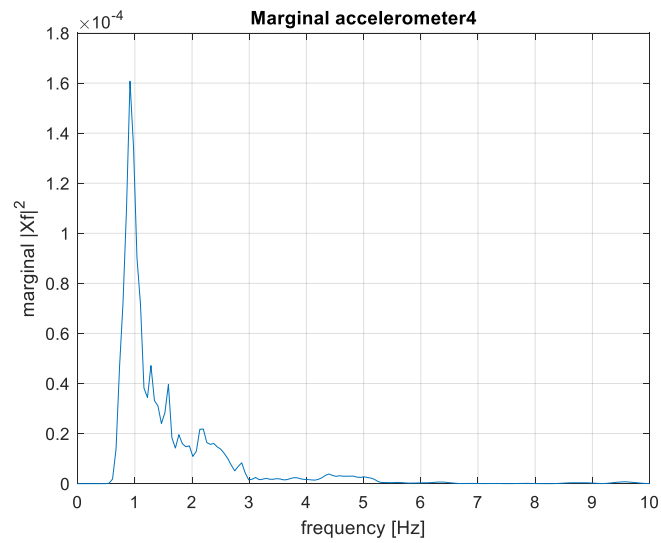


Figure 4.23 Accelerometer 4 located on the side opposite to the Cannara center during truck test

It is possible to see how the most energetic frequency continues to be almost at 1 Hz value during the acquisitions with the passage of the truck lasting about 50 seconds. In this case there are also frequencies with more energy compared to standard traffic acquisitions. The table below shows the peaks identified in marginal graphs relating to the six accelerometers.

SENSOR	PEAKS		
	ACC1	0.98	1.65
ACC2	1.04	1.71	2.44
ACC3	0.98	1.65	2.26
ACC4	0.92	1.28	1.60
ACC5	0.92	1.34	1.71
ACC6	1.04	1.40	1.65

Table 4.2 Energy peaks in the marginal graphs during truck test

The value between 0.9 Hz and 1 Hz can be considered the frequency of the first vibrating mode of the structure because it is present in all the sensors during both acquisitions. After the comparison of the two acquisitions it was interesting to evaluate the frequency peaks after the passage of the truck. The free decay part of the signal was analyzed. The table below shows the energy peaks in frequency.

SENSOR	PEAKS			
	ACC1	0.98	1.22	1.40
ACC2	0.92	1.22	1.46	1.71
ACC3	0.98	1.10	1.40	1.77
ACC4	0.92	1.28	1.59	1.77
ACC5	0.92	1.10	1.34	1.77
ACC6	0.98	1.10	1.46	1.65

Table 4.3 Energy peaks in the marginal graphs during truck test (free decay)

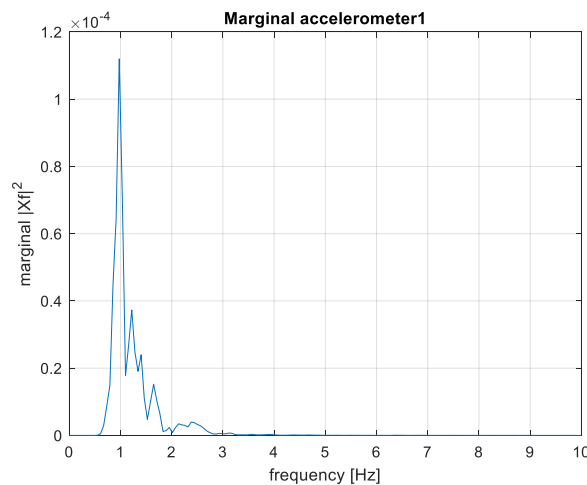


Figure 4.24 Accelerometer 1 located in the middle of the bridge during truck test (free decay)

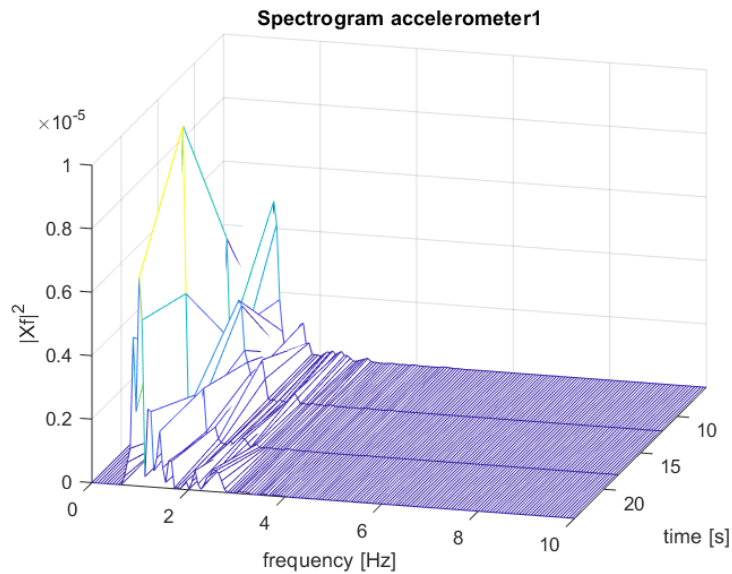


Figure 4.25 Spectrogram of accelerometer 1 located in the middle of the bridge during truck test (free decay)

Strong energy peak is present at 1 Hz also analyzing the part of the signal in free decay. Our analysis was carried out on the displacements but it can also be developed directly on the accelerations. A counter test using accelerations showed the same peaks but with a lower energy content. A peak of energy at around 1 Hz is systematically detected in time-frequency analysis. It is the first own frequency of the bridge. This value is lower compared to the frequency value of the first mode identified by fem models. The values of the first mode in the model hinged on the Cannara side with reduced stiffness and in the model fully restrained on the Cannara side with reduced stiffness are respectively 1.42 and 1.66. Therefore, the models seem to overestimate the actual frequency values of the bridge. This can be due to the constraints conditions adopted that are too rigid. For example if we use the fully restrained condition we are assuming that the bridge is longer than its total length. Therefore, from these analyzes it seems to be necessary to release completely both sides of the bridge or to introduce Winkler'elastic springs. Moreover it would be probably interesting to simulate the backfill on both sides of the bridge.

4.4 CONCLUSION

Data analysis in time-frequency domain shows a systematic peak in marginal graphs of all the six accelerometers related to the acquisitions during standard traffic. The energy peak is around 1 Hz. The same peak value is present in the analysis of the acquisitions during the passage of the truck at different speeds and in the analysis of the free decay part of this signal. Thus, we can affirm that this frequency with an high energy content is the frequency of the first vibrating mode of the bridge. The marginal graphs of truck test show also two or three other peaks but we can't consider these frequency values relative to the structure's own modes because we don't have a lot of informations about it. The frequency of the first vibrating mode identified by FEM models appears higher compared to the value of 1 Hz. Therefore, we can affirm that the FEM models overestimate the real frequencies of the structure. The models are realized in a more rigid way compared to the reality. The reason of this is due to the restrained conditions. For example when we consider a model fully restrained on the Cannara side, we simulate that the bridge is longer than its length. To reduce the frequency values of fem models is necessary to release the bridge on both sides or to introduce Winkler's elastic springs. It is also possible to reduce the frequency values moving down the stiffness but in the models with reduced stiffness its value is already low. It will be useful to carry out further tests to calibrate correctly the fem model. It is necessary to drill cores on concrete to evaluate its current characteristics and to investigate the embankment on both sides of the bridge.

The ratio between the signal value and the noise value appear not so high particularly during standard traffic. Probably the sensitivity of the sensors is too low to pick up vibrations not so high like truck vibrations. The noise almost completely masked the signal. It is possible to overcome this limit creating more sensitive sensors to increase the signal, leaving the noise value unchanged. NBG Systems company can do this. The problem with more sensitive sensors is saturation. For example more precise accelerometers could measure a smaller acceleration range but the passage of the heavy vehicle could saturate the measure. In this case we would have not a correct

value of acceleration. Therefore, the acquisitions with heavy vehicles can be carried out perfectly with the sensors used by us.

A possible intervention activity was thought to remove the causes of instability and to implement the overall consolidation of the bridge:

- It is possible to remove the causes of the yielding of the abutment introducing the deep foundations. In particular it can be introduced a series of micropiles able to move the load induced by the bridge on the abutments to a sufficiently deep and stable soil level to avoid hydrogeological interference over time;
- It is possible to realize a reinforcement of the slab to recover the full efficiency of the bridge. The intervention could involve the use of composite materials or Fiber Reinforced Polymers (FRP). They are useful for the recovery of reinforced concrete structure. They could be used to recover damaged parts of the bridge and to reinforce the parts that suffer from deformation induced by the yielding;

The choice of consolidation and reinforcement interventions have been designed to minimize interference with traffic. These proposals will be discussed after having carried out careful analysis to confirm the hypotheses on the causes of the yielding of one abutment of the Cannara Bridge.

All the twelve sensors installed on the bridge will remain there for one year. Professor Ubertini wants to carry out a complete dynamic identification of the bridge (modal forms, frequencies and damping) recording one hour of signal. The goal is to develop an analysis considering the passage of heavy vehicles only. It will be necessary to link the transit of heavy vehicles recorded during the acquisitions. It will be necessary to consider a period equal to 1000 seconds multiplied by the own period of the structure to have a good dynamic identification.

Furthermore, it was decided with professor Ubertini and the NBG company to carry out a comparison between fiber optic sensors and MEMS accelerometers installing them on the same structure. It will be interesting to compare the results of the two different sensors to understand more informations.

REFERENCES

Aktan A. E., Helmicki A. J. and Hunt V. J. *Issues in Health Monitoring for Intelligent Infrastructure*. Journal of Smart Materials and Structures 7, 674-692. – 1998

Balageas D. (n.d.), *Introduction to Structural Health Monitoring*. *Structural Health Monitoring*, 13–43. DOI: 10.1002/9780470612071.ch1 – 2006

Basciani C., Neri P., Relazione tecnica su prove di carico statico effettuate sul ponte di Cannara. - Febbraio 2018

Chang P. C., Flatau A., Liu S. C., *Review Paper: Health Monitoring of Civil Infrastructure*. *Structural Health Monitoring: An International Journal*, 2(3), 257–267. DOI: 10.1177/1475921703036169 - 2003

Chapuis B., *Introduction to Structural Health Monitoring*. *IIV Collection*, 1–11. DOI: 10.1007/978-3-319-69233-3_1 – 2017

Chen H.-P., Ni Y.-Q., *Structural Health Monitoring of Large Civil Engineering Structures*. DOI: 10.1002/9781119166641 – 2018

Chen W., Zhu Y., Fu Y., Feng J., Huang S., *Process Control and Inspection for Industry*. DOI: 10.1117/12.403852 – 2000

Doebling S. W., Farrar C. R., Prime M. B., *A Summary Review of Vibration-Based Damage Identification Methods*. *The Shock and Vibration Digest*, 30(2), 91–105. DOI: 10.1177/058310249803000201 - 1998

Fuhr P. L., Huston D. R., *Pacific Northwest Fiber Optic Sensor Workshop*. DOI: 10.1117/12.207756 – 1995

Giurgiutiu V., *Structural Health Monitoring of aerospace composites* [Book]. – 2016

Hua-Peng C., and Yi-Qing N., *Structural Health Monitoring of Large Civil Engineering Structures* [Book] - 2018.

Huston D. R., Fuhr P. L., Udd, E., Inaudi D., *Fiber Optic Sensor Technology and Applications*. DOI: 10.1117/12.372945 – 1999

Karbhari V. M., *Design Principles for Civil Structures. Encyclopedia of Structural Health Monitoring*. DOI: 10.1002/9780470061626.shm107 – 2009

Latella L., Relazione tecnica sulle indagini geognostiche, geofisiche e prove di laboratorio effettuate sul ponte di Cannara – Febbraio 2018

Lynch J. P., *A Summary Review of Wireless Sensors and Sensor Networks for Structural Health Monitoring. The Shock and Vibration Digest, 38(2), 91–128*. DOI: 10.1177/0583102406061499 – 2006

Margiotta P., *I ponti ad arco in calcestruzzo sostenuti da cavi nelle fasi di costruzioni ed esercizio*. Palermo: Università degli Studi di Palermo - 2011.

Materazzi A. L., Balli R., Relazione tecnica di valutazione delle origini del fenomeno fessurativo sul ponte di Cannara - 1997

Meng X., Nguyen D., Xie, Y., Owen J., Psimoulis P., Ince S., ... Bhatia P., *Design and Implementation of a New System for Large Bridge Monitoring—GeoSHM. Sensors, 18(3), 775*. DOI:10.3390/s18030775 - 2018

Peters K. J., Inaudi D., *Fiber optic sensors for assessing and monitoring civil infrastructures. Sensor Technologies for Civil Infrastructures, 121–158*. DOI: 10.1533/9780857099136.121 – 2014

Santarella L., Miozzi E., *Ponti italiani in cemento armato (seconda raccolta)*. Milano: Ulrico Hoepli, - 1932

Soga K., Luo L., *Distributed fiber optics sensors for civil engineering infrastructure sensing. Journal of Structural Integrity and Maintenance, 3(1), 1–21*. DOI: 10.1080/24705314.2018.1426138 - 2018

Sohn H., Farrar C. R., Hemez F., Czarnecki J., *A review of Structural Health Monitoring Literature 1996-2001.* - 2003

Song G., Wang C., Wang B., *Structural Health Monitoring (SHM) of Civil Structures.* *Applied Sciences*, 7(8), 789. DOI: 10.3390/app7080789 – 2017

Tennyson R. C., Mufti A. A., Neale K., *Health Monitoring and Management of Civil Infrastructure Systems.* DOI: 10.1117/12.435594 – 2001

Udd E., *Fiber Optic Sensors for Structural Monitoring.* *Frontiers in Optics 2014.* DOI: 10.1364/fio.2014.ftu4b.1 – 2014

SITOGRAFHY

https://moodle2.units.it/pluginfile.php/215992/mod_resource/content/0/02-NS-RichiamaAnalisiSegnali.pdf

http://www.maths.lu.se/fileadmin/maths/personal_staff/mariasandsten/TFkompe_r2.pdf

http://www.diegm.uniud.it/bernardini/Didattica/Analisi/Lucidi/analisi-tf-slide_2.pdf

https://biomedia4n6.uniroma3.it/teaching/tds_el/materiale_didattico/TeoriaDeiSegnali.pdf

<http://biblus.acca.it/download/norme-tecniche-per-le-costruzioni-2018-ntc-2018-pdf/>

<https://www.hbm.com/it/4596/cose-la-fibra-a-griglia-di-bragg/>